

ANALYSIS, SIMULATION, AND EVALUATION OF MAXIMUM POWER
POINT TRACKING (MPPT) METHODS FOR A SOLAR POWERED
VEHICLE

by
HANNES KNOPF

A thesis submitted in partial fulfillment of the
requirements for the degree of

MASTER OF SCIENCE
in
ELECTRICAL AND COMPUTER ENGINEERING

Portland State University
1999

Dedicated to

my great grandmother

Marliese Knopf

Table of Contents

List of Tables	v
List of Figures	vi
1 Introduction	1
2 The Photovoltaic Power System	6
2.1 Photovoltaic Cells and Solar Arrays	7
2.1.1 Physical Structure of a Photovoltaic Cell	7
2.1.2 Equivalent Circuit and Mathematical Model	10
2.1.3 The Solar Panel	12
2.2 Lead-Acid Batteries	19
2.3 DC-DC Converters	23
2.3.1 The Buck Converter	24
2.3.2 The Boost Converter	37
2.3.3 The Buck-Boost Converter	48
3 Maximum Power Point Tracking	58
3.1 Simple panel-load matching	59
3.2 Semi-dynamic load matching	61
3.3 The voltage-feedback method	62
3.3.1 Measurement of V_{oc} at the panel	64

3.3.2	Usage of a pilot cell	65
3.4	The power-feedback method	66
3.4.1	The perturbation and observation method (P&O)	66
3.4.2	The incremental conductance method (IncCond)	72
3.4.3	Analog MPPT methods	76
3.4.4	Forced oscillation — auto oscillation	79
3.5	The current-feedback method	82
4	Simulation and Evaluation	84
4.1	Modeling of the system components	86
4.1.1	The solar panel	86
4.1.2	The batteries	89
4.1.3	The dc-to-dc converter	89
4.1.4	The MPPT Controller	93
4.2	The MPPT simulations	94
4.2.1	Operation under stable environmental conditions	95
4.2.2	Performance under changing insolation levels	114
4.2.3	Performance under changing temperature levels	123
4.2.4	Performance under simulated random variations of temper- ature and insolation	129
5	Conclusions	140
	Bibliography	144
	Appendix A	150
A.1	Component specifications for Simulink simulations	150

A.2 Block diagrams of the simulated models 153

Appendix B **157**

B.1 Signal curves of various system configurations under standard test
conditions (STC) 157

B.2 Signal curves under varying operating conditions 163

List of Tables

3.1	The solar panels and the corresponding measured values for I_{sc} and V_{oc} at different temperatures for the solar car SOLTRAIN.	61
3.2	Truth table for the improved P&O algorithm after Burger	71
4.1	Comparison of the ripple losses for the different MPPT techniques under steady-state conditions (STC).	112

List of Figures

1.1	The solar powered racing car SOLTRAIN.	5
1.2	SOLTRAIN license plate.	5
2.1	Power train of a solar powered vehicle.	6
2.2	Schematic representation of a standard pn-junction solar cell.	7
2.3	Simple equivalent circuit diagram for a photovoltaic cell.	8
2.4	I - V characteristic of a photovoltaic cell.	9
2.5	Equivalent two-diode circuit model of a photovoltaic cell and its circuit symbol.	10
2.6	I - V characteristics of a photovoltaic cell array for various values of irradiance S at a temperature of 25°C	13
2.7	I - V characteristics of a photovoltaic cell array for various values of temperature T at an irradiance of 1000 W/m^2	13
2.8	P - V characteristics of a photovoltaic cell array for various values of irradiance S at a temperature of 25°C	14
2.9	P - V characteristics of a photovoltaic cell array for various values of temperature T at an irradiance of 1000 W/m^2	15
2.10	Maximum Power Point MPP and the corresponding voltage V_{mp} and current I_{mp} for a photovoltaic cell array with 168 cells in series operating at STC.	16
2.11	Angle of Incidence (AOI) θ and geometric face of a solar array.	17

2.12 Schematic representation of a solar panel as used in the solar car SOLTRAIN.	18
2.13 Equivalent circuit model of a lead-acid battery.	20
2.14 Ideal switch voltage $v_s(t)$, duty ratio D , and switching period T_s	24
2.15 Ideal buck converter circuit.	24
2.16 Equivalent circuit of a buck converter at closed switch time DT_s	25
2.17 Equivalent circuit of a buck converter at open switch time $D'T_s$	26
2.18 Waveform of the inductor voltage $v_l(t)$ for an ideal buck converter.	29
2.19 Conversion ratio $M(D)$ vs. duty ratio D for an ideal buck converter.	31
2.20 Buck converter with series resistor R_l to account for inductor losses.	33
2.21 Ideal boost converter circuit.	38
2.22 Equivalent circuit of a boost converter at closed switch time DT_s	38
2.23 Equivalent circuit of a boost converter at open switch time $D'T_s$	39
2.24 Conversion ratio $M(D)$ vs. duty ratio D for an ideal boost converter.	41
2.25 Boost converter with series resistor R_l to account for inductor losses.	43
2.26 Conversion ratio V_o/v_i vs. duty ratio D for a non-ideal boost con- verter dependent on R_l/Z	45
2.27 Efficiency η vs. conversion ratio V_o/v_i for a non-ideal boost converter dependent on R_l/Z	46
2.28 Ideal buck-boost converter circuit.	48
2.29 Equivalent circuit of a buck-boost converter at closed switch time DT_s	49
2.30 Equivalent circuit of a buck-boost converter at open switch time $D'T_s$	50
2.31 Conversion ratio $M(D)$ vs. duty ratio D for an ideal buck-boost converter.	52

2.32	Buck-boost converter with series resistor R_l to account for inductor losses.	53
2.33	Conversion ratio V_o/v_i vs. duty ratio D for a non-ideal buck-boost converter dependent on R_l/z	55
2.34	Efficiency η vs. conversion ratio V_o/v_i for a non-ideal buck-boost converter dependent on R_l/z	56
3.1	Top view of the SOLTRAIN's solar panel configuration. The corresponding panel names can be found in Table 3.1.	60
3.2	Voltage-feedback with pulse width modulation (PWM) on a dc-dc converter.	63
3.3	Flow chart of the P&O MPPT algorithm.	68
3.4	Deviation from the MPP with the P&O algorithm under rapidly changing insolation levels S	69
3.5	Flow chart of the IncCond MPPT algorithm.	74
3.6	Analog MPPT mechanism	77
3.7	P - V curve for the solar array with the power ripple caused by the array voltage modulation.	80
4.1	Block diagram of the MPPT-controlled solar power system.	85
4.2	SIMULINK [®] implementation of the expression $I_{R_p} = \frac{V+IzR_s}{zR_p}$	87
4.3	Functional block diagram of the solar panel.	88
4.4	Battery impedance represented as a single SIMULINK [®] transfer-function block.	90
4.5	SIMULINK [®] implementation of equation (4.4).	91
4.6	Block diagram for the simulation of a buck converter.	92
4.7	The MPPT controller generates the PWM control variable d directly.	94

4.8	Simulation of the P&O MPPT method in combination with a buck converter under stable environmental conditions.	96
4.9	Detailed plot of the waveforms of the P&O MPPT simulation with a buck converter.	98
4.10	Oscillations of P&O MPPT with a buck converter at a high frequency sampling rate (1000 Hz).	100
4.11	Power signal and control variable of P&O MPPT with boost converter at 100 Hz.	101
4.12	Signals for power P , voltage V and current I at a solar panel in a system with P&O MPPT on a boost converter at 1000 Hz.	102
4.13	Details of the discrete power signal and the control variable d of the system with P&O MPPT on a boost converter at 1000 Hz.	103
4.14	Power and control signal of a buck-boost converter with P&O MPPT operating at 50 Hz	104
4.15	Discrete power signal and control variable d of the P&O algorithm at a sampling frequency of 200 Hz in combination with a buck-boost converter.	105
4.16	Plot of the steady-state oscillations of the improved P&O MPPT mechanism with a buck converter at a sampling frequency of 100 Hz.	107
4.17	Output power ripple with an improved P&O algorithm at a buck converter operating at 1000 Hz.	108
4.18	Power and control signal of a simulation of a IncCond MPPT algorithm in combination with a buck converter at a sampling frequency of 100 Hz.	110

4.19	Power and control signal of a simulation of the IncCond MPPT algorithm in combination with a buck converter at an increased sampling frequency of 1 kHz.	111
4.20	Power output signals of the various MPPT configurations under a slow increase in insolation	115
4.21	Comparison of the various MPPT's signals for output power, panel voltage, and the control variable d under rapidly increasing insolation levels.	117
4.22	Power and control signal of the various MPPTs under quickly decreasing insolation levels.	119
4.23	Signals of the four simulated MPPTs employing a boost converter during rapidly increasing insolation.	122
4.24	Output power, panel voltage, and the duty-ratio d for the various MPPT algorithms under slowly increasing cell temperature.	125
4.25	Signals for output power and panel voltage of the various digital MPPT methods under slowly decreasing cell temperature.	126
4.26	Signals of output power, panel voltage, and the duty ratio d of the various MPPT algorithms under quickly decreasing cell temperature.	128
4.27	Signal curves of a solar power supply system controlled by a conventional P&O MPPT under randomly varying environmental conditions.	131
4.28	Signal curves of a solar power supply system controlled by the improved P&O MPPT under randomly varying environmental conditions.	133
4.29	Signal curves of a solar power supply system controlled by the IncCond MPPT under randomly varying environmental conditions.	135

4.30	Signal curves of a solar power supply system controlled by the improved IncCond MPPT algorithm under randomly varying environmental conditions.	137
4.31	Comparison of the power signals of the various MPPT methods under randomly varying temperature and insolation levels.	138
A.1	Block diagram of the buck converter.	153
A.2	Block diagram of the boost converter.	153
A.3	Block diagram of the buck-boost converter.	154
A.4	Block diagram of the P&O MPPT algorithm.	154
A.5	Block diagram of the improved P&O algorithm.	155
A.6	Block diagram of the IncCond algorithm.	156
B.1	Power and control signal for the improved P&O method operating with a boost converter at a sampling frequency of 100 Hz.	157
B.2	Power and control signal for the improved P&O method operating with a boost converter at an increased sampling frequency of 1 kHz.	158
B.3	Power and control signal for the improved P&O method operating with a buck-boost converter at a sampling frequency of 50 Hz.	159
B.4	Power and control signal for the improved P&O method operating with a buck-boost converter at an increased sampling frequency of 200 kHz.	160
B.5	Power and control signal for the IncCond MPPT operating with a boost converter at a sampling frequency of 100 Hz.	161
B.6	Power and control signal for the IncCond MPPT operating with a boost converter at an increased sampling frequency of 1 kHz.	161

B.7	Power and control signal for the IncCond MPPT operating with a buck-boost converter at a sampling frequency of 50 Hz.	162
B.8	Power and control signal for the IncCond MPPT operating with a buck-boost converter at an increased sampling frequency of 200 Hz.	162
B.9	Output power and control variable d of the various simulated MPPT techniques under slowly falling insolation levels.	163
B.10	Signal curves of a solar power supply system employing a boost converter controlled by the P&O MPPT algorithm under randomly varying environmental conditions.	164

Chapter 1

Introduction

“We believe that the clean and inexhaustible power of sunlight will be the most promising resource in mankind’s quest to develop sustainable energy in the 21st century and beyond.”

*— Hirofumi Tezuka, director and general manager
Kyocera Corporation, Solar Division*

The generation of energy in our modern industrialized society is still mainly based on a very limited resource: petroleum. As the world’s energy demands rise and new sources for petroleum become scarce, the search for alternative energy resources has become an important issue for our time. A large amount of research has been done not only in the area of nuclear power generation but also in the area of unlimited energy sources such as wind power generation and solar energy transformation. Significant projects have been realized and others are still in planning. Most of these new systems are used to generate electrical power which is fed into the public electrical grid to provide energy for businesses and private homes.

In addition to homes and businesses, another important element of our industrialized society generates a considerable demand for petroleum based energy: personal transportation. Since the combustion of carbon based petroleum derivatives generates the infamous greenhouse gas carbon-dioxide (CO₂), the continually

increasing traffic significantly contributes to global warming and is the main source of air pollution in big cities.

This has led to programs and efforts to design low emission (LEV) and zero emission (ZEV) vehicles. Research is being done in highly efficient combustion engines, fuel cell technology, hybrid cars combining conventional propulsion techniques with electrical drive systems, and electrical vehicles powered either by batteries or by a solar energy conversion system.

This search for alternative energy sources to power individual vehicles led to the decision of a group of Reed College students in the early 90's to build the solar-powered racing car SOLTRAIN.

A solar vehicle is powered by photovoltaic cell arrays which allow for direct conversion of solar radiation into electrical energy. Since space and weight are very limited with any vehicle but particularly with a racing vehicle, it is desired that the maximum possible amount of energy be obtained from the employed photovoltaic cells.

Every photovoltaic cell array has an optimum operating point, called the maximum power point (MPP), which varies depending on cell temperature and the present insolation level. The goal of this thesis is to find the mechanism best suited for employment in a moving vehicle to optimally track this point of maximum efficiency and adjust the operating point of the solar cell array accordingly.

The solar-powered racing vehicle SOLTRAIN is not yet equipped with such a maximum power point tracking (MPPT) device. The addition of such an operating point controller will yield an estimated 60 % increase in power output from the solar cells. This leads to a higher efficiency of the overall system without adding any additional photovoltaic cell surface to the existing array.

There are two main groups of MPPTs: those that use analog circuitry and classical feedback control, and others that use a microprocessor to maintain control of the operating point.

Analog systems have the advantage of having low cost components, but are more problematic to control. It is difficult to develop a stable system which is able to maintain its accuracy even under extreme operating conditions such as the wide temperature variations that occur in an outdoor vehicle.

The digitally controlled MPPT systems have the advantage that a power point tracking algorithm will not be influenced by changes in temperature and therefore will always be very reliable. Additionally, the use of an algorithm allows for additional control modes to cope with certain system states such as a fully charged battery buffer. The digital controller also allows for operational data logging to monitor system behavior and performance which will be of high analytical value for an experimental vehicle such as the SOLTRAIN.

The main challenge in designing a microprocessor-controlled MPPT is the combination of the strongly nonlinear continuous-time system of the photovoltaic cell array with a discrete-time control device. This union makes it impossible to evaluate such important factors as system performance and stability with the classical approach of closed-form transfer-function analysis.

This thesis will introduce a novel approach to analyze, simulate, and evaluate the complete solar power supply system with a digital MPPT controller under varying operating conditions as they are experienced in a moving outdoor vehicle. The simulation tool SIMULINK[®], which is included in The MathWorks's software package MATLAB[®], enables for the simulation of mixed discrete-continuous systems and therefore allows the direct comparison of the various approaches to maximum

power point tracking under the same operating conditions. The digitally controlled MPPT can be directly included in the simulated system, and modifications to improve the MPPT performance of conventional MPPT algorithms can be evaluated without having to build and modify an expensive prototype.

To be able to properly simulate the complete solar power supply system, detailed mathematical models for all of the system's components are necessary. These components consist of the array of photovoltaic cells, an energy buffer in the form of a parallel-connected battery pack, and optionally a dc-to-dc converter. Figure 2.1 shows a representative system schematic of this configuration. The introduction of the components and the detailed derivation of their mathematical models can be found in Chapter 2.

Chapter 3 discusses a wide variety of available MPPT techniques and possible modifications and improvements. Both, analog and microprocessor based methods are introduced and analyzed.

In Chapter 4 various MPPT methods are applied to the photovoltaic power supply systems introduced in Chapter 2. Their performance under a large variety of operating conditions is analyzed and evaluated supported by SIMULINK® simulations.

The solar car SOLTRAIN and its State of Oregon licence plate are shown in Figures 1.1 and 1.2.



Figure 1.1: The solar powered racing car SOLTRAIN.



Figure 1.2: SOLTRAIN license plate.

Chapter 2

The Photovoltaic Power System

The power supply system for a solar vehicle consists of an array of photovoltaic cells, a set of batteries as an energy buffer and optionally some kind of converter to match the voltage of the solar array with the battery voltage (Figure 2.1). If the conversion ratio of the converter is varied by a controller to constantly adjust the operating voltage of the solar panel to its point of maximum power (V_{mp}), it is being operated as a Maximum Power Point Tracker (MPPT).

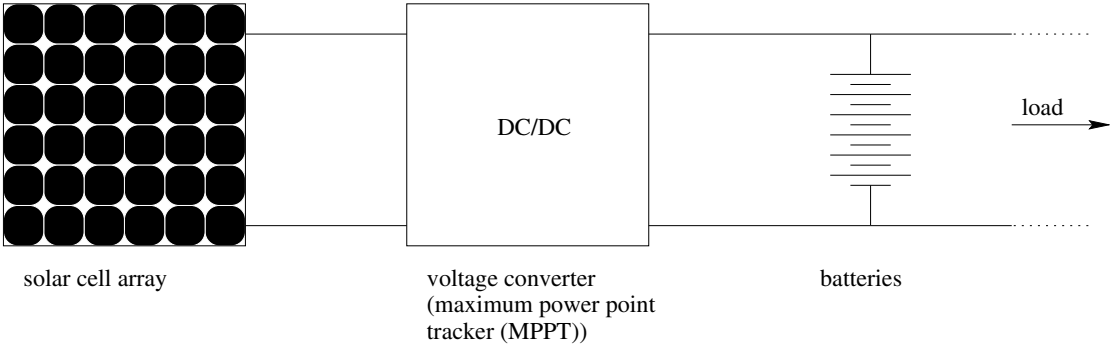


Figure 2.1: Power train of a solar powered vehicle.

This chapter will introduce the various elements of such a photovoltaic power system and derive the mathematical models necessary to represent its behavior in a complete system simulation.

2.1 Photovoltaic Cells and Solar Arrays

2.1.1 Physical Structure of a Photovoltaic Cell

A solar cell is a semiconducting device that absorbs light and converts it into electrical energy. Today's most common cell is a mass manufactured single p-n junction Silicon (Si) cell with an efficiency up to about 17 % [Möl93]. It consists of a moderately p-doped base substrate and a thin heavily n-doped top layer. Thin metal contacts on the surface and a plain metal layer on the back connect this photovoltaic element to the load (Figure 2.2).

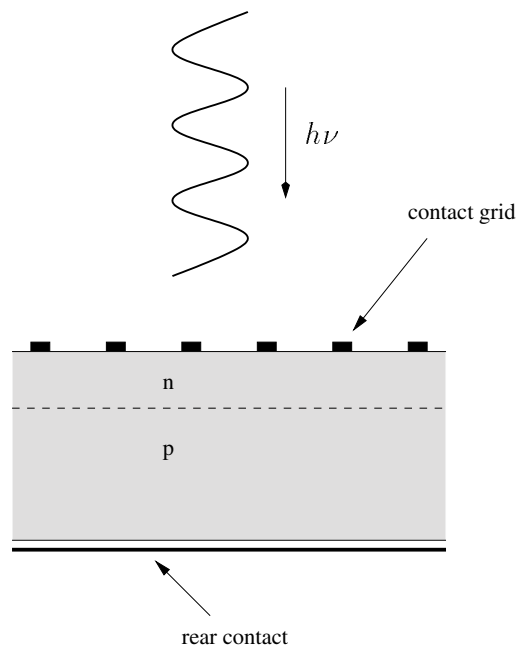


Figure 2.2: Schematic representation of a standard pn-junction solar cell.

If exposed to radiation, electron-hole pairs are created by photons with an energy greater than the band-gap energy of the semiconductor ($h\nu > E_g$). This is called the photovoltaic effect. The newly created charge carriers in the depletion

region are separated by the existing electric field. This leads to a forward bias of the p-n junction and builds up a voltage potential called the photo-voltage. As soon as a load is connected to the cell, this voltage will cause a current (called the photo-current) to flow through the load. In addition the forward bias of the p-n junction also leads to a small diode current I_d in the opposing direction of the photo-current [Nev78, Cle96].

The p-n junction properties and the discussed reaction of the semiconductor to radiation lead to the simplified and idealized equivalent circuit diagram of a photovoltaic cell as shown in Figure 2.3.

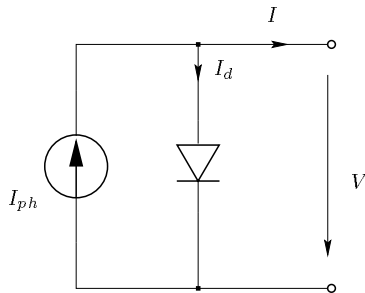


Figure 2.3: Simple equivalent circuit diagram for a photovoltaic cell.

Application of Kirchoff's law and the exponential diode equation (2.1) leads to a simple mathematical model for a photovoltaic cell (2.2) [Möl93].

$$I_d = I_s \left[e^{\frac{qV}{2kT}} - 1 \right], \quad (2.1)$$

$$I = I_{ph} - I_s \left[e^{\frac{qV}{2kT}} - 1 \right]. \quad (2.2)$$

I and V are the output current and voltage of the cell. I_{ph} is the generated photo-current and I_s is the reverse saturation current of the diode. Furthermore, the

characteristics are influenced by the temperature T and by the constant for the elementary charge q ($1.602 \cdot 10^{-19}$ C) and Boltzmann's constant k ($1.380 \cdot 10^{-23}$ J/K).

With this model in mind it is not surprising that the I - V characteristics of a photovoltaic cell are quite similar to those of a regular diode. The major difference is the existence of an open circuit voltage V_{oc} which leads to a short circuit current I_{sc} visible as a current offset in the characteristic curve (Figure 2.4). A photovoltaic cell in total darkness will perform similar to a regular diode [Möl93, FB83].

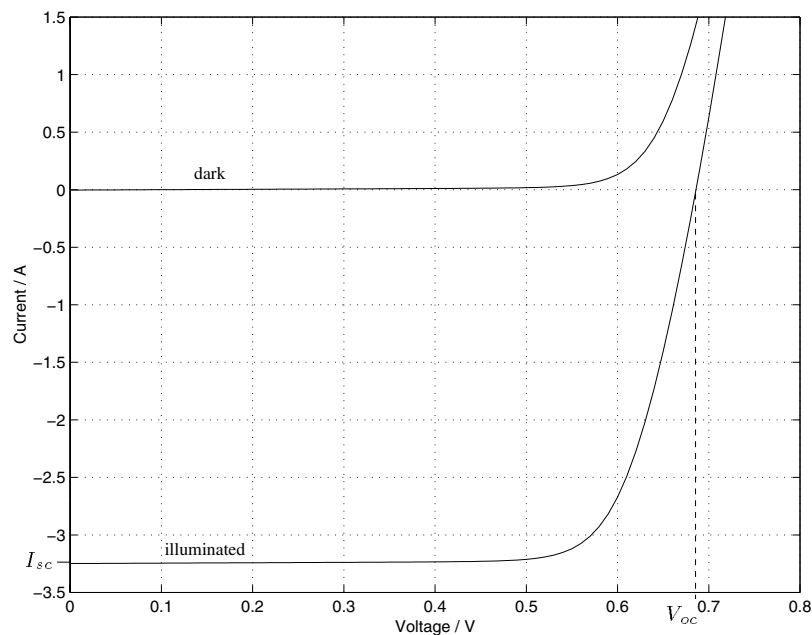


Figure 2.4: I - V characteristic of a photovoltaic cell.

Many efforts are being made to increase the efficiency of solar cells by utilizing multi-layer techniques and various semiconducting materials such as Gallium Arsenide (GaAs), Indium Phosphide (InP), Copper Indium Selenide (CuInSe₂), Cadmium Telluride (CdTe), Copper Selenide (Cu₂Se), and Zinc Phosphide (Zn₃P₂) [Fey97]. This increased the cell efficiency to more than 21 % for Si and 25 % for

GaAs solar cells in recent years [BGK⁺97].

Since a higher complexity of a cell is accompanied by a higher price, research has also been done in the area of low cost mass production which led for example to amorphous polycrystalline thin film solar cells [FB83]. The thin film configuration greatly reduces material costs and allows for continuous flow processing. The disadvantage of this technique is a reduction in cell efficiency to approximately 10 %-13 %.

2.1.2 Equivalent Circuit and Mathematical Model

Actual measurements on real cells under diverse operating conditions, however, show the need for a more sophisticated model. In particular the internal resistance of the device has to be taken into consideration. This leads to the widely used “two-diode model” as shown in Figure 2.5 [Möl93, Bur97].

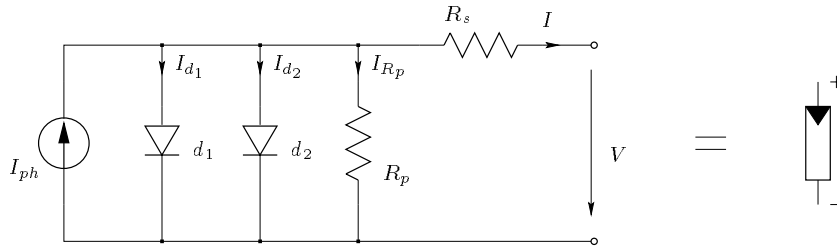


Figure 2.5: Equivalent two-diode circuit model of a photovoltaic cell and its circuit symbol.

Figure 2.5 is a representation of the mathematical model for the current-voltage characteristic which is given as [GRIR97]:

$$I = I_{ph} - I_{s1} \left[e^{\frac{q(V+IR_s)}{n_1 kT}} - 1 \right] - I_{s2} \left[e^{\frac{q(V+IR_s)}{n_2 kT}} - 1 \right] - \frac{V + IR_s}{R_p}. \quad (2.3)$$

I and V are the output current and output voltage of the photovoltaic cell, I_{ph} is the generated photo-current, I_{s_1} and I_{s_2} are the diodes' reverse saturation currents, n_1 and n_2 the diode ideality factors, R_s and R_p the series and parallel resistance (respectively), and T is the absolute temperature in Kelvin. The equation also contains the elementary charge constant q ($1.602 \cdot 10^{-19}$ C) and the Boltzmann constant k ($1.380 \cdot 10^{-23}$ J/K). The photo-current I_{ph} is equal to its value at maximum insolation¹ times the irradiance S in percent ($I_{ph} = SI_{ph,max}$).

It is obvious from equation (2.3), that the current-voltage characteristic strongly depends on insolation and temperature. The dependency on the temperature is further amplified by the properties for the photo-current I_{ph} and the diodes' reverse saturation currents I_s which are given by Burger [Bur97]:

$$I_{ph}(T) = I_{ph}|_{(T=298\text{K})} [1 + (T - 298\text{K}) \cdot (5 \cdot 10^{-4})], \quad (2.4)$$

$$I_{s_1} = K_1 T^3 e^{-\frac{E_g}{kT}}, \quad (2.5)$$

$$I_{s_2} = K_2 T^{\frac{5}{2}} e^{-\frac{E_g}{kT}}, \quad (2.6)$$

where E_g is the band-gap energy of the semiconductor and

$$K_1 = 1.2 \text{ A/cm}^2\text{K}^3, \quad (2.7)$$

$$K_2 = 2.9 \cdot 10^5 \text{ A/cm}^2\text{K}^{5/2} \quad (2.8)$$

vary with the manufacturer and depend on the size of the cell surface area.

¹Derived from the definition of the standard test conditions (STC) for solar arrays, a maximum insolation of 1000 W/m^2 is assumed. STC are reference testing values of cell temperature (25°C), in-plane irradiance (1000 W/m^2) and air mass solar reference spectrum (AM = 1.5) for photovoltaic (PV) module or PV cell testing, defined in IEC 61829 (1995-03) [IEC95].

2.1.3 The Solar Panel

In photovoltaic energy systems, single cells are combined into solar cell arrays by connecting a number of cells in series. Consideration of the equivalent circuit model (Figure 2.5 on page 10) leads to the equation for a photovoltaic cell array (commonly called a solar panel or solar array) with z photovoltaic cells in series connection (2.9) [Bur97].

$$I = I_{ph} - I_{s1} \left[e^{\frac{q(V+IzR_s)}{zn_1kT}} - 1 \right] - I_{s2} \left[e^{\frac{q(V+IzR_s)}{zn_2kT}} - 1 \right] - \frac{V + IzR_s}{zR_p}. \quad (2.9)$$

These panels then can be further arranged in series or parallel connections to achieve the desired voltage and current values for the system.

As mentioned earlier in section 2.1.2, the I - V characteristics of a photovoltaic cell strongly depend on insolation and temperature (equations (2.3) to (2.6)). This becomes very apparent when evaluating equation (2.3) for selected values of temperature and irradiance and plotting the results as an I - V graph (Figures 2.6 and 2.7). Figure 2.6 shows that the output current I of an array is greatly influenced by the change in insolation S , whereas the output voltage V stays approximately constant. In contrast, for a changing temperature one can see that the voltage varies widely while the current remains unchanged (Figure 2.7).

The P - V characteristics for a photovoltaic cell array can be obtained from the I - V characteristics and the relation for the output power $P = VI$ as shown in Figures 2.8 and 2.9. These figures clearly show how the dependency of output current I and output voltage V on temperature and insolation translate into a dependency of the output power on the same two parameters.

Figure 2.8 confirms the expected behavior of a device that converts solar energy into electrical energy: the power output of a solar panel is greatly reduced for a

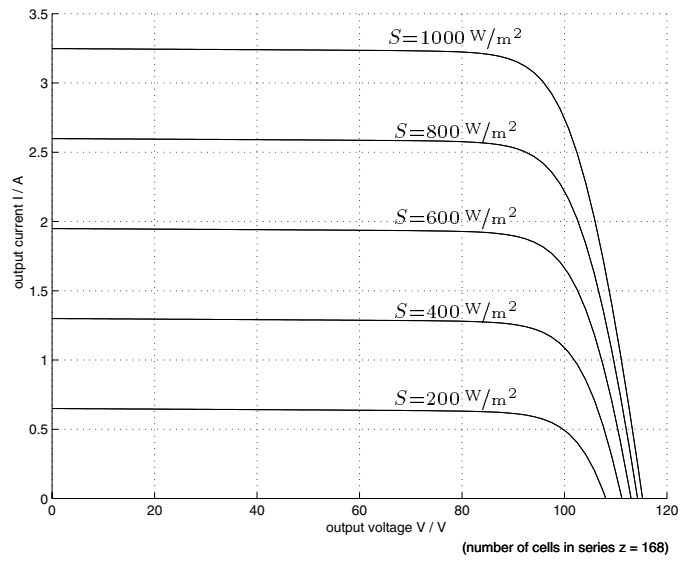


Figure 2.6: I - V characteristics of a photovoltaic cell array for various values of irradiance S at a temperature of 25 °C.

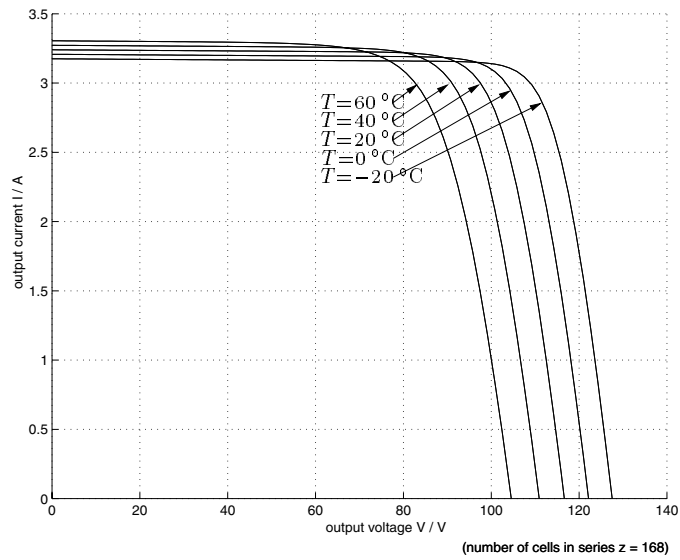


Figure 2.7: I - V characteristics of a photovoltaic cell array for various values of temperature T at an irradiance of 1000 W/m^2 .

decreasing insolation. It also shows an effect which might not be immediately obvious: the output power is reduced by an increase in panel temperature. This can be explained by the significant temperature dependency of the open circuit voltage V_{OC} . The voltage drops due to an increase of the reverse saturation current I_s in the diode (see equations (2.5) and (2.6)). The principal temperature variation of I_s is a result of the temperature variation of the intrinsic carrier concentration, which yields a higher recombination rate inside the semiconductor [Nev78].

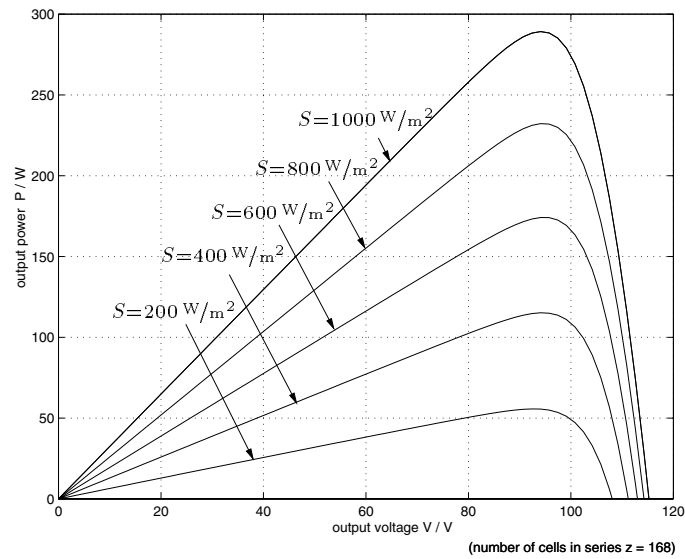


Figure 2.8: P - V characteristics of a photovoltaic cell array for various values of irradiance S at a temperature of 25°C .

It can also be seen that the output power of a solar panel not only depends on temperature and insolation, but also very strongly on its operating voltage V . The point of maximum power indicated as MPP (Maximum Power Point) in Figure 2.10 is the desired operating point for a photovoltaic array to obtain maximum efficiency. The corresponding values for voltage and current are called V_{mp} and I_{mp} , respectively.

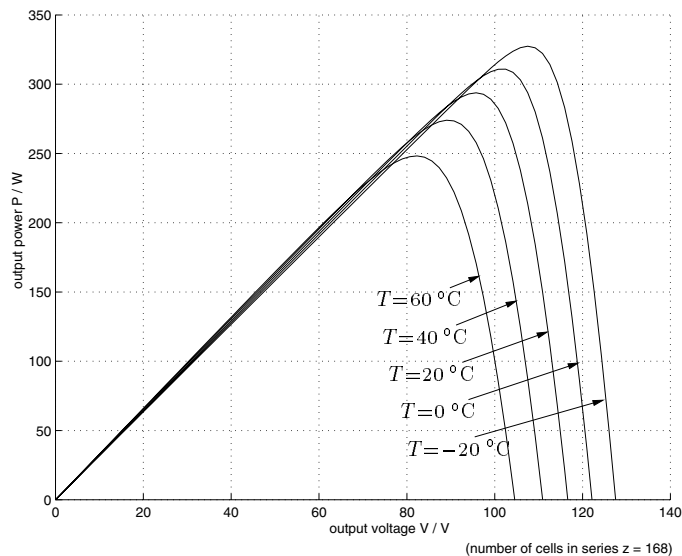


Figure 2.9: P - V characteristics of a photovoltaic cell array for various values of temperature T at an irradiance of 1000 W/m^2 .

The P - V curve shown in Figure 2.10 shares the temperature and insolation dependencies shown in Figures 2.6–2.9; as a result the value for the optimum operating voltage V_{mp} will vary constantly with changes in these environmental conditions. In these circumstances a maximum power point tracking (MPPT) mechanism can help to significantly increase the power output of a solar power system by adjusting the system load in such a way that the operating voltage V will always be approximately equal to the optimum operating voltage V_{mp} :

$$V = V_{mp} + \epsilon; \quad (2.10)$$

with ϵ being as small as possible.

The importance of keeping the operating voltage as close as possible to V_{mp} is illustrated in Figure 2.10. If the operating voltage differs from V_{mp} by about 10% as indicated by V_1 , it will result in a output power reduction of almost 25%. Comparison of systems with and without maximum power point tracking devices

shows that units with a MPPT output 80-90 % of their theoretical maximum power, whereas units without a MPPT only operate at 30 % of their maximum power output [HS98].

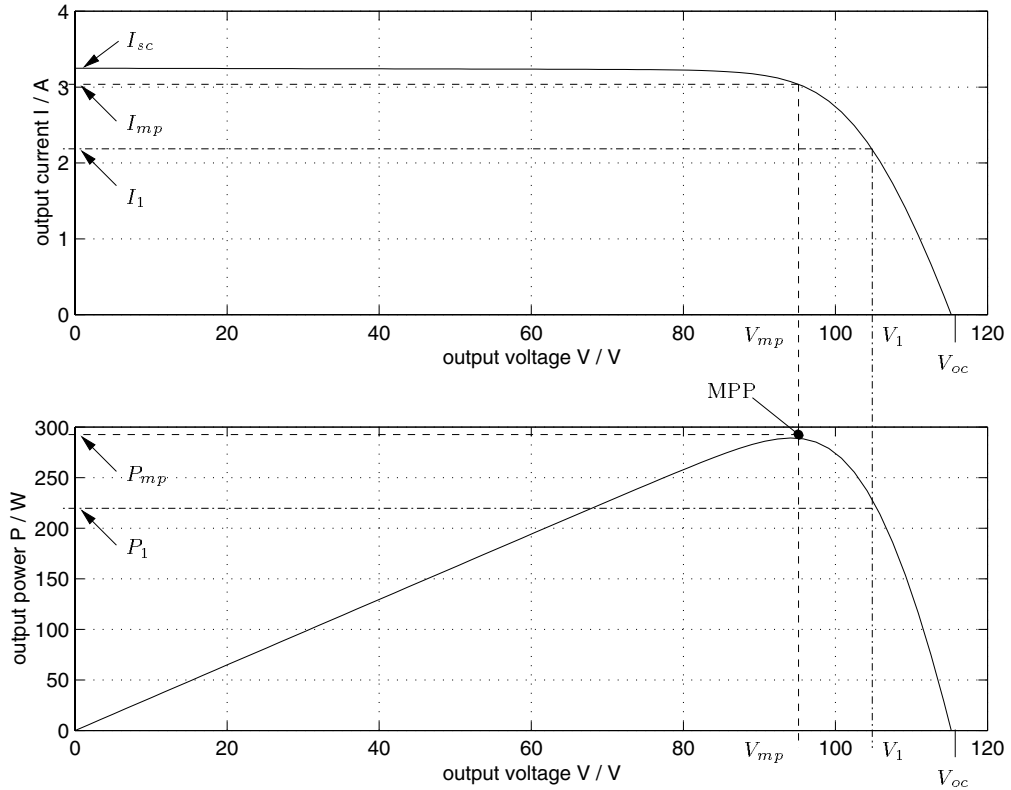


Figure 2.10: Maximum Power Point MPP and the corresponding voltage V_{mp} and current I_{mp} for a photovoltaic cell array with 168 cells in series operating at STC.

Another factor which influences the performance and output power of the solar array is the solar angle of incidence (AOI) effect, also known as the “cosine effect” [GPR90, KE96, Nev78].

As discussed earlier, the generated photo-current I_{ph} depends on the insolation S on the array. The insolation in turn depends on the size of the geometric face of the panel (Figure 2.11). If the sun is at an angle θ with the normal of the panel,

the generated power will decrease with the increase of θ following the cosine law:

$$P = P_0 \cos(\theta), \quad (2.11)$$

where P_0 denotes the output power at normal solar incidence.

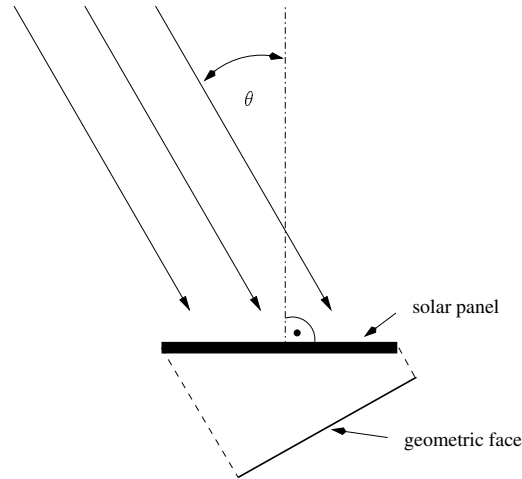


Figure 2.11: Angle of Incidence (AOI) θ and geometric face of a solar array.

Additional factors which influence the light which actually reaches the solar cells include: the surface texture and material of the photovoltaic cell itself, reflection and other optical effects on some transparent material in place to protect the actual cell surface from the environment, and the relative air mass (AM). Relative air mass is the relative path length of the sunlight traveling through the atmosphere and therefore represents the atmospheric influence on the light's spectrum [KE96]. For vertical incidence of sunlight, the air mass is set equal to one. Since this never occurs on most places of our planet, the air mass for standard test conditions (STC) is set to 1.5 as an average representation of ground conditions [FB83].

At the beginning of this section it was mentioned that a solar panel consists of a certain number of photovoltaic cells in series. This is necessary to achieve a rea-

sonably high output voltage at the panel. But considering the photovoltaic cell's equivalent circuit diagram (Figure 2.3 on page 8), the drawback of this configuration becomes clear: as soon as one photovoltaic cell is shaded, it will behave like a diode in reverse direction to the current flow. This results either in almost zero current or, if the voltage is higher than the diode's reverse breakdown voltage, it will eventually even destroy the photovoltaic cell. This can be avoided by placing “bypass” diodes in parallel to the cells (Figure 2.12). It is sufficient to group a number of photovoltaic cells together to be bypassed only by one diode, as long as the voltage of this substring of cells does not exceed the reverse breakdown voltage of one cell of its type [GPR90].

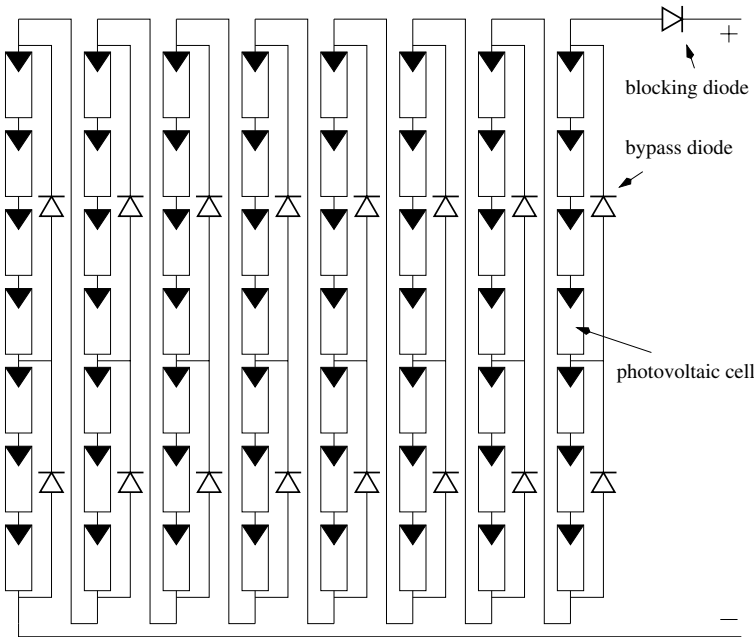


Figure 2.12: Schematic representation of a solar panel as used in the solar car SOLTRAIN.

Additional protective measures indicated in Figure 2.12 are the “blocking” diodes: these diodes are connected in series to the solar array to prevent reverse

current flow through the array in case of low or zero illumination. This current flow can be caused by another power source in the system such as the storage batteries. Without the blocking diodes, a reverse current flow through the idle panel could discharge the batteries and even cause thermal damage to the photovoltaic cells [KOS80].

2.2 Lead-Acid Batteries

In a photovoltaic power supply system, batteries are used as an energy buffer (Figure 2.1). This buffer is necessary because the sun is not consistently available due to a variety of factors: the weather, time of the day, and for vehicles rapidly changing insolation due to vehicle motion. Using the batteries to store the electrical power from the solar panels in the form of chemical energy makes the generated energy readily available whenever it is needed, independent of the current weather conditions and time.

Since the batteries are part of the overall electrical system, it is necessary to include them in the system model. Therefore an equivalent electrical circuit model for the batteries is needed to be able to analyze the dynamic performance and the steady-state behavior of the whole power system.

Lu, Liu, and Wu [LLW95] use a model which was originally developed by Salameh, Casacca, and Lynch in [CS92] and [SCL92] as shown in Figure 2.13. It is an improvement of the commonly used Thevenin equivalent circuit model. The Thevenin model describes the primary behavior of a battery correctly, but does not account for the slowly changing properties of a battery such as the increase and decrease of the operating voltage caused by the process of charging and discharging.

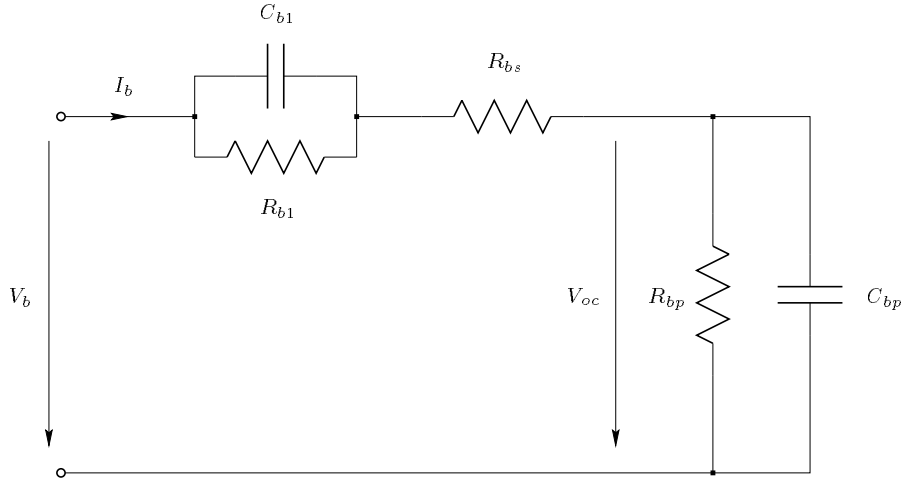


Figure 2.13: Equivalent circuit model of a lead-acid battery.

This new battery model includes equivalent components for all major operating characteristics of a lead-acid battery: The battery's electrochemical energy capacity is represented by the capacitor C_{bp} whose charge is a result of the flow of electrons over time and is linear for constant current conditions in a region of 10–90 percent of the maximum charge level. The value of C_{bp} is derived from the general expression for the energy in a capacitor:

$$E_c = \frac{1}{2}CV_c^2, \quad (2.12)$$

with C being the capacitor's capacity and V_c being its voltage. Unlike a capacitor, a battery's voltage will not be equal to zero at its lowest state of charge. This is equivalent to a capacitor having a minimum charge level equal to the energy $E_{c,min}$. The fully charged battery capacity is represented by a maximum charge level with the energy $E_{c,max}$. This leads to the following equation for the overall

energy storable in a battery [LLW95]:

$$E_b = E_{c,max} - E_{c,min} = \frac{1}{2}CV_{max}^2 - \frac{1}{2}CV_{min}^2 = \frac{1}{2}C_{bp} (V_{max}^2 - V_{min}^2). \quad (2.13)$$

The energy E_b is either given by the manufacturer of the battery directly in kilowatt hours (kWh) or it is specified in ampere hours (Ah — which must be transformed into the units used for energy (kWh) by multiplication with the specified operating voltage). The voltages V_{max} and V_{min} are the battery's maximum charge and minimum charge open circuit voltages respectively. Conversion of equation (2.13) finally leads to an expression for the capacitor representing the battery's charge capacity:

$$C_{bp} = \frac{2E_b}{V_{max}^2 - V_{min}^2}. \quad (2.14)$$

The internal resistance of the battery is represented by the two series resistors R_{bs} and R_{b1} . The bulk electrolyte and plate resistance is represented by the resistor R_{bs} , whereas the resistor R_{b1} represents electrolyte diffusion. R_{b1} also models (together with the small capacitor C_{b1}) the battery's overvoltage or polarization effect [Bod77]. This represents the phenomenon wherein the battery's open circuit voltage drops as soon as a load is connected. Similarly a sudden voltage jump can be observed with the application of a charging current. Using the notation given in Figure 2.13 the overvoltage can be expressed as the difference between the battery open circuit voltage V_{oc} and the battery terminal voltage V_b . R_{b1} and C_{b1} form a parallel RC network with a time constant $\tau = R_{b1}C_{b1}$ so that

$$v_b = v_{oc} + R_{b1} (1 - e^{-t/\tau}) i_b + R_{bs} i_b. \quad (2.15)$$

Another very important characteristic of a battery is self-discharge, represented by the resistor R_{bp} in parallel with the main capacitor C_{bp} . It is caused by elec-

trollysis of water at high voltages and by slow leakage across the battery terminals at low voltages [SCL92].

The circuit in Figure 2.13 describes the characteristics of a lead-acid battery in a comprehensive yet very simplified way: Salameh, Casacca, and Lynch [SCL92] give in their proposal of the model further mathematical expressions used to adjust the model's components with varying temperature to represent the temperature dependency of a battery. They do not account for further dependencies such as the state of charge or the electrolyte level in the battery cells which are additional factors influencing the battery's characteristics.

In the research done by Lu, Liu, and Wu [LLW95] and the accompanying simulations, these complex dependencies are neglected and fixed values are used to represent the equivalent circuit's components. This is sufficient since the battery model is part of an only approximate dynamic model of the overall power supply system used to analyze stability and system performance.

Figure 2.13 may be mathematically expressed in the frequency domain representing the equivalent input impedance of a lead-acid battery:

$$\begin{aligned} Z(s) &= R_{bs} + R_{b1} \parallel C_{b1} + R_{bp} \parallel C_{bp} \\ &= R_{bs} + \frac{R_{b1}}{R_{b1}C_{b1}s + 1} + \frac{R_{bp}}{R_{bp}C_{bp}s + 1}. \end{aligned} \tag{2.16}$$

For usage in the system's mathematical model it is necessary to transform (2.16) into one single term of the following form:

$$Z(s) = \frac{s^2 a_2 + s a_1 + a_0}{s^2 b_2 + s b_1 + b_0}, \tag{2.17}$$

where the coefficients a_i and b_j are used to represent the different circuit compo-

nents:

$$\begin{aligned}
a_2 &= R_{bs}R_{b1}R_{bp}C_{b1}C_{bp}, \\
a_1 &= R_{bs}R_{b1}C_{b1} + R_{bs}R_{bp}C_{bp} + R_{b1}R_{bp}C_{bp} + R_{bp}R_{b1}C_{b1}, \\
a_0 &= R_{bs} + R_{b1} + R_{bp}, \\
b_2 &= R_{b1}R_{bp}C_{b1}C_{bp}, \\
b_1 &= R_{b1}C_{b1} + R_{bp}C_{bp}, \\
b_0 &= 1.
\end{aligned} \tag{2.18}$$

This is the final form of the mathematical battery model as it will be used in the system simulations in Chapter 4.

2.3 DC-DC Converters

In this section the principles of switching power conversion are introduced and details of different DC-DC converter circuits are discussed. The mathematical models for the buck, boost, and buck-boost converter are derived to represent the circuit's steady-state and dynamic behaviors.

A switching converter consists of capacitors, inductors, and switches. All these devices ideally do not consume any power, which is the reason for the high efficiencies of switching converters. The switch is realized with a switched mode semiconductor device, usually a MOSFET. If the semiconductor device is in the off-state, its current is zero and hence its power dissipation is zero. If the device is in the on-state (i.e. saturated), the voltage drop across it will be close to zero and hence the dissipated power will be very small [Eri97].

During the operation of the converter, the switch will be switched at a constant

frequency f_s with an on-time of DT_s , and an off-time of $(1 - D)T_s$, where T_s is the switching period $1/f_s$ and D is the duty ratio of the switch ($D \in [0, 1]$) (see Figure 2.14).

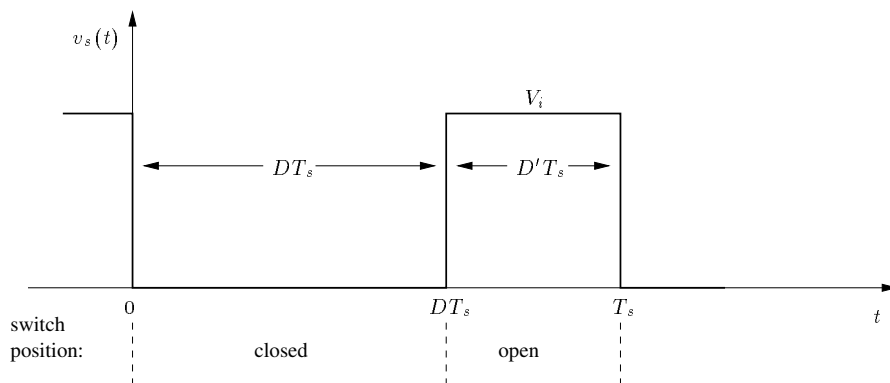


Figure 2.14: Ideal switch voltage $v_s(t)$, duty ratio D , and switching period T_s .

2.3.1 The Buck Converter

The buck converter (Figure 2.15) can be often found in the literature as the step-down converter. This gives a hint of its typical application of converting its input voltage into a lower output voltage, where the conversion ratio $M = V_o/V_i$ varies with the duty ratio D of the switch.

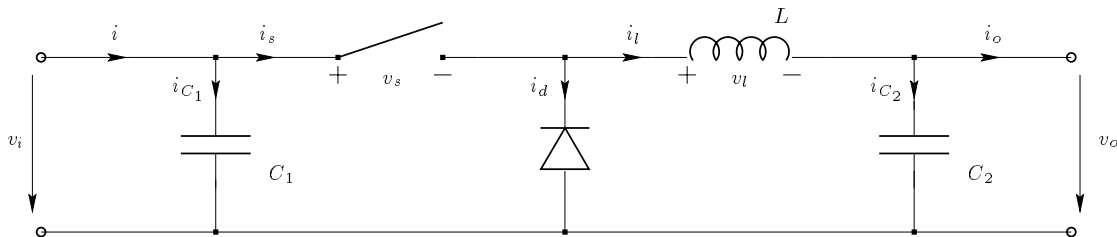


Figure 2.15: Ideal buck converter circuit.

When the switch in Figure 2.15 is closed ($t \in [0, DT_s)$), the diode will be reverse biased and a current flows through the inductor into the load (Figure 2.16). As soon as the switch is open ($t \in [DT_s, T_s)$), the inductor will maintain the current flow to the load, but the loop closes through the now forward biased diode (Figure 2.17).

The equivalent circuit model

To further investigate the buck converter and to derive its mathematical model, the equivalent circuit representation for the two different switch states (open and closed switch) must be analyzed. Figure 2.16 shows the equivalent circuit diagram of a buck converter with the switch closed. Figure 2.17 represents the buck converter with the switch open during the time interval $D'T_s$, where D' denotes the complement of the duty ratio D , defined as

$$D' = 1 - D. \quad (2.19)$$

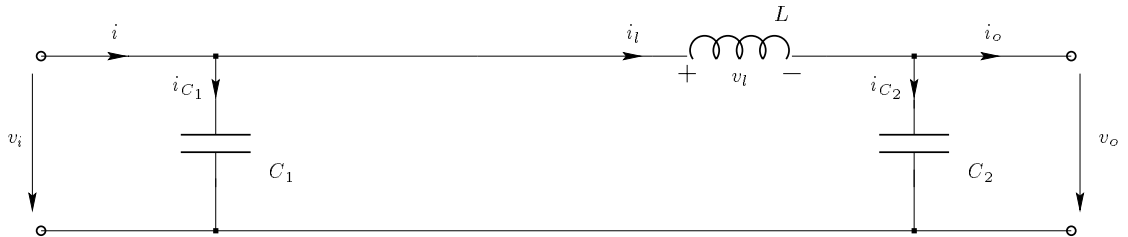


Figure 2.16: Equivalent circuit of a buck converter at closed switch time DT_s .

Applying Kirchhoff's law to the circuit in Figure 2.16 (switch closed) leads to

the following set of equations:

$$i_{C_1}(t) = C_1 \frac{dv_i(t)}{dt} = i(t) - i_l(t), \quad (2.20)$$

$$i_{C_2}(t) = C_2 \frac{dv_o(t)}{dt} = i_l(t) - i_o(t), \quad (2.21)$$

$$v_l(t) = L \frac{di_l(t)}{dt} = v_i(t) - v_o(t). \quad (2.22)$$

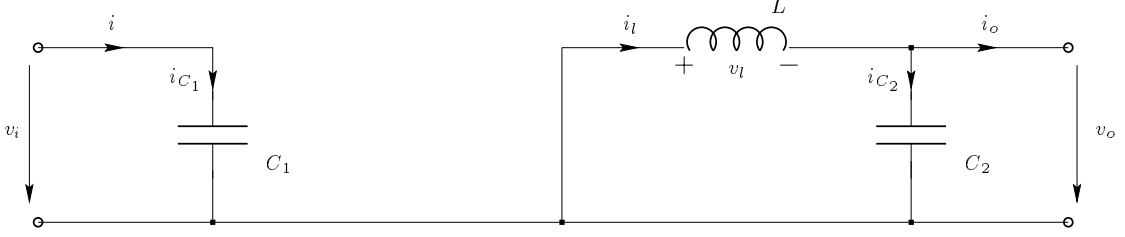


Figure 2.17: Equivalent circuit of a buck converter at open switch time $D'T_s$.

Using Kirchoff's law on Figure 2.17 (switch open), a second set of equations is obtained:

$$i_{C_1}(t) = C_1 \frac{dv_i(t)}{dt} = i(t), \quad (2.23)$$

$$i_{C_2}(t) = C_2 \frac{dv_o(t)}{dt} = i_l(t) - i_o(t), \quad (2.24)$$

$$v_l(t) = L \frac{di_l(t)}{dt} = -v_o(t). \quad (2.25)$$

These are the basic equations used to derive all the mathematical models describing the various properties of the buck converter.

Small-ripple approximation

Every variable in equations (2.20) to (2.25) has a dc value plus a ripple component. This can be expressed in general by

$$x(t) = X + x_{ripple}(t), \quad (2.26)$$

where X represents the dc component of $x(t)$ which is equivalent to its average value $\langle x(t) \rangle$, while $x_{ripple}(t)$ denotes the signal's ripple.

For a well-designed converter, the magnitude of the ripple will be much smaller than the dc component [Eri97]:

$$\|x_{ripple}(t)\| \ll X. \quad (2.27)$$

Therefore the ripple can be neglected and the signal can be approximated by its dc component:

$$x(t) \approx X = \langle x \rangle. \quad (2.28)$$

This approximation is called the *small-ripple approximation* or the *linear-ripple approximation* and makes the mathematical analysis of switching converters much easier. Equations (2.20) to (2.25) can now be rewritten; for DT_s the resulting equations are

$$i_{C_1} = I - I_l, \quad (2.29)$$

$$i_{C_2} = I_l - I_o, \quad (2.30)$$

$$v_l = V_i - V_o, \quad (2.31)$$

and similarly for $D'T_s$:

$$i_{C_1} = I, \quad (2.32)$$

$$i_{C_2} = I_l - I_o, \quad (2.33)$$

$$v_l = -V_o. \quad (2.34)$$

Volt-second balance and charge-balance

The dc values of the inductor voltage and the capacitor current deserve a closer inspection. They are defined as the average of their original signal:

$$V_l = \langle v_l \rangle = \frac{1}{T_s} \int_0^{T_s} v_l(t) dt, \quad (2.35)$$

$$I_c = \langle i_c \rangle = \frac{1}{T_s} \int_0^{T_s} i_c(t) dt. \quad (2.36)$$

Use of the relations $v_l = L \frac{di_l}{dt}$ and $i_c = C \frac{dv_c}{dt}$ yields:

$$i_l(T_s) - i_l(0) = \frac{1}{L} \int_0^{T_s} v_l(t) dt, \quad (2.37)$$

$$v_c(T_s) - v_c(0) = \frac{1}{C} \int_0^{T_s} i_c(t) dt. \quad (2.38)$$

If steady-state operation is assumed, the initial and final values for one switching period must be equal:

$$i_l(t + T_s) = i_l(t), \quad (2.39)$$

$$v_c(t + T_s) = v_c(t). \quad (2.40)$$

These conditions are called *inductor volt-second balance* and *capacitor charge balance* respectively [Eri97]; it is now possible to rewrite equations (2.37) and (2.38) as follows:

$$0 = \frac{1}{L} \int_0^{T_s} v_l(t) dt, \quad (2.41)$$

$$0 = \frac{1}{C} \int_0^{T_s} i_c(t) dt. \quad (2.42)$$

Comparing equations (2.41) and (2.42) with the definition for the average values of v_l and i_c in (2.35) and (2.36), it is apparent that the dc values for the inductor

voltage and capacitor current must be zero:

$$V_i = \langle v_l \rangle = \frac{1}{T_s} \int_0^{T_s} v_l(t) dt = 0, \quad (2.43)$$

$$I_c = \langle i_c \rangle = \frac{1}{T_s} \int_0^{T_s} i_c(t) dt = 0. \quad (2.44)$$

This conclusion will be used in the next section to derive the dc model of the converter.

Steady-state dc characteristics and conversion ratio

Equations (2.31) and (2.34) motivate the construction of the inductor voltage using the small-ripple approximation as shown in Figure 2.18.

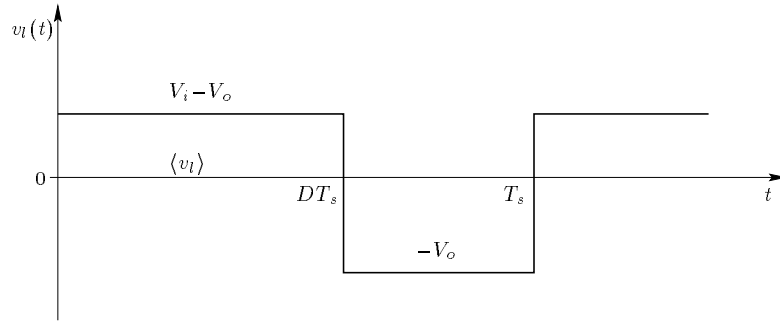


Figure 2.18: Waveform of the inductor voltage $v_l(t)$ for an ideal buck converter.

The expression for the average inductor voltage can be easily derived from the waveform in Figure 2.18. According to the principle of inductor volt-second balance the average inductor voltage is equal to zero in the steady-state case so

$$\langle v_l(t) \rangle = D(V_i - V_o) + D'(-V_o) = 0. \quad (2.45)$$

Using equations (2.29)–(2.30) and (2.32)–(2.33) and applying the principle of

capacitor charge balance leads to the expressions for the average capacitor currents:

$$\langle i_{C_1}(t) \rangle = D(I - I_l) + D'I = 0, \quad (2.46)$$

$$\langle i_{C_2}(t) \rangle = D(I_l - I_o) + D'(I_l - I_o) = 0. \quad (2.47)$$

Further conversion of (2.45)–(2.47) combined with (2.19) leads to three simple equations which describe the steady-state dc characteristics of a buck converter:

$$DV_i = V_o, \quad (2.48)$$

$$I = DI_l, \quad (2.49)$$

$$I_l = I_o, \quad (2.50)$$

where (2.48) yields the conversion ratio $M(D)$ of the buck converter

$$M(D) = \frac{V_o}{V_i} = D. \quad (2.51)$$

Figure 2.19 illustrates this linear relation.

Determination of the voltage and current ripple

While the output voltage ripple amplitude Δv_o usually ranges within 1% of the dc component V_o , the amplitude of the inductor current ripple Δi_l varies by as much as 10% to 20% of its dc value I_l [Eri97]. This is important to know, because the inductor current ripple is determined by the value of the inductance L . If the ripple gets too large, the size of the switching semiconductor device must be increased to handle the high current peaks. Increase in size would result in an increase in weight and higher cost. Therefore a more detailed investigation of the inductor current ripple must be done.

Using the well-known relation $v_l = L \frac{di_l}{dt}$ and equation (2.31), which was derived using the method of small-ripple approximation, the following expression is

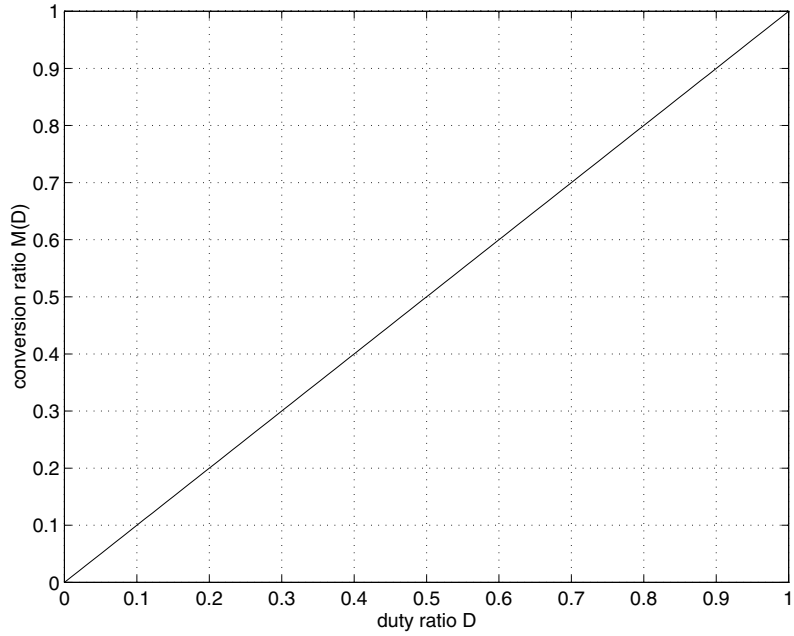


Figure 2.19: Conversion ratio $M(D)$ vs. duty ratio D for an ideal buck converter.

obtained:

$$\frac{di_l}{dt} = \frac{v_l}{L} \approx \frac{V_i - V_o}{L}, \quad (2.52)$$

where $\frac{di_l}{dt}$ represents the slope of the inductor current during the first time interval DT_s of a switching period.

For the second time interval $D'T_s$ with (2.34) the equation becomes:

$$\frac{di_l}{dt} = \frac{v_l}{L} \approx \frac{-V_o}{L}. \quad (2.53)$$

As equations (2.52) and (2.53) show, the small-ripple approximation leads to a linear expression for the slope of the switching ripple, hence its alternative denotation as *linear ripple approximation*.

With the linear expression for $\frac{di_l}{dt}$ (2.52), the equation for the peak-to-peak

current ripple can be easily derived:

$$i_{l_{pp}} = 2\Delta i_l = \frac{V_i - V_o}{L} DT_s. \quad (2.54)$$

Since the converter is assumed to be in equilibrium, it does not make a difference if DT_s or $D'T_s$ is chosen to determine the the ripple amplitude.

Equation (2.54) can now be solved for the inductance L so that a desired current ripple amplitude can be achieved:

$$L = \frac{V_i - V_o}{2\Delta i_l} DT_s. \quad (2.55)$$

To obtain a desired output voltage ripple, a similar approach can be used. With the relation $i_{C_2} = C_2 \frac{dv_{C_2}}{dt}$ and small-ripple approximation (2.30), the following equation is obtained:

$$\frac{dv_{C_2}}{dt} = \frac{i_{C_2}}{C_2} \approx \frac{I_l - I_o}{C_2}, \quad (2.56)$$

where $\frac{dv_{C_2}}{dt}$ is the slope of the output voltage ripple during the time interval DT_s .

This leads to the peak-to-peak output voltage ripple:

$$v_{o_{pp}} = 2\Delta v_o = \frac{I_l - I_o}{C_2} DT_s, \quad (2.57)$$

with Δv_o being the amplitude of the output voltage ripple.

Solving (2.57) for C_2 yields an expression which can be used to choose C_2 as a function of the desired output voltage ripple:

$$C_2 = \frac{I_l - I_o}{2\Delta v_o} DT_s. \quad (2.58)$$

The non-ideal converter model

All previous analysis was based on an ideal converter circuit with 100% efficiency, which means that no component losses were considered. Sources for power

loss can be inductor losses (such as magnetic core and copper losses), equivalent series resistance (ESR) of capacitors, semiconductor conduction losses, and semiconductor switching losses. If all these effects are considered, the mathematical model gets too complex for further analysis.

Inclusion of a resistance R_l to represent inductor losses (while neglecting other sources of power loss) modifies the buck converter model as shown in Figure 2.20.

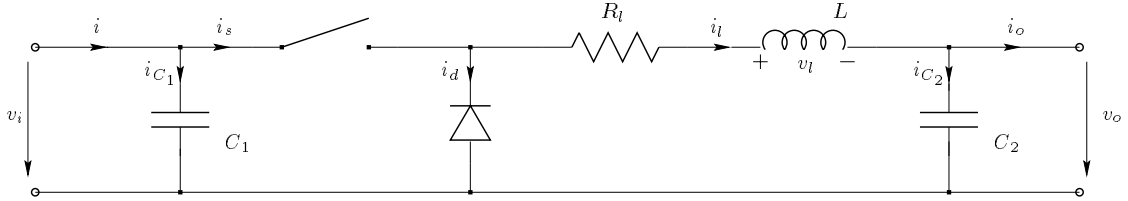


Figure 2.20: Buck converter with series resistor R_l to account for inductor losses.

For the time interval DT_s the equations become:

$$i_{C_1} = I - I_l, \quad (2.59)$$

$$i_{C_2} = I_l - I_o, \quad (2.60)$$

$$v_l = -R_l I_l + V_i - V_o, \quad (2.61)$$

and for $D'T_s$:

$$i_{C_1} = I, \quad (2.62)$$

$$i_{C_2} = I_l - I_o, \quad (2.63)$$

$$v_l = -R_l I_l - V_o. \quad (2.64)$$

Applying the principles of inductor volt-second balance and capacitor charge balance to (2.59)–(2.64), results in modified versions of equations (2.48)–(2.50) as

shown below:

$$DV_i = V_o + R_l I_l, \quad (2.65)$$

$$I = DI_l, \quad (2.66)$$

$$I_l = I_o. \quad (2.67)$$

The converter's efficiency

The inclusion of losses in the converter model yields a new expression for the conversion ratio between input and output voltage:

$$\frac{V_o}{V_i} = \eta M(D), \quad (2.68)$$

where η is the ratio of the converter's output power P_{out} to the input power P_{in} or its efficiency:

$$\eta = \frac{P_{out}}{P_{in}} = \frac{V_o I_o}{V_i I}. \quad (2.69)$$

If equations (2.65), (2.67), and (2.51) are used as substitutions in (2.68), the expression for the conversion ratio can be found as:

$$\frac{V_o}{V_i} = \frac{V_o}{\frac{V_o + R_l I_l}{D}} = \frac{D}{1 + \frac{R_l I_l}{V_o}} = \frac{1}{1 + \frac{R_l I_o}{V_o}} D = \frac{1}{1 + \frac{R_l}{Z}} D = \eta D, \quad (2.70)$$

with $Z = V_o/I_o$ being the complex load of the converter. This leads to a new expression for the efficiency:

$$\eta = \frac{P_{out}}{P_{in}} = \frac{1}{1 + \frac{R_l}{Z}}. \quad (2.71)$$

This means for the special case of the buck converter, the efficiency η is independent of the duty ratio and therefore the conversion ratio is still a linear expression of D . The influence of the load impedance on the efficiency of the converter represents the fact that a larger load causes a higher power transfer through the converter and therefore higher losses.

The small-signal ac model

All equations derived in the previous sections represent only the buck converter's steady-state dc behavior. To obtain a model of its dynamic characteristics a small signal ac analysis is necessary.

As discussed before, the switching ripple of a well-designed converter can be neglected in the modeling process. The variations which are now investigated are underlying ac variations in the converter waveforms. This means that the averaged signal $\langle x(t) \rangle$, which is derived by small-ripple approximation, is assumed to actually consist of its steady-state or quiescent value X plus some superimposed small ac variations $\hat{x}(t)$:

$$\langle x(t) \rangle = X + \hat{x}(t). \quad (2.72)$$

All the signals and waveforms of the converter can therefore be rewritten as follows:

$$\begin{aligned} d(t) &= D + \hat{d}(t), \\ \langle v_i(t) \rangle &= V_i + \hat{v}_i(t), \\ \langle i(t) \rangle &= I + \hat{i}(t), \\ \langle v_o(t) \rangle &= V_o + \hat{v}_o(t), \\ \langle i_o(t) \rangle &= I_o + \hat{i}_o(t), \\ \langle i_l(t) \rangle &= I_l + \hat{i}_l(t). \end{aligned} \quad (2.73)$$

If these equations are substituted into the averaged equations (2.45) to (2.47) for

the buck converter, recalled as

$$\begin{aligned}
L \frac{d\langle i_l(t) \rangle}{dt} &= d(t)\langle v_i(t) \rangle - \langle v_o(t) \rangle, \\
C_1 \frac{d\langle v_i(t) \rangle}{dt} &= \langle i(t) \rangle - d(t)\langle i_l(t) \rangle, \\
C_2 \frac{d\langle v_o(t) \rangle}{dt} &= \langle i_l(t) \rangle - \langle i_o(t) \rangle,
\end{aligned} \tag{2.74}$$

the following model can be derived:

$$L \frac{d(I_l + \hat{i}_l(t))}{dt} = (D + \hat{d}(t))(V_i + \hat{v}_i(t)) - (V_o + \hat{v}_o(t)), \tag{2.75}$$

$$C_1 \frac{d(V_i + \hat{v}_i(t))}{dt} = I + \hat{i}(t) - (D + \hat{d}(t))(I_l + \hat{i}_l(t)), \tag{2.76}$$

$$C_2 \frac{d(V_o + \hat{v}_o(t))}{dt} = I_l + \hat{i}_l(t) - (I_o + \hat{i}_o(t)). \tag{2.77}$$

Since a small ac variation is added to the quiescent operating point value, this step is called perturbation. After multiplying out equations (2.75)–(2.77) and arranging the different terms according to their order, the expression for the inductor voltage (2.75) will appear as follows:

$$L \left(\frac{dI_l}{dt} + \frac{d\hat{i}_l(t)}{dt} \right) = \underbrace{DV_i - V_o}_{\text{dc terms}} + \underbrace{D\hat{v}_i(t) + V_i\hat{d}(t) - \hat{v}_o(t)}_{\text{1st-order ac terms}} + \underbrace{\hat{d}(t)\hat{v}_i(t)}_{\text{2nd-order ac term}}. \tag{2.78}$$

This equation is nonlinear because it contains a second-order ac term. Assuming the ac variations are very small in magnitude compared to the dc steady-state values, then

$$\|\hat{x}(t)\| \ll X. \tag{2.79}$$

Thus, equation (2.78) can be linearized by simply neglecting the second order term. Since the derivative of a constant is equal to zero, the dc term is also eliminated. This leaves a linear expression containing only the first-order ac variations such

that equation (2.78) can be rewritten as

$$L \frac{d\hat{i}_l(t)}{dt} = D\hat{v}_i(t) + V_i\hat{d}(t) - \hat{v}_o(t). \quad (2.80)$$

Expressions (2.76) and (2.77) for the capacitor currents can be similarly linearized using the small-signal assumption:

$$C_1 \frac{d\hat{v}_i(t)}{dt} = \hat{i}(t) - D\hat{i}_l(t) - \hat{d}(t)I_l, \quad (2.81)$$

$$C_2 \frac{d\hat{v}_o(t)}{dt} = \hat{i}_l(t) - \hat{i}_o(t). \quad (2.82)$$

Equations (2.80) to (2.82) represent the small-signal ac model of a buck converter and therefore are sufficient to describe the converter dynamics caused by nonlinear components such as capacitors and inductors.

2.3.2 The Boost Converter

The principles of small ripple approximation, inductor volt-second balance, and capacitor charge balance introduced in section 2.3.1 can be used in any switching converter to find its steady-state voltages and currents.

The boost converter, as shown in Figure 2.21, is also known as the step-up converter. The name implies its typical application of converting a low input-voltage to a high output-voltage, essentially functioning like a reversed buck converter.

The equivalent circuit model

During the first time interval DT_s of the switching period T_s , the closed switch connects the input through the inductor to ground and a high current starts to flow. The diode is reverse biased so no inductor current flows through the load (Figure 2.22). After the switch is opened in the second time interval $D'T_s$ of the

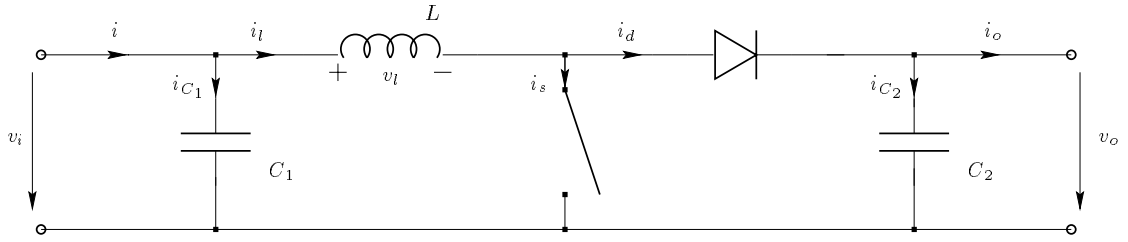


Figure 2.21: Ideal boost converter circuit.

switching period (Figure 2.23), the nature of the inductor objects to the discontinuity in the current flow, and the high current through the now forward biased diode leads to a high voltage rise which is applied across the load.

To derive the boost converter's steady state transfer-functions and the expression for its conversion ratio $M(D)$, the two different time intervals DT_s and $D'T_s$ for the switching period T_s must be considered.

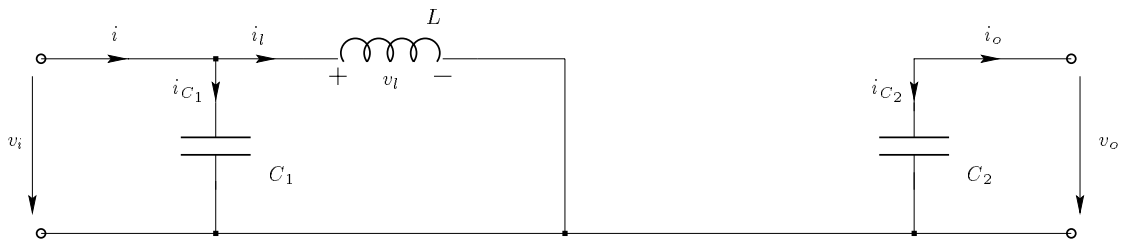


Figure 2.22: Equivalent circuit of a boost converter at closed switch time DT_s .

Figure 2.22 shows the equivalent circuit of a boost converter during the time interval DT_s , when the switch is closed. Application of Kirchhoff's circuit equations

leads to the following set of expressions for DT_s :

$$\begin{aligned}
 i_{C_1}(t) &= C_1 \frac{dv_i(t)}{dt} = i(t) - i_l(t), \\
 i_{C_2}(t) &= C_2 \frac{dv_o(t)}{dt} = -i_o(t), \\
 v_l(t) &= L \frac{di_l(t)}{dt} = v_i(t).
 \end{aligned}
 \tag{2.83}$$

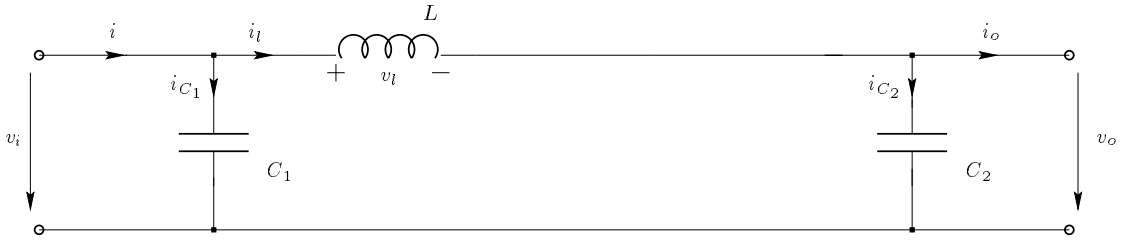


Figure 2.23: Equivalent circuit of a boost converter at open switch time $D'T_s$.

For the time period of the open switch $D'T_s$ shown in Figure 2.23 a second set of equations can be derived:

$$\begin{aligned}
 i_{C_1}(t) &= C_1 \frac{dv_i(t)}{dt} = i(t) - i_l(t), \\
 i_{C_2}(t) &= C_2 \frac{dv_o(t)}{dt} = i_l(t) - i_o(t), \\
 v_l(t) &= L \frac{di_l(t)}{dt} = v_i(t) - v_o(t).
 \end{aligned}
 \tag{2.84}$$

Steady-state dc characteristics and conversion ratio

The small ripple approximation as discussed on page 27 makes it possible to neglect the switching ripple in the converter signals and replace them by their

average values (2.28). This simplifies equations (2.83) to

$$\begin{aligned} i_{C_1} &= I - I_l, \\ i_{C_2} &= -I_o, \\ v_l &= V_i, \end{aligned} \tag{2.85}$$

and (2.84) to

$$\begin{aligned} i_{C_1} &= I - I_l, \\ i_{C_2} &= I_l - I_o, \\ v_l &= V_i - V_o. \end{aligned} \tag{2.86}$$

To find the averaged values for i_{C_1} , i_{C_2} , and v_l over an entire switching period T_s equations (2.85) and (2.86) are substituted into (2.87):

$$\begin{aligned} \langle x(t) \rangle &= \frac{1}{T_s} \int_t^{t+T_s} x(\tau) d\tau \\ &= \frac{1}{T_s} \left[\int_t^{t+DT_s} x \Big|_{[0,DT_s)}(\tau) d\tau + \int_{t+DT_s}^{t+T_s} x \Big|_{[DT_s,T_s)}(\tau) d\tau \right]. \end{aligned} \tag{2.87}$$

Application of the principle of inductor volt-second balance and capacitor charge balance as introduced in section 2.3.1 on page 28 finally yields the averaged dc model of a boost converter:

$$\begin{aligned} \langle i_{C_1}(t) \rangle &= D(I - I_l) + D'(I - I_l) = 0, \\ \langle i_{C_2}(t) \rangle &= D(-I_o) + D'(I_l - I_o) = 0, \\ \langle v_l(t) \rangle &= DV_i + D'(V_i - V_o) = 0. \end{aligned} \tag{2.88}$$

With $D' = 1 - D$ (2.19), this can be further simplified to a final set of equations

describing the steady-state dc characteristics:

$$I = I_l, \quad (2.89)$$

$$I_o = D'I_l, \quad (2.90)$$

$$V_i = D'V_o, \quad (2.91)$$

where (2.91) yields the conversion ratio $M(D)$ of the ideal boost converter:

$$M(D) = \frac{V_o}{V_i} = \frac{1}{D'} = \frac{1}{1-D}. \quad (2.92)$$

Figure 2.24 illustrates this relation for the step-up converter.

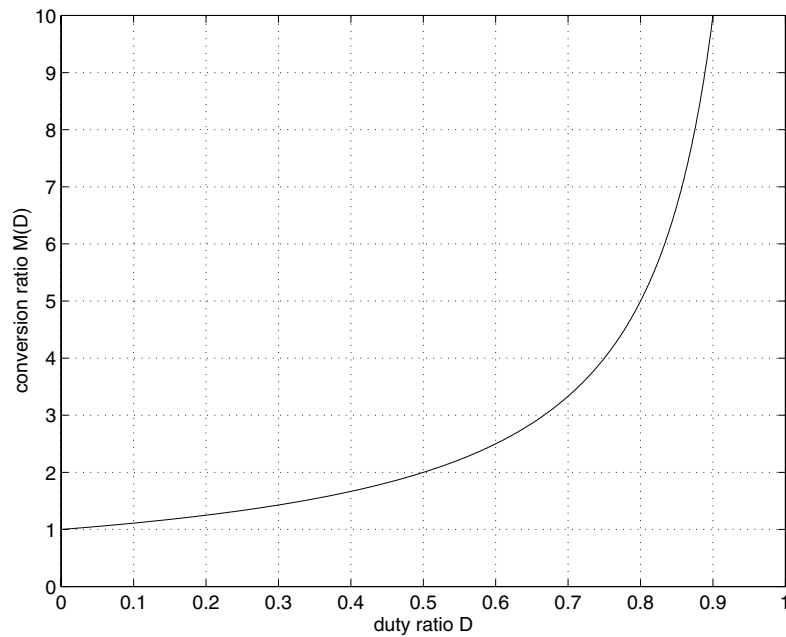


Figure 2.24: Conversion ratio $M(D)$ vs. duty ratio D for an ideal boost converter.

Determination of voltage and current ripple

For the boost converter, as for the buck converter in section 2.3.1, a linear ripple approximation is made for the output voltage ripple Δv_o , the input voltage

ripple Δv_i , and for the inductor current ripple Δi_l . This makes it possible to derive expressions to dimension the circuit components according to specified ripple limitations.

With equations (2.83) and (2.85) a linear approximation of the slopes of the aforementioned ripples is given as

$$\begin{aligned}\frac{dv_{C_1}}{dt} &= \frac{i_{C_1}}{C_1} \approx \frac{I - I_l}{C_1}, \\ \frac{dv_{C_2}}{dt} &= \frac{i_{C_2}}{C_2} \approx \frac{-I_o}{C_2}, \\ \frac{di_l}{dt} &= \frac{v_l}{L} \approx \frac{V_i}{L},\end{aligned}\tag{2.93}$$

where $\frac{dv_{C_1}}{dt}$, $\frac{dv_{C_2}}{dt}$, $\frac{di_l}{dt}$ are the slopes of the input voltage ripple, the output voltage ripple, and the inductor current ripple during the first time interval DT_s , respectively. With these linear equations it is easy to express the peak-to-peak ripple:

$$\begin{aligned}v_{i_{pp}} &= 2\Delta v_i = \frac{I - I_l}{C_1} DT_s, \\ v_{o_{pp}} &= 2\Delta v_o = \frac{-I_o}{C_2} DT_s, \\ i_{l_{pp}} &= 2\Delta i_l = \frac{V_i}{L} DT_s.\end{aligned}\tag{2.94}$$

Solving (2.94) for the appropriate component values results in a set of equations which make it possible to design a converter according to given ripple specifications:

$$\begin{aligned}C_1 &= \frac{I - I_l}{2\Delta v_i} DT_s, \\ C_2 &= \frac{-I_o}{2\Delta v_o} DT_s, \\ L &= \frac{V_i}{2\Delta i_l} DT_s.\end{aligned}\tag{2.95}$$

The non-ideal converter model

One important issue when designing a high efficiency switching converter is to determine the dependency of the conversion ratio on the losses occurring in the real, non-ideal components. As in the buck converter example in section 2.3.1, only the dependency on the inductor losses is analyzed. Figure 2.25 shows an equivalent circuit diagram for a boost converter with inductor losses indicated by a series resistor R_l .

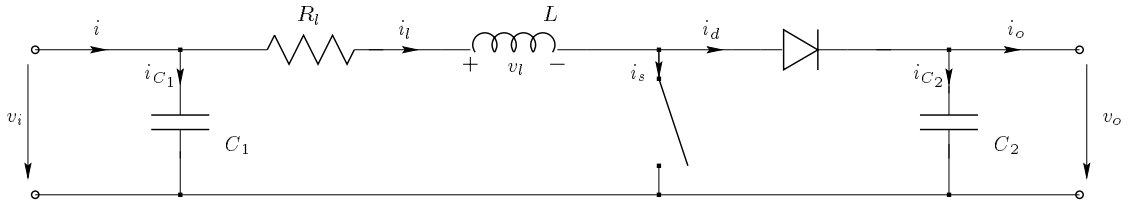


Figure 2.25: Boost converter with series resistor R_l to account for inductor losses.

The inclusion of inductor losses leads to a new set of system equations for the boost converter. With the application of the small ripple approximation, the equations for the time interval DT_s are:

$$\begin{aligned} i_{C_1} &= I - I_l, \\ i_{C_2} &= -I_o, \\ v_l &= -R_l I_l + V_i, \end{aligned} \tag{2.96}$$

and for $D'T_s$

$$\begin{aligned} i_{C_1} &= I - I_l, \\ i_{C_2} &= I_l - I_o, \\ v_l &= -R_l I_l + V_i - V_o. \end{aligned} \tag{2.97}$$

With the principles of inductor volt-second balance and capacitor charge balance, equations (2.96) and (2.97) yield a new steady-state averaged model for the boost converter, which accounts for losses in the inductor:

$$\begin{aligned} I &= I_l, \\ I_o &= D'I_l, \\ V_i &= R_l I_l + D'V_o. \end{aligned} \tag{2.98}$$

The converter's efficiency

If losses are taken into consideration, the efficiency η of the converter has an influence on its conversion ratio V_o/v_i (2.68). Using (2.92) and the efficiency equation (the ratio between output and input power) leads to

$$\frac{V_o}{V_i} = \frac{V_o}{D'V_o + R_l I_l} = \frac{\frac{1}{D'}}{1 + \frac{R_l I_l}{D'V_o}} = \frac{\frac{1}{D'}}{1 + \frac{R_l I_o}{D'^2 V_o}} = \frac{1}{1 + \frac{R_l}{D'^2 Z}} \frac{1}{D'} = \eta M(D), \tag{2.99}$$

with $Z = V_o/I_o$ being the complex load of the converter. This yields

$$\eta = \frac{1}{1 + \frac{R_l}{D'^2 Z}}. \tag{2.100}$$

Like the buck converter equation (2.99) shows that the efficiency and the conversion ratio not only become dependent on parasitic effects of the circuit components, but also on the actual load of the converter. This is understandable since a higher load causes a higher power transfer through the converter and therefore greater losses in non-ideal components.

However, unlike the buck converter, the relation (2.100) shows that the efficiency of the boost converter depends on the duty ratio D , or more appropriately, its complement D' (2.19). This causes the conversion ratio V_o/v_i to be a nonlinear function of D . Figure 2.26 shows this dependency of the converter's conversion

ratio on the duty cycle D and shows how the ratio R_l/z determines the maximum possible step between input and output voltage.

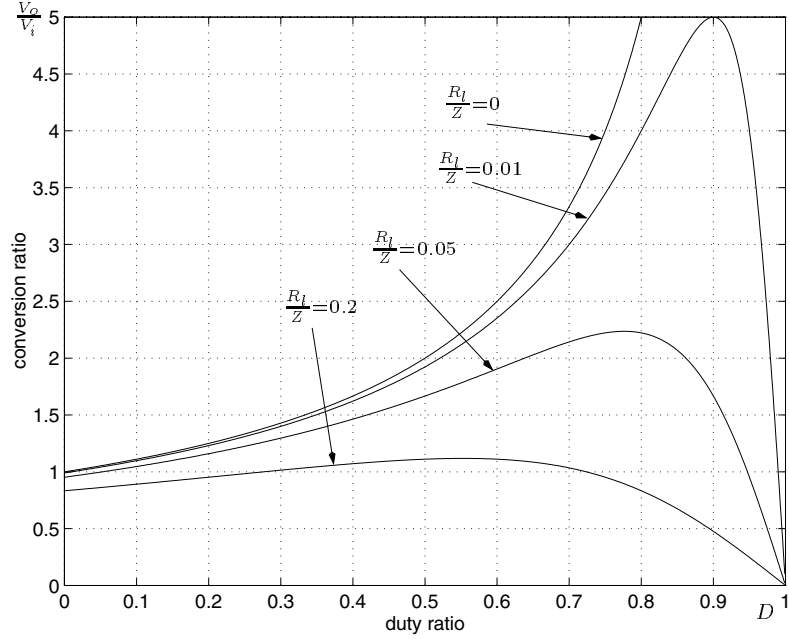


Figure 2.26: Conversion ratio V_o/V_i vs. duty ratio D for a non-ideal boost converter dependent on R_l/z .

The design requires a high efficiency of a solar power system. Therefore it is important to know how the conversion ratio of the utilized converter influences its efficiency. To find this relation, the inverse of (2.99) must be found to form a function $\eta(V_o/V_i)$. This requires several steps: The inverse of (2.100) is found to be:

$$D' = \sqrt{\frac{R_l}{Z} \cdot \frac{\eta}{1-\eta}}, \quad (2.101)$$

where the positive root has been selected, since $D' \in (0, 1)$. (2.101) is then substituted into (2.99):

$$\frac{V_o}{V_i} = \eta \frac{1}{D'} = \eta \sqrt{\frac{1}{R_l/z} \cdot \frac{1-\eta}{\eta}} = \sqrt{\frac{\eta(1-\eta)}{R_l/z}}. \quad (2.102)$$

The inverse of (2.102) is then the desired function $\eta(V_o/V_i)$:

$$\eta(V_o/V_i) = \frac{1}{2} \pm \sqrt{\frac{1}{4} - \frac{R_l}{Z} (V_o/V_i)^2}. \quad (2.103)$$

Because a converter is operating at its maximum efficiency if $V_o/V_i = 1$, the positive root of (2.103) is selected to plot the graph in Figure 2.27.

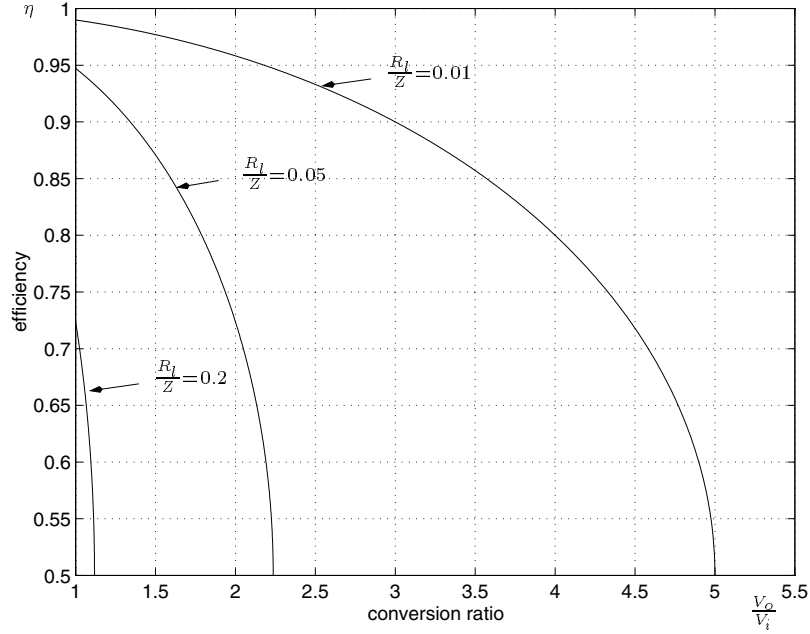


Figure 2.27: Efficiency η vs. conversion ratio V_o/V_i for a non-ideal boost converter dependent on R_l/Z .

The plot in Figure 2.27 shows how the maximum possible conversion ratio depends on the factor R_l/Z . This limitation originates from the second term of equation (2.103) and can be expressed as:

$$\frac{V_o}{V_i} \leq \frac{1}{2} \sqrt{\frac{1}{R_l/Z}}. \quad (2.104)$$

Such a limitation of the conversion ratio as in (2.104) did not occur for the buck converter (section 2.3.1). This can be explained by the fact that the buck con-

verter's efficiency only depends on R_l/z but not on the duty ratio D (2.71). This will play a role for the choice of converter in the final photovoltaic power system.

The small-signal ac model

The small-signal ac model describes the dynamic behavior of the converter. To obtain the ac model equations the given expressions for the dc model (2.88) are perturbed using (2.73). For the boost converter this yields:

$$\begin{aligned} C_1 \frac{d(V_i + \hat{v}_i(t))}{dt} &= I + \hat{i}(t) - (I_l + \hat{i}_l(t)), \\ C_2 \frac{d(V_o + \hat{v}_o(t))}{dt} &= (D' - \hat{d}(t))(I_l + \hat{i}_l(t)) - (I_o + \hat{i}_o(t)), \\ L \frac{d(I_l + \hat{i}_l(t))}{dt} &= V_i + \hat{v}_i(t) - (D' - \hat{d}(t))(V_o + \hat{v}_o(t)). \end{aligned} \quad (2.105)$$

Using the definition of the complement of the duty ratio (2.19), the perturbed signal of $d'(t)$ is given as

$$d'(t) = 1 - d(t) = 1 - (D + \hat{d}(t)) = D' - \hat{d}(t). \quad (2.106)$$

This avoids the problem of having an additional variable, $\hat{d}'(t)$, in the final system of equations .

If the different terms in (2.105) are multiplied out and the new terms are sorted according to their order, the system appears as follows:

$$\begin{aligned} C_1 \left(\frac{dV_i}{dt} + \frac{d\hat{v}_i(t)}{dt} \right) &= I - I_l + \hat{i}(t) - \hat{i}_l(t), \\ C_2 \left(\frac{dV_o}{dt} + \frac{d\hat{v}_o(t)}{dt} \right) &= D'I_l - I_o + D'\hat{i}_l(t) - \hat{d}(t)I_l - \hat{i}_o(t) - \hat{d}(t)\hat{i}_l(t), \\ L \left(\frac{dI_l}{dt} + \frac{d\hat{i}_l(t)}{dt} \right) &= \underbrace{V_i - D'V_o}_{\text{dc terms}} + \underbrace{\hat{v}_i(t) - D'\hat{v}_o(t) + \hat{d}(t)V_o}_{\text{1st-order ac terms}} + \underbrace{\hat{d}(t)\hat{v}_o(t)}_{\text{2nd-order ac terms}}. \end{aligned} \quad (2.107)$$

This is a set of nonlinear equations. Assuming that the ac variations $\hat{x}(t)$ are much smaller than the steady-state values of the signal (2.79), this system can be linearized by neglecting the second order terms. If the terms on the right side are equated to the terms on the left side of the equation, a set of linear system equations remains:

$$\begin{aligned} C_1 \frac{d\hat{v}_i(t)}{dt} &= \hat{i}(t) - \hat{i}_l(t), \\ C_2 \frac{d\hat{v}_o(t)}{dt} &= D'\hat{i}_l(t) - \hat{d}(t)I_l - \hat{i}_o(t), \\ L \frac{d\hat{i}_l(t)}{dt} &= \hat{v}_i(t) - D'\hat{v}_o(t) + \hat{d}(t)V_o. \end{aligned} \quad (2.108)$$

Since the derivative of a constant is equal to zero, the dc terms are also eliminated. This result is consistent with the principles of inductor volt-second balance and capacitor charge balance.

2.3.3 The Buck-Boost Converter

The buck-boost converter combines the properties of the buck and boost configurations. It can be used to ideally transform any dc input voltage into any desired dc output voltage. In practical usage the ideality is of course limited by component losses.

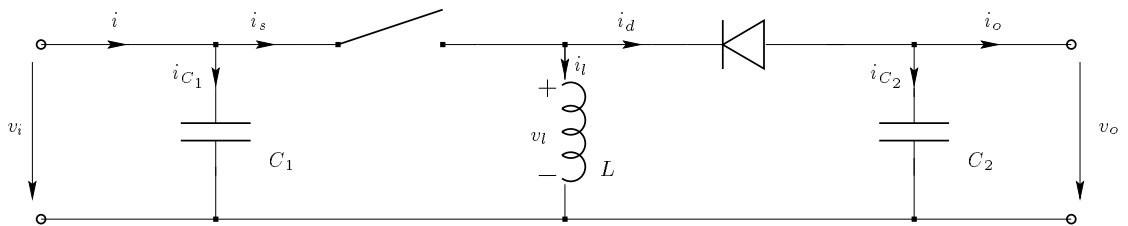


Figure 2.28: Ideal buck-boost converter circuit.

The equivalent circuit model

Figure 2.28 shows the ideal equivalent circuit diagram of the buck-boost converter. If the switch is closed during the first time interval DT_s of the switching period T_s , a current starts flowing from the input source through the inductor to ground (Figure 2.29). After the switch opens at the beginning of the second time interval $D'T_s$, this current flow is maintained by the nature of the inductor. The current loop closes through the load and the diode (Figure 2.30). Since the current is forced to flow “backwards” through the load, the output voltage V_o of the buck-boost converter is negative. Variation of the duty ratio D will vary the conversion ratio between output and input voltage V_o/V_i .

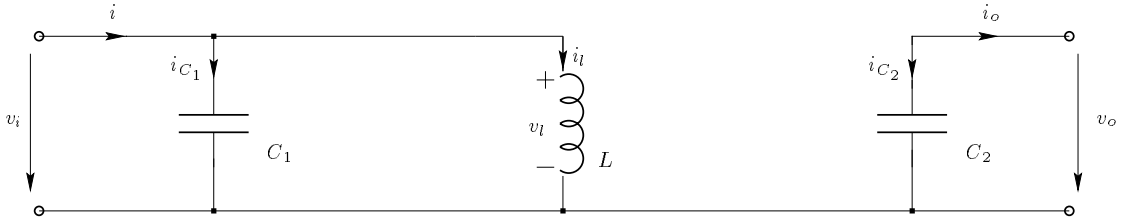


Figure 2.29: Equivalent circuit of a buck-boost converter at closed switch time DT_s .

Application of Kirchhoff's law and node equations to the circuit in the first switch state shown in Figure 2.29 yields the first part of the system equations for the time period DT_s :

$$\begin{aligned}
 i_{C_1}(t) &= C_1 \frac{dv_i(t)}{dt} = i(t) - i_l(t), \\
 i_{C_2}(t) &= C_2 \frac{dv_o(t)}{dt} = -i_o(t), \\
 v_l(t) &= L \frac{di_l(t)}{dt} = v_i(t),
 \end{aligned} \tag{2.109}$$

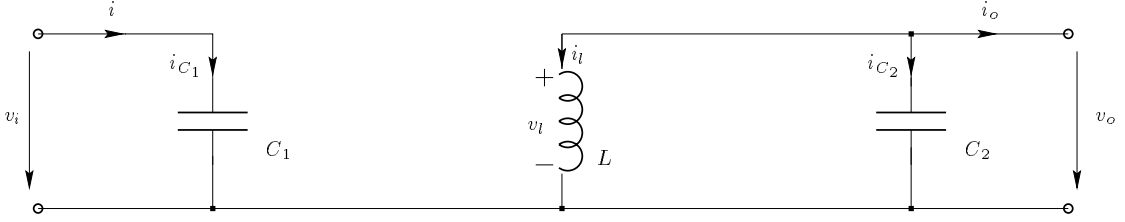


Figure 2.30: Equivalent circuit of a buck-boost converter at open switch time $D'T_s$.

and for the second time period $D'T_s$, after Figure 2.30:

$$\begin{aligned}
 i_{C_1}(t) &= C_1 \frac{dv_i(t)}{dt} = i(t), \\
 i_{C_2}(t) &= C_2 \frac{dv_o(t)}{dt} = -i_l(t) - i_o(t), \\
 v_l(t) &= L \frac{di_l(t)}{dt} = v_o(t).
 \end{aligned} \tag{2.110}$$

Steady-state dc characteristics and conversion ratio

The small ripple approximation (2.27) makes it possible to replace the time dependent variables in (2.109) and (2.110) with their average values (2.28). This yields for DT_s :

$$\begin{aligned}
 i_{C_1} &= I - I_l, \\
 i_{C_2} &= -I_o, \\
 v_l &= V_i,
 \end{aligned} \tag{2.111}$$

and for $D'T_s$:

$$\begin{aligned}
 i_{C_1} &= I, \\
 i_{C_2} &= -I_l - I_o, \\
 v_l &= V_o.
 \end{aligned} \tag{2.112}$$

Inductor volt-second balance and capacitor charge balance as discussed on page 28 in section 2.3.1 lead with (2.87) to:

$$\begin{aligned}\langle i_{C_1}(t) \rangle &= D(I - I_l) + D'I = 0, \\ \langle i_{C_2}(t) \rangle &= D(-I_o) + D'(-I_l - I_o) = 0, \\ \langle v_l(t) \rangle &= DV_i + D'V_o = 0.\end{aligned}\tag{2.113}$$

The steady-state averaged model for the ideal buck-boost converter can now be derived by multiplying out equations (2.113). This yields with $D' = 1 - D$ (2.19)

$$I = DI_l,\tag{2.114}$$

$$I_o = -D'I_l,\tag{2.115}$$

$$DV_i = -D'V_o,\tag{2.116}$$

where (2.116) yields the dc conversion ratio $M(D)$ of the ideal buck-boost converter:

$$M(D) = \frac{V_o}{V_i} = -\frac{D}{D'} = -\frac{D}{1-D}.\tag{2.117}$$

Figure 2.31 illustrates the conversion ratio of a buck-boost converter as a plot over the duty ratio D .

Determination of voltage and current ripple

A linear ripple approximation is done, like previously discussed converter types, to determine equations which make it easier to design a converter which will meet desired maximum switching ripple specifications. It is assumed that the slope of the ripple during either of the two time intervals in a switching period T_s is a linear function of time. For the interval DT_s this yields with equations (2.109)

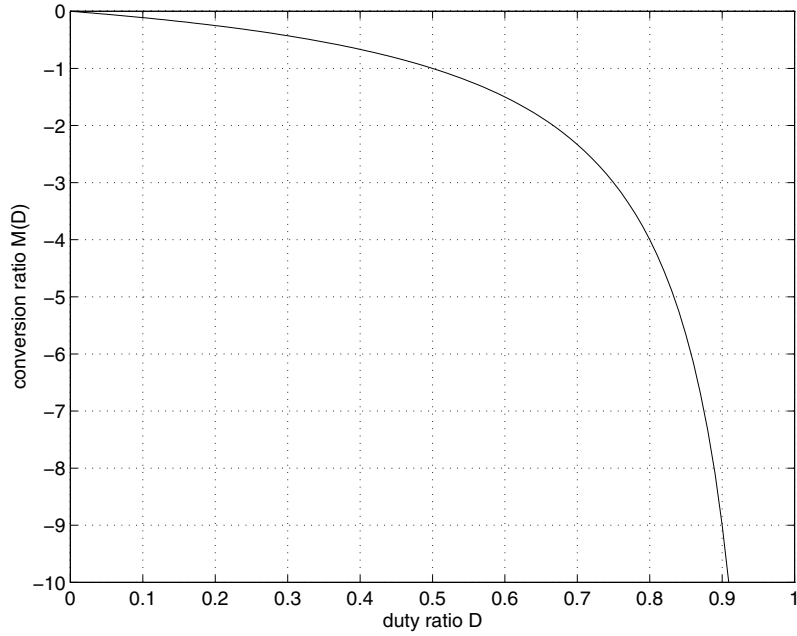


Figure 2.31: Conversion ratio $M(D)$ vs. duty ratio D for an ideal buck-boost converter.

and (2.111)

$$\begin{aligned}
 \frac{dv_{C_1}}{dt} &= \frac{i_{C_1}}{C_1} \approx \frac{I - I_l}{C_1}, \\
 \frac{dv_{C_2}}{dt} &= \frac{i_{C_2}}{C_2} \approx \frac{-I_o}{C_2}, \\
 \frac{di_l}{dt} &= \frac{v_l}{L} \approx \frac{V_i}{L},
 \end{aligned} \tag{2.118}$$

where $\frac{dv_{C_1}}{dt}$, $\frac{dv_{C_2}}{dt}$, and $\frac{di_l}{dt}$ are the slopes of the switching ripples Δv_i , Δv_o , and Δi_l , respectively. This leads to the following expressions for the peak-to-peak ripple amplitudes:

$$\begin{aligned}
 v_{i_{pp}} &= 2\Delta v_i = \frac{I - I_l}{C_1} DT_s, \\
 v_{o_{pp}} &= 2\Delta v_o = \frac{-I_o}{C_2} DT_s, \\
 i_{l_{pp}} &= 2\Delta i_l = \frac{V_i}{L} DT_s.
 \end{aligned} \tag{2.119}$$

Finally (2.119) can be transformed such that the converter components depend on specified switching ripple amplitudes Δv_i , Δv_o , and Δi_l :

$$\begin{aligned} C_1 &= \frac{I - I_l}{2\Delta v_i} DT_s, \\ C_2 &= \frac{-I_o}{2\Delta v_o} DT_s, \\ L &= \frac{V_i}{2\Delta i_l} DT_s. \end{aligned} \tag{2.120}$$

The non-ideal converter model

One important issue when designing a high efficiency switching converter is to determine the dependency of the conversion ratio on the losses occurring in the real, non-ideal components. As in the buck converter example in section 2.3.1, only the dependency on the inductor losses is analyzed. Figure 2.32 shows an equivalent circuit diagram for a boost converter with inductor losses indicated by a series resistor R_l .

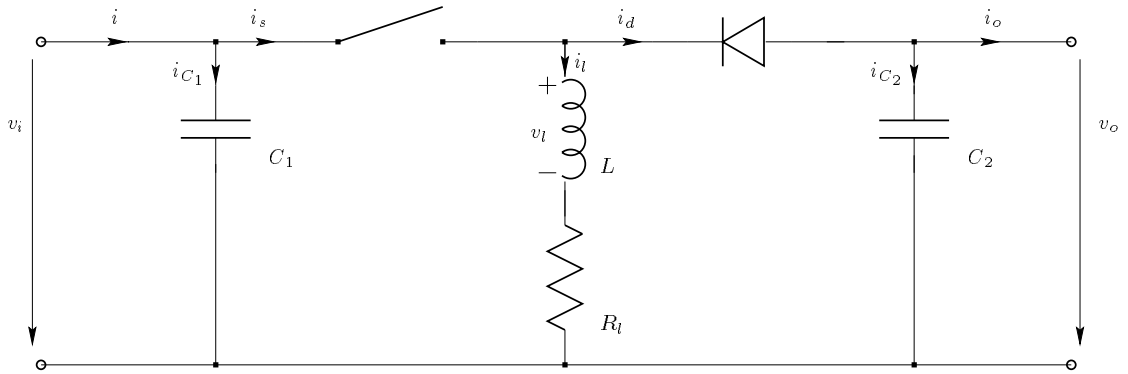


Figure 2.32: Buck-boost converter with series resistor R_l to account for inductor losses.

The inclusion of the inductor losses leads to a modified set of equations describing the converter. For the time interval DT_s these are:

$$\begin{aligned}i_{C_1} &= I - I_l, \\i_{C_2} &= -I_o, \\v_l &= V_i - R_l I_l,\end{aligned}\tag{2.121}$$

and for $D'T_s$:

$$\begin{aligned}i_{C_1} &= I, \\i_{C_2} &= -I_l - I_o, \\v_l &= V_o - R_l I_l.\end{aligned}\tag{2.122}$$

Application of the principles of inductor volt-second balance and capacitor charge balance yields the averaged steady-state model for a buck-boost converter with inductor losses considered

$$I = DI_l,\tag{2.123}$$

$$I_o = -D'I_l,\tag{2.124}$$

$$DV_i = R_l I_l - D'V_o.\tag{2.125}$$

The converter's efficiency

The previously derived equations (2.124) and (2.125) can be used to obtain the conversion ratio V_o/V_i for the non-ideal buck-boost converter as well as its efficiency

η . With (2.68)

$$\begin{aligned}
 \frac{V_o}{V_i} &= \frac{V_o}{R_l I_l - D' V_o} D \\
 &= \frac{1}{1 - \frac{R_l I_l}{D' V_o}} \left(-\frac{D}{D'} \right) \\
 &= \frac{1}{1 + \frac{R_l I_o}{D'^2 V_o}} \left(-\frac{D}{D'} \right) \\
 &= \frac{1}{1 + \frac{R_l}{D'^2 Z}} \left(-\frac{D}{D'} \right) = \eta M(D),
 \end{aligned} \tag{2.126}$$

which yields for the efficiency

$$\eta = \frac{1}{1 + \frac{R_l}{D'^2 Z}}. \tag{2.127}$$

Interestingly the expression for the efficiency of the buck-boost converter is the same as for the boost converter (equation (2.100) on page 44).

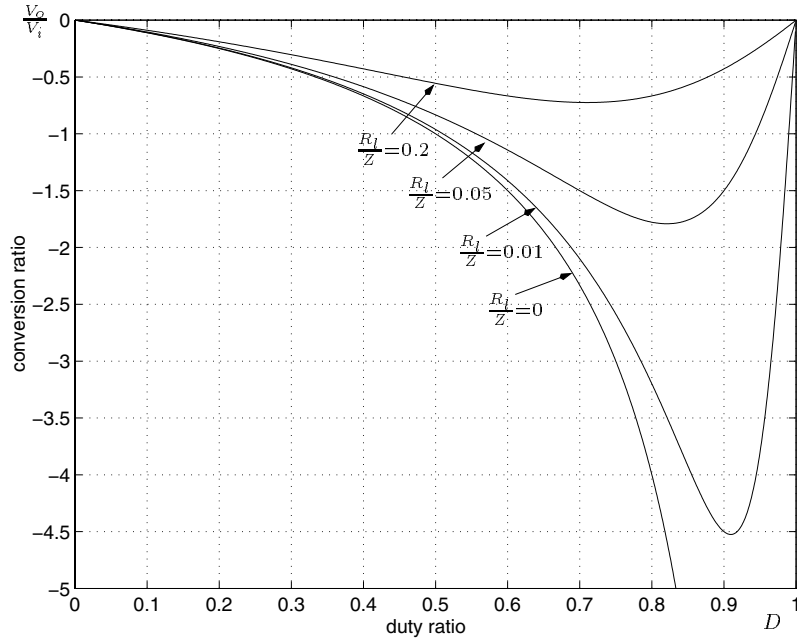


Figure 2.33: Conversion ratio V_o/V_i vs. duty ratio D for a non-ideal buck-boost converter dependent on R_l/Z .

The properties of equation (2.126) are plotted in Figure 2.33. It can be seen that the ratio R_l/Z determines the maximum possible conversion ratio V_o/V_i , with Z being the load impedance V_o/I_o .

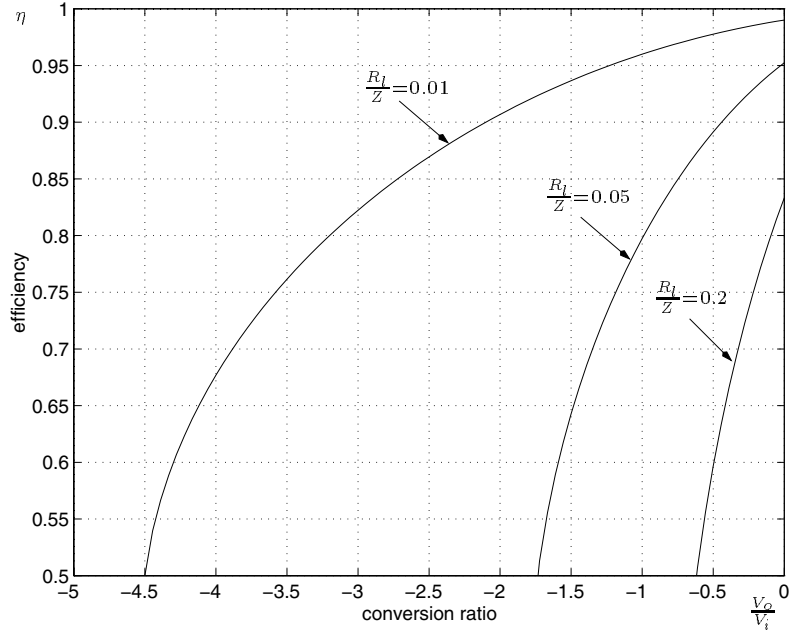


Figure 2.34: Efficiency η vs. conversion ratio V_o/V_i for a non-ideal buck-boost converter dependent on R_l/Z .

For the system design and the selection of the converter type it is important to characterize how the converter's efficiency depends on the conversion ratio. The function expressing this relation is the inverse of equation (2.126). For its derivation the inverse of (2.127) (see equation (2.101)) is substituted into (2.126):

$$\frac{V_o}{V_i} = \eta \left(\frac{D' - 1}{D'} \right) = \eta \left(1 - \sqrt{\frac{1}{R_l/Z} \cdot \frac{1 - \eta}{\eta}} \right) = \eta - \sqrt{\frac{\eta(1 - \eta)}{R_l/Z}}. \quad (2.128)$$

The inverse of (2.128) is the desired function in dependence of V_o/V_i :

$$\eta(V_o/V_i) = \frac{1}{1 + R_l/Z} \left[\frac{1}{2} + \frac{R_l}{Z} \cdot V_o/V_i \pm \sqrt{\frac{1}{4} + \frac{R_l}{Z} \cdot V_o/V_i - \frac{R_l}{Z} (V_o/V_i)^2} \right]. \quad (2.129)$$

Because the efficiency is always greater than zero, the positive root must be selected. The plot of this function (Figure 2.34) clearly shows the importance of minimizing component losses in the converter. The maximum possible conversion ratio dependent on R_l/Z is determined by the square-root term in equation (2.129):

$$\left[\frac{1}{4} + \frac{R_l}{Z} \cdot V_o/V_i - \frac{R_l}{Z} (V_o/V_i)^2 \right] \geq 0, \quad (2.130)$$

which yields for the conversion ratio:

$$\frac{V_o}{V_i} \leq \frac{1}{2} - \frac{1}{2} \sqrt{1 + \frac{1}{R_l/Z}}. \quad (2.131)$$

The negative root has been chosen in (2.131) because the conversion ratio of the buck-boost converter is always smaller than zero (see Figure 2.33).

The small-signal ac model

Similarly to sections 2.3.1 and 2.3.2, the small-signal ac model can be derived to investigate the converter's dynamic behavior. If the switching ripple is assumed to be zero, the perturbed system equations (2.113) become with (2.73):

$$\begin{aligned} C_1 \frac{d(V_i + \hat{v}_i(t))}{dt} &= I + \hat{i}(t) - (D + \hat{d}(t))(I_l + \hat{i}_l(t)), \\ C_2 \frac{d(V_o + \hat{v}_o(t))}{dt} &= -(I_o + \hat{i}_o(t)) - (D' - \hat{d}(t))(I_l + \hat{i}_l(t)), \\ L \frac{d(I_l + \hat{i}_l(t))}{dt} &= (D + \hat{d}(t))(V_i + \hat{v}_i(t)) + (D' - \hat{d}(t))(V_o + \hat{v}_o(t)). \end{aligned} \quad (2.132)$$

If equations (2.132) are multiplied out, only first order terms remain. This leads to a set of linear equations describing the small-signal behavior of the systems as

$$\begin{aligned} C_1 \frac{d\hat{v}_i(t)}{dt} &= \hat{i}(t) - D\hat{i}_l(t) - \hat{d}(t)I_l, \\ C_2 \frac{d\hat{v}_o(t)}{dt} &= -\hat{i}_o(t) - D'\hat{i}_l(t) + \hat{d}(t)I_l, \\ L \frac{d\hat{i}_l(t)}{dt} &= D\hat{v}_i(t) + \hat{d}(t)V_i + D'\hat{v}_o(t) - \hat{d}(t)V_o. \end{aligned} \quad (2.133)$$

Chapter 3

Maximum Power Point Tracking

As shown in the previous chapter, the energy extracted from a solar panel is strongly limited by the physical constraints of photovoltaic cells. The approximate power density of the insolation on a sunny day is around 1000 W/m^2 . In combination with solar cell efficiencies between 15 % and 17 % this yields a maximum possible power output between 150 W/m^2 and 170 W/m^2 .

There are two ways to increase the power coming from a photovoltaic array: One can add more panels to the array, which means an increase in area requirements and a great increase in cost for material. One can also attempt to make the existing array always work at its highest possible efficiency. Figure 2.10 on page 16 shows the Maximum Power Point (MPP) of a solar array. If the array is operated at this point with its corresponding values for current I_{mp} and voltage V_{mp} , the maximum possible efficiency is achieved.

The goal of this thesis is to find the optimum mechanism for extracting the maximum possible power out of a given set of solar panels on the solar car SOLTRAIN.

There are many different approaches to this problem. A huge variety of concepts leads to an even larger variety of circuits and mechanisms for operating photovoltaic panels as close as possible to the point of maximum power and efficiency.

Some of the concepts are very robust and simple, whereas other approaches require very sophisticated logic devices such as microprocessors combined with high-power high-efficiency switching converters.

In this chapter different approaches to operating a solar panel at or close to its maximum power point are analyzed and their suitability to the environment of a solar car is examined.

3.1 Simple panel-load matching

To achieve the goal of operating the photovoltaic cells close to their point of maximum power, the method of simple load matching can be used. In this method the optimum operating point of the solar panel is determined either in theory or under average operating conditions by a series of measurements. After the corresponding values for maximum power current and voltage (I_{mp} and V_{mp}) are found, a matching load is designed.

In the existing configuration of the car SOLTRAIN, a battery pack with an average operating voltage of 108V is used. The battery pack is configured as an energy buffer on a parallel bus with nine different solar panels (see Figure 3.1). Since the battery is electrically “stiffer” than the photovoltaic array, the system bus voltage and therefore the operating voltage of the solar cells is tied to the voltage of the batteries [SH84]. Such a system is usually designed such that the average battery voltage is close to the average V_{mp} .

The advantage of this configuration is its simplicity. Since no additional circuitry is used, the risk of component failure is kept low for the whole system and the power loss between panel and batteries is reduced to the conductor losses.

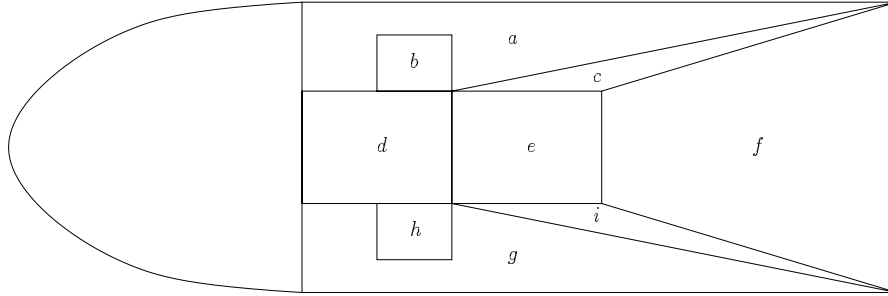


Figure 3.1: Top view of the SOLTRAIN's solar panel configuration. The corresponding panel names can be found in Table 3.1.

The drawback of this system is that it does not take any changes in insolation or temperature (and thus changes in V_{mp}) into consideration. In addition the different angles of incidence (AOI) on the individual panels are neglected. Effects like aging of the photovoltaic cell material or a dusty panel surface may also cause a variation in the point of maximum power and efficiency. Because of the parallel connection of all the different panels and the significant differences in optimum operating conditions, some panels are forced to operate far off their point of maximum efficiency. The discrepancy between the maximum power voltage V_{mp} and the nominal battery voltage V_b (108 V) was found to be higher than 50 % for some of SOLTRAIN's solar panels (see Table 3.1). This yields a significantly reduced power output, since it was shown in section 2.1.3 that a deviation of only 10 % will already lead to a power reduction of approximately 25 %.

Table 3.1 shows the values for the short circuit current I_{sc} and the open circuit voltage V_{oc} for the different solar panels on the car SOLTRAIN at two different temperatures. It is apparent that I_{sc} and V_{oc} are sensitively dependent on changes in operating conditions. The changes in the open-circuit voltage V_{oc} are mainly caused by the indicated temperature difference of approximately 25 °C (see also

panel name & location	$T \approx 50^\circ\text{C}$				$T = 25^\circ\text{C}$			
	V_{oc} (V)	I_{sc} (A)	V_{mp} (V)	$\frac{V_b - V_{mp}}{V_b}$ (%)	V_{oc} (V)	I_{sc} (A)	V_{mp} (V)	$\frac{V_b - V_{mp}}{V_b}$ (%)
[a] starboard (cells)	108.9	1.75	82.76	23.4	128.6	2.34	97.75	9.5
[b] starboard (shards)	119.1	0.26	90.25	16.2	NA	NA	NA	NA
[c] starboard wing	104.7	0.14	79.75	26.3	NA	NA	NA	NA
[d] top front	61.0	1.48	46.36	57.1	67.0	2.39	50.92	52.9
[e] top middle	114.9	1.75	87.32	19.1	135.2	2.37	102.75	4.9
[f] top back	112.4	1.72	85.42	20.9	137.8	2.32	104.73	3.0
[g] port (cells)	107.3	1.88	81.55	24.5	120.4	2.33	91.50	15.3
[h] port (shards)	109.1	0.27	82.92	23.2	NA	NA	NA	NA
[i] port wing	104.5	0.17	79.42	26.5	NA	NA	NA	NA

Table 3.1: The solar panels and the corresponding measured values for I_{sc} and V_{oc} at different temperatures for the solar car SOLTRAIN. V_{mp} denotes the theoretical maximum power voltage, whose deviation from the car’s nominal battery voltage V_b is given in %. The values at temperature $T = 25^\circ\text{C}$ were measured in a testing lab under STC, while the values at the approximate temperature $T \approx 50^\circ\text{C}$ were obtained during a field measurement on a sunny summer day in Portland, Oregon.

Figure 2.7 on page 13), whereas the changes in short-circuit current I_{sc} indicate a difference in insolation between the two measurements (see Figure 2.6 on page 13). This might be the result of variations in the AOI or a discrepancy between STC and plain Oregon sunlight. It is also noted that the values for the maximum power point I_{mp} and V_{mp} are in constant proportion to I_{sc} and V_{oc} (see Figure 2.10 on page 16). Therefore a more sophisticated method of panel-load matching must be found if higher efficiency is desired.

3.2 Semi-dynamic load matching

An improvement of the method discussed in section 3.1 is described by Yongji and Deheng [YD92]. A number of individually controllable battery cells is connected in series. Depending on the desired operating voltage of the photovoltaic

array, the number of battery cells in series can be changed.

Salameh [SMD88] implements a similar method with the use of an array reconfiguration controller. By rearranging the series and parallel connections between the different panels, the matching between load and photovoltaic cell array is improved. This enables the system to react to changes in environmental conditions such as temperature and irradiance and therefore operate closer to the actual MPP.

Both these approaches require extra circuitry and wiring. In addition, the stepwise increase or decrease in operating voltage does not permit accurate tracking of the MPP. Furthermore in Yongji's approach it is difficult to keep an equal charge level on all the battery cells which in the long term degrades battery life. As a result the flexibility necessary for the use with a solar powered vehicle can not be achieved. These methods might be sufficient for use with a stationary photovoltaic system to provide two or more operating modes for different times of the day or different seasons.

3.3 The voltage-feedback method

If no battery is present in the system to tie the bus voltage to an almost constant level, a simple control system can be applied [SP93, HS98]. As discussed in Chapter 2, a dc-to-dc converter can be used to convert the voltage level at a photovoltaic cell array to another voltage level at the load. Feedback of the panel voltage and comparison with a constant reference voltage can be used to continuously adjust the duty ratio of the converter to operate the solar panel at a predefined operating point close to the MPP.

This method makes it possible to operate a solar array under unknown or

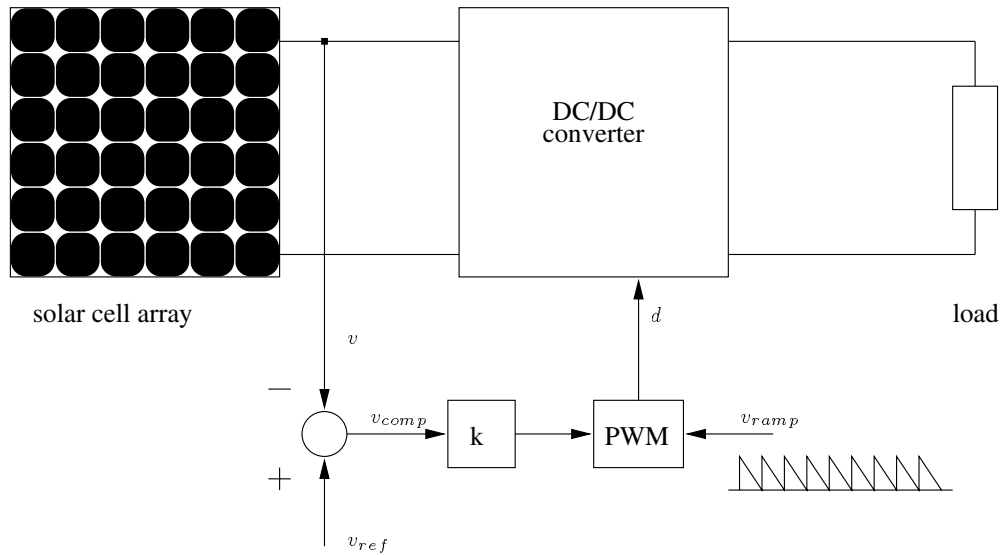


Figure 3.2: Voltage-feedback with pulse width modulation (PWM) on a dc-dc converter.

changing load conditions and still be able to choose a desirable operating point for the panel.

The disadvantages of this configuration are the same as for the method of simple load matching with a battery pack as discussed in section 3.1. The system is not able to adjust to changing environmental conditions such as insolation and temperature. It is therefore not suitable for use in a solar powered vehicle.

As already mentioned above, the panel voltage at the maximum power point V_{mp} can be considered to be a constant fraction of the panel's open-circuit voltage V_{oc} . This relation can be used to get information about the current position of the panel's MPP and is employed in the approach discussed next.

3.3.1 Measurement of V_{oc} at the panel

An improved version of the voltage-feedback method is used by Enslin and others [EWSS97]. The panel's open-circuit voltage V_{oc} is measured by interrupting the normal operation of the system with a certain frequency, storing the measured value, and then adjusting the reference voltage v_{ref} to some fraction of the open-circuit voltage which has been experimentally determined to be 76 % of V_{oc} . This reference voltage is compared with the operating voltage of the panel V and the resulting error signal v_{comp} is used as input to the PWM control of the dc-dc converter (see also Figure 3.2).

This augmentation allows the control of the operating voltage of the photovoltaic panel with consideration of such important factors as irradiance and temperature. In addition aging and dust accumulation on the cell surface are taken into account.

Since the adjustment of the reference voltage to 76 % of the open-circuit voltage is always a fixed fraction, this method can still not be called real maximum power point tracking. The accuracy of the adjustment of the operating voltage to the maximum power voltage V_{mp} depends on the choice of this fraction compared to the real ratio of V_{mp} to V_{oc} .

The interruption of the regular system operation with a certain frequency yields losses which are estimated by Sullivan and Powers [SP93] to be 0.05 % of the available maximum power. Losses caused by the inaccuracy in finding the actual MPP are estimated to be around 0.5 % (although these figures may be optimistic). Frequent system interruption will furthermore lead to an increase in electrical noise. The system components in the converter and the control circuit must be designed to be able to cope with the resulting current interruptions.

3.3.2 Usage of a pilot cell

To avoid the drawbacks related with a frequent interruption of the system operation, Schaefer and Hise [SH84] as well as Salameh, Dagher, and Lynch [SDL91] propose the use of a pilot cell. This is a single photovoltaic cell which is electrically independent of the rest of the array. Its open circuit voltage V_{oc} is constantly measured and therefore gives implicit information of the rest of the panel's current operating conditions. As with the method discussed in section 3.3.1, V_{oc} of the pilot cell is multiplied by a certain constant factor to result in the reference voltage for the feedback control loop.

This method avoids the problems caused by the interrupted operation of the photovoltaic array, but still allows adjustment of the feedback control reference voltage dependent on changes in such important factors as irradiance and temperature.

In a solar powered vehicle the use of a pilot cell as a reference for the behavior of the array is not easy to implement. Surface area, already very limited, must be reserved for the placement of the cell, which will not contribute to the power generation itself.

In the special case of the solar car SOLTRAIN it would be impossible to find an ideal placement of a pilot cell to represent all the cells on the vehicle (see Table 3.1). Since the different solar panels are mounted at different angles, it would be necessary to place an individual pilot cell for each of them.

Since this method still uses a fixed factor to estimate the optimum operating point voltage V_{mp} from a measured value of V_{oc} , the MPP is still not truly tracked. This technique relies on previous knowledge of the photovoltaic array's characteristics to estimate where the maximum power point is. The losses caused by not

operating at the exact MPP are of the same order of magnitude as estimated by Sullivan and Powers [SP93] for the method described in section 3.3.1.

3.4 The power-feedback method

The overall goal is to increase the power output of the vehicles solar array. In some papers it is proposed to maximize the power delivered to the load [SMD88, HS98, SP93, HLS98]. But as Sullivan and Powers [SP93] point out, the maximization of the power to a motor as a load may lead to a maximization of the power dissipated in its windings and not to a maximization of its mechanical power output. To have a design which is independent of the load type, it is therefore preferable to pursue a maximization of solar panel output power.

If actual MPP tracking is to be achieved, it is necessary to get information about the actual power extracted from the photovoltaic array. This can be done by measuring the panel output voltage V and the panel output current I and then multiplying these two parameters to get the actual value for the panel output power $P = VI$. Given these values there are various methods of tracking the actual MPP of the array.

3.4.1 The perturbation and observation method (P&O)

The P&O method is a widely used approach to MPPT. It employs a microprocessor with the values for panel voltage V and panel current I as its input values and the desired operating voltage V_{ref} as its output value. The notation used for the desired operating voltage V_{ref} alludes to the fact that this system can then be inserted in the already discussed voltage-feedback controller to supply v_{ref} as

shown in Figure 3.2.

Another possible configuration is to have the microprocessor directly controlling the dc-to-dc converter's PWM input variable d . This makes the extra voltage control feedback loop dispensable.

As the name of the P&O method states, this process works by perturbing the system by increasing or decreasing the array operating voltage and observing its impact on the array output power. Figure 3.3 shows a flow chart diagram of the P&O algorithm as it is implemented in the controlling microprocessor.

As can be seen in Figure 3.3, V and I are measured to calculate the current array output power $P(k)$. This value for $P(k)$ is compared to the value obtained from the last measurement $P(k - 1)$. If the output power has increased since the last measurement, the perturbation of the output voltage will continue in the same direction as in the last cycle. If the output power has decreased since the last measurement, the perturbation of the output voltage will be reversed to the opposite direction of the last cycle.

With this algorithm the operating voltage V is perturbed with every MPPT cycle. As soon as the MPP is reached, V will oscillate around the ideal operating voltage V_{mp} . This causes a power loss which depends on the step width of a single perturbation. If the step width is large, the MPPT algorithm will be responding quickly to sudden changes in operating conditions with the tradeoff of increased losses under stable or slowly changing conditions. If the step width is very small the losses under stable or slowly changing conditions will be reduced, but the system will be only able to respond very slowly to rapid changes in temperature or insolation. The value for the ideal step width is system dependent and needs to be determined experimentally.

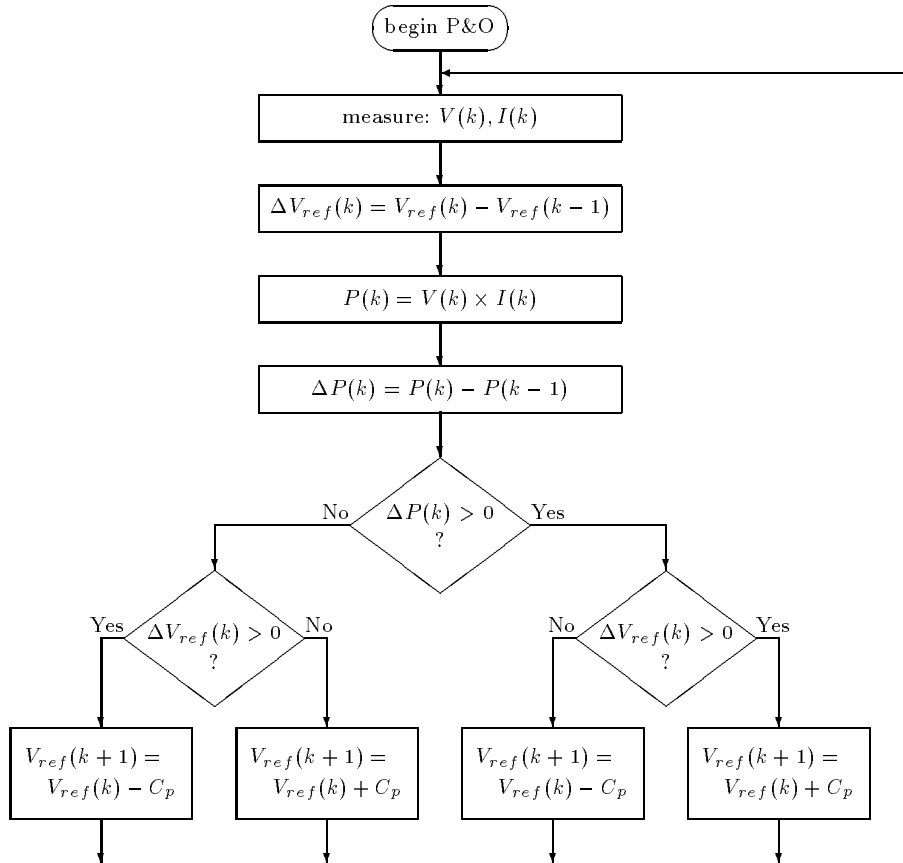


Figure 3.3: Flow chart of the P&O MPPT algorithm. C_p is the perturbation step width.

Another drawback of the P&O method is described by Hussein and others [HMHO95]. In the case of a sudden increase in insolation S , the P&O algorithm reacts as if the increase occurred as a result of the previous perturbation of the array operating voltage. The next perturbation, therefore, will be in the same direction as the previous one. Assuming that the system has been oscillating around the MPP, it can be seen in Figure 3.4 that a continuous perturbation in one direction will lead to an operating point far away from the actual MPP. This process continues until the increase in insolation slows down or ends.

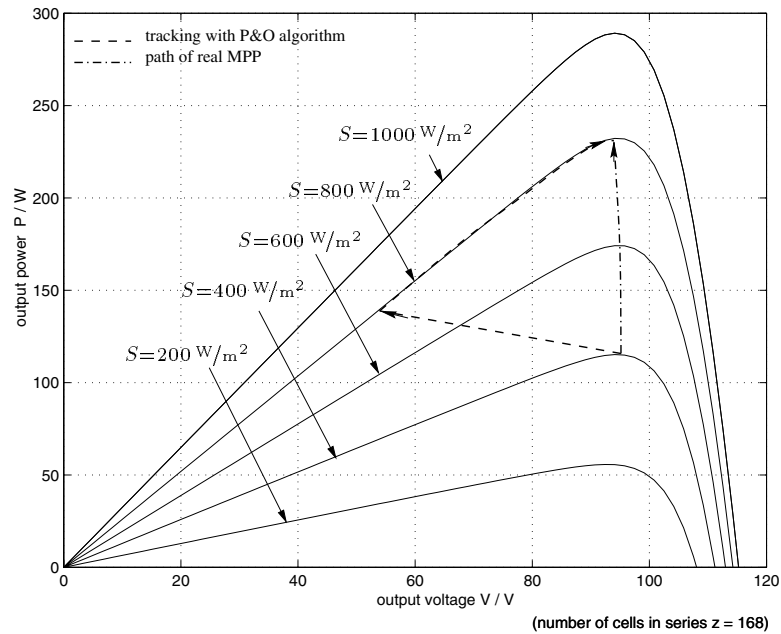


Figure 3.4: Deviation from the MPP with the P&O algorithm under rapidly changing insolation levels S .

In an environment of rapidly changing atmospheric conditions and frequently changing insolation levels this deviation from the MPP can cause significant power loss. A moving vehicle represents such an environment. The rapid changes of the insolation levels S on a photovoltaic array mounted on a vehicle are not only

caused by clouds and passing shadows of buildings or vegetation, but also by the ever changing AOI on the array as the car moves around curves and corners.

Experimental results by Hussein and others [HMHO95] show an efficiency of 81.5% when using the P&O algorithm. This however, is still a vast improvement compared to the 31.3% efficiency shown by a system operating without any MPPT mechanism.

The improved P&O algorithm

Burger [Bur97] proposes a solution to the problem of deviation from the MPP during rapidly increasing insolation levels. He introduces a new condition to the ‘Yes’ branch of the $\Delta P(k) > 0$ condition in the P&O algorithm (Figure 3.3). If the output power has increased twice during the last two cycles or if the direction of perturbation has been the same for the last two steps, the direction of the perturbation of the output voltage is reversed. Table 3.2 shows the truth table for this improved algorithm with all of the 16 possible states of the MPPT and the resulting choice of the next $\Delta V_{ref}(k+1)$.

Table 3.2 shows two cases of unclear conditions. These occur when the output power has increased twice over two consecutive steps in the same direction of perturbation. In this case it could be that the system is deviating from the MPP as indicated in Figure 3.4. Therefore the new control condition cc as proposed by Burger has been included in the P&O algorithm. If the output power increase is caused by the perturbation of the output voltage and not by an increase in insolation, the value for $P(k)$ will decrease with this proposed control step in the opposite direction. If the output power increase is caused by an increase in insolation, the power will still be increasing even with this reversal of the perturba-

signum ΔV_{ref} ($k-1$)	signum ΔP ($k-1$)	signum ΔV_{ref} (k)	signum ΔP (k)	status	signum ΔV_{ref} ($k+1$)
-	-	-	-	invalid	+
-	-	-	+	invalid, <i>cc</i> true	+
-	-	+	-	<i>S</i> decr.	-
-	-	+	+	$V < V_{mp}$	+
-	+	-	-	$V \approx V_{mp}$	+
-	+	-	+	unclear, <i>cc</i> true	+
-	+	+	-	$V > V_{mp}$	-
-	+	+	+	<i>S</i> incr., <i>cc</i> true	-
+	-	-	-	<i>S</i> decr.	+
+	-	-	+	$V > V_{mp}$	-
+	-	+	-	invalid	-
+	-	+	+	invalid, <i>cc</i> true	-
+	+	-	-	$V < V_{mp}$	+
+	+	-	+	<i>S</i> incr., <i>cc</i> true	+
+	+	+	-	$V \approx V_{mp}$	-
+	+	+	+	unclear, <i>cc</i> true	-

Table 3.2: Truth table for the improved P&O algorithm with MPP deviation control condition “*cc*”. *S* is the insolation level.

tion. Therefore the system will be oscillating around its previous operating point until the increase in insolation ends. The exact behavior of the system with this improved P&O algorithm will be discussed along with the performed SIMULINK® simulations in Chapter 4.

3.4.2 The incremental conductance method (IncCond)

To avoid the drawbacks of the P&O MPPT method, Hussein and others [HMHO95] developed the incremental conductance MPPT algorithm (IncCond). It is based on the fact that the derivative of the output power P with respect to the panel voltage V is equal to zero at the maximum power point (MPP). The solar panel's P - V characteristics in Figure 3.4 show further that the derivative is greater than zero to the left of the MPP and less than zero to the right of the MPP. This leads to the following set of equations:

$$\frac{dP}{dV} = 0 \quad \text{for } V = V_{mp}, \quad (3.1)$$

$$\frac{dP}{dV} > 0 \quad \text{for } V < V_{mp}, \quad (3.2)$$

$$\frac{dP}{dV} < 0 \quad \text{for } V > V_{mp}. \quad (3.3)$$

The fact that $P = VI$ and the chain rule for the derivative of products yields

$$\frac{dP}{dV} = \frac{d(VI)}{dV} = I \frac{dV}{dV} + V \frac{dI}{dV} = I + V \frac{dI}{dV}. \quad (3.4)$$

Combining equations (3.1) and (3.4) leads to the MPP condition ($V = V_{mp}$) in terms of array voltage V and array current I :

$$\frac{dI}{dV} = -\frac{I}{V}. \quad (3.5)$$

This shows that with equations (3.1)–(3.4) enough information is gathered to determine the relative location of the MPP by measuring only the incremental and

instantaneous array conductances $\frac{dI}{dV}$ and $\frac{I}{V}$, respectively. Hussein and others used these relations to develop the IncCond algorithm as shown in Figure 3.5.

The algorithm is implemented with a microprocessor controlling either the dc-to-dc converter input d directly or by setting the reference voltage v_{ref} for a voltage-feedback controller circuit as shown in Figure 3.2.

As can be seen in Figure 3.5, the IncCond MPPT method works with just two sensors measuring the panel's operating voltage V and current I . The necessary incremental changes dV and dI are approximated by comparing the most recent measured values for V and I with those measured in the previous cycle:

$$dV(k) \approx V(k) - V(k - 1), \quad (3.6)$$

$$dI(k) \approx I(k) - I(k - 1). \quad (3.7)$$

The central function to find the MPP employs the conditions

$$\frac{dI}{dV} = -\frac{I}{V}, \quad (3.8)$$

and

$$\frac{dI}{dV} > -\frac{I}{V}. \quad (3.9)$$

If (3.8) is true, the system operates at the MPP and no change in operating voltage is necessary — thus the adjustment step is bypassed and the current cycle ends.

If (3.8) is false, equation (3.9) with (3.2) and (3.3) is used to determine whether the system is operating at a voltage greater or less than V_{mp} . The operating voltage is adjusted accordingly.

If the system was operating at the MPP during the previous cycle, the incremental change of the operating voltage will be zero ($dV(k) = 0$). This would lead

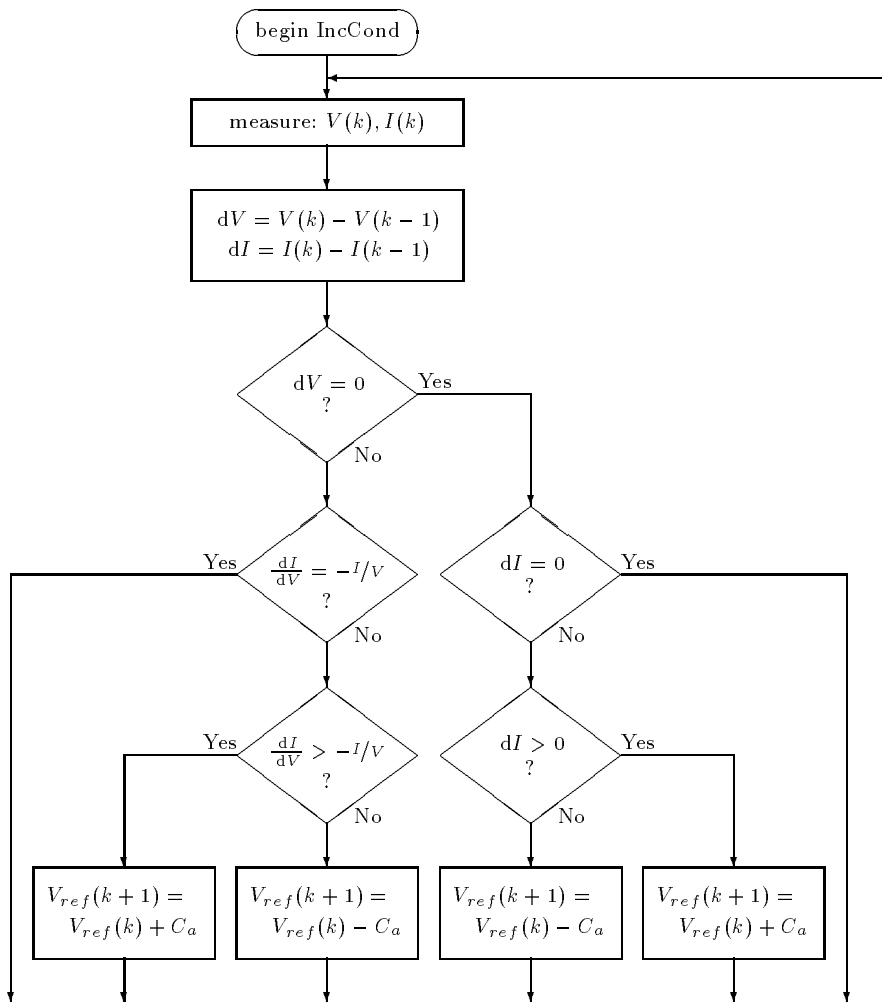


Figure 3.5: Flow chart of the IncCond MPPT algorithm. C_a is the adjustment step width.

to a division by zero error. To avoid a system crash, this condition is checked first and leads if true to another branch in the algorithm with further tests on possible changes of the panel's operating conditions. Since the voltage has not changed, the only useful information about possible changes can be gained from the current measurement and its possible incremental change dI . If dI is equal to zero, the operating conditions have not changed and therefore the adjustment of the system voltage is bypassed. If $dI \neq 0$, equations (3.2) and (3.3) are used to determine if the system is operating above or below V_{mp} and a corresponding adjustment of the operating voltage is performed.

One of the advantages of this MPPT algorithm is that it does not oscillate around the MPP. The check of conditions (3.8) and $dI = 0$ allows it to bypass the perturbation step and therefore maintain a constant operating voltage V once the MPP is found.

Furthermore, conditions (3.9) and $dI > 0$ make it possible to determine the relative location of the MPP. This leads to the advantage that an initial adjustment in the wrong direction, as with the "trial and error" P&O method, does not occur. A fast and correct system response to changing operating conditions should be the result — yielding a high system efficiency.

According to Hussein, the mentioned problem of deviation from the MPP under fast increasing insolation levels in a P&O controlled system is overcome with the IncCond method. This claim will be tested by a complete system simulation discussed in Chapter 4.

Hussein and others' experimental results showed for the IncCond method an efficiency in relation to theoretical maximum power of 89.9%. The same experimental configuration with the P&O MPPT algorithm resulted in only 81.5%

efficiency (see section 3.4.1).

Hussein and others also discovered with their experiments that the maximum power condition $\frac{dP}{dV} = 0$ (which is equivalent to $\frac{dI}{dV} = -\frac{I}{V}$) only rarely occurred. This results in oscillations around the MPP even under stable environmental conditions. This instability is mainly caused by the approximations made for dV and dI with equations (3.6) and (3.7). It is also very difficult to adjust V to the exact V_{mp} when using a constant adjustment step width C_a .

A solution to this problem would be to add a small marginal error ϵ to the maximum power condition (3.5) such that the MPP is assumed to be found if

$$\left| \frac{dI}{dV} + \frac{I}{V} \right| \leq \epsilon. \quad (3.10)$$

The value of ϵ must be determined with consideration of the tradeoff between the problem of not operating exactly at the MPP and the possibility of oscillating around it. It will also depend on the chosen perturbation step width C_a .

Further detailed investigations of the IncCond MPPT method will be discussed in Chapter 4 with the support of performed SIMULINK® simulations.

3.4.3 Analog MPPT methods

The two previously discussed methods both utilize microprocessors to track the MPP. The values for the solar array's output voltage V and output current I are digitized and then analyzed by an algorithm to decide on an appropriate control step.

Analog systems use the voltage and the current from the photovoltaic cells directly to control the operating point of the panel. The current is sensed by a small resistance in the current path. The resulting voltage drop v_{sense} is proportional to

the current's value.

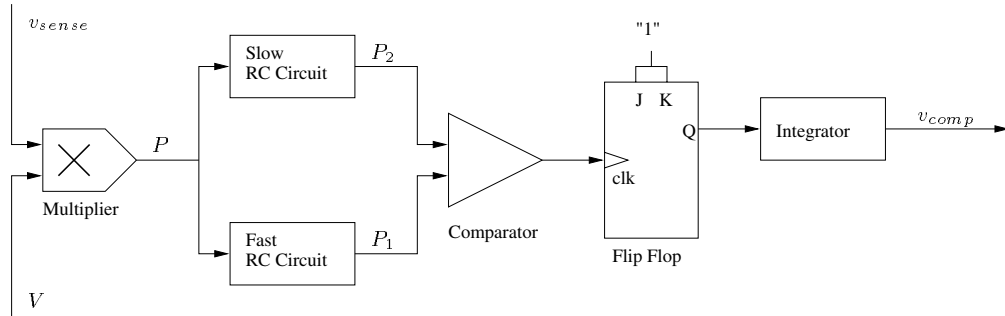


Figure 3.6: Analog MPPT mechanism

Salameh and Taylor [ST90] propose the system shown in Figure 3.6. The voltage v_{sense} which is proportional to the panel current I is multiplied with the panel voltage V . The multiplier outputs a signal proportional to the present panel output power P . The two different RC circuits force differing time delays upon the signal P in the two branches to form P_1 and P_2 . These two signals generate an output signal at the comparator representing the sign of the derivative $\frac{dP}{dt}$. For increasing power output at the panel this slope is greater than zero, for decreasing power it is less than zero. The comparator's output is then used to trigger a flip-flop which toggles its output value between the two states -1 and 1 every time a falling edge occurs on its input. The flip-flop's output is integrated and used as a slowly increasing or decreasing v_{comp} to form the PWM control signal of the dc-to-dc converter as shown in Figure 3.2 on page 63.

This analog approach to MPPT is similar to the simple P&O MPPT method discussed in section 3.4.1. The output voltage of the panel is perturbed by changing the conversion ratio d of the dc-to-dc converter. To decide on the direction of perturbation a feedback loop is created. The value of $\frac{dP}{dt}$ is used to determine

whether the output power of the panel increases or decreases. If the output power is increasing, the perturbation continues in one direction until a decrease is detected. The perturbation is then reversed and continues in the opposite direction until the sign of $\frac{dP}{dt}$ changes again from positive to negative.

On the P - V curve shown in Figure 2.10 this is equivalent to the operating point of the panel climbing up towards the MPP. As it overshoots the ideal operating voltage V_{mp} the MPP is passed and the power starts to decrease. This causes the derivative $\frac{dP}{dt}$ to become negative and triggers the flip-flop to change its output state. Now the direction of perturbation is reversed and the operating point climbs towards the MPP again. A constant oscillation around the MPP is the result.

This similarity to the P&O method comes along with almost the same drawbacks: in the case of rapidly increasing insolation levels, the tracking mechanism is unable to detect if the power increase is caused by its perturbation of the operating point or by the increase of irradiance at the photovoltaic cells. This can cause a deviation from the MPP as shown in Figure 3.4 which results in unwanted power losses. Furthermore, the continuous perturbation of the operating point causes an oscillation around the MPP even under constant operating conditions. These oscillations further reduce the efficiency of this MPPT mechanism.

One of the main disadvantages of this analog MPPT technique is mentioned by Sullivan and Powers [SP93]: rapid changes in insolation or a noisy current sense signal can cause the flip-flop to change its state incorrectly. The system is unable to recover from this error. The false flip-flop state will force the operating point to ramp away from the MPP, resulting in a constant negative input signal at the flip-flop. Since the flip-flop changes its state only if a falling edge occurs on its input, the operating point will continue to drift in the wrong direction until the

system shuts down.

To prevent the system from being shut down with this arbitrarily occurring error, a fault condition must be defined. Sullivan and Powers suggest monitoring the panel output current and forcing the flip-flop to change its state as soon as the current falls below a pre-determined limit. The drawback of this solution is the limitation of the operating range of the panel to current values above this limit. Furthermore, the operating point must drift quite far away from the MPP for the faulty state to be detected. This will create a significant source of power loss if the error occurs frequently.

3.4.4 Forced oscillation — auto oscillation

In all of the MPPT methods discussed so far, the derivative of the solar panel's output power was used in various ways to determine the relative location of the MPP. Appropriate adjustment of the operating voltage eventually led to an operating point closely oscillating around the MPP. These oscillations were automatically generated by the utilized feedback control.

A new method with a forced oscillation of the operating point is introduced by Cocconi and Rippel in the GM Sunracer Case History [CR90]. A small 100 Hz voltage ripple is added to the panel's operating voltage. This results in an output power ripple whose phase and amplitude are dependent on the operating point's location relative to the MPP.

Figure 3.7 shows how a modulation of the array voltage causes a ripple in the output power. If this modulation occurs in the area below the MPP (denoted A), the voltage and the power ripple will be perfectly in phase. If the modulation occurs at an operating point in the area above the MPP (denoted B), the output

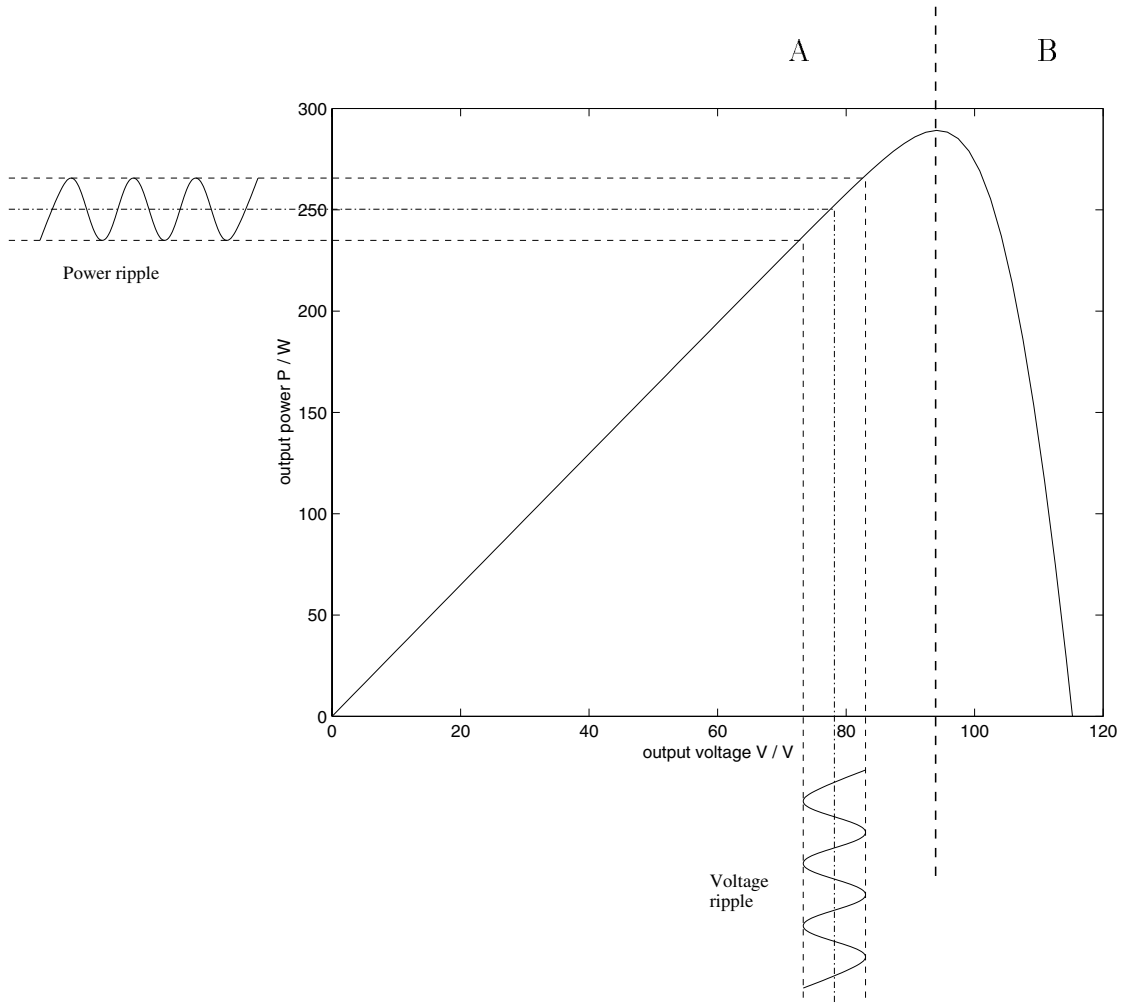


Figure 3.7: P - V curve for the solar array with the power ripple caused by the array voltage modulation. The letter A denotes the area for an operating point below the MPP, B the area above the MPP.

power ripple will be 180 degrees out of phase. In the special case that the operating point is exactly at the MPP, the power ripple will have twice the frequency of the voltage ripple and be very low in amplitude.

Cocconi and Rippel then feed the ac component of the output power signal into a “synchronous detector” which is clocked by the supplied voltage ripple. This detector analyzes the signal’s phase and magnitude and outputs an error signal proportional to the operating point’s distance to the MPP. The error signal is integrated and fed back into the dc-to-dc converter’s PWM control.

The advantage of this method is that the phase and amplitude analysis provides information about the location of the MPP. Furthermore, the integrated output signal of the synchronous detector slowly converges towards zero as the operating point approaches the MPP. This allows for the operating voltage V to be slowly adjusted towards V_{mp} . There will be no continuous oscillation around the MPP caused by a fixed step width of the MPPT. The only oscillation occurring with this method is the 100 Hz modulation of the operating voltage.

The drawback of this method is the difficulty in evaluating very low signal amplitudes. The ac component of the output power signal is much smaller than the dc component and will contain a high noise level due to the switching dc-to-dc converter. This noise can be filtered out using higher order bandpass filters, but this will lead to further losses in the signal’s amplitude. When the operating point finally approaches the MPP, the signal’s amplitude will further decrease and will make it difficult for the synchronous detector to maintain a stable output signal. An increase in the amplitude of the modulating signal to improve the signal to noise ratio will also lead to higher oscillations at the MPP and therefore increase power losses even under stable environmental conditions [Bur97].

3.5 The current-feedback method

In all of the real MPPT methods presented so far, a measurement of I and V was used to get information about the present panel output power. Based on this information the MPPT mechanism adjusted the panel output voltage V to move the operating point of the solar cells closer to their MPP.

Sullivan and Powers [SP93] as well as Burger [Bur97] present a new method of MPPT using only a current measurement to get information on the system's present operating point.

Their method is based on the assumption that the system's battery pack always operates at a nearly constant voltage level. Therefore a maximization of the power fed into the battery would be equal to maximizing the battery charge current I_b . This means that instead of finding and minimizing $\frac{dP}{dV}$, this technique seeks to control and minimize the derivative $\frac{dI_b}{dV}$. The information gained from the current measurement is interpreted in the same manner as the power signal has been used in the previous tracking methods. This means that either the analog MPPT methods as proposed by Sullivan and Powers or microprocessor based methods as proposed by Burger with the standard MPPT algorithms (see sections 3.4.1 and 3.4.2) are applicable.

The advantage of this method is that it does not require the complexity, cost and power necessary to sense and multiply two different operating parameters.

Since the maximized battery input current I_b equals the dc-to-dc converter's output current, this approach has the same restrictions as techniques maximizing the dc-to-dc converter output power: it is dependent on a battery as a load. The risk of maximizing the power dissipation in the windings of a dc-motor load has

already been mentioned at the beginning of section 3.4. But there are further problems occurring without a battery buffer tying the voltage to an almost constant level: maximizing power is only equivalent to maximizing current if a rise in current is *always* associated with a rise in power. In mathematical terms this means that the derivative $\frac{dP_b}{dI_b}$ must be bounded and strictly greater than zero. This can be expressed as:

$$0 < \frac{V_b}{I_b} + \frac{dV_b}{dI_b} < \infty. \quad (3.11)$$

This will always be the case for a plain resistive load or a battery load. But if the load consists of another PWM dc-to-dc converter for example controlling a dc-motor (as with the SOLTRAIN), the derivative $\frac{dP_b}{dI_b}$ would be ideally equal to zero which would result in the impossibility of finding the MPP in the measured current signal.

Chapter 4

Simulation and Evaluation

Simulations are a powerful tool for evaluating the theoretical performance of different systems. The device under test can be operated under easily controllable conditions and its performance can be precisely monitored. The process of simulation links the two major parts of a system design: the theoretical outline and the realization of a prototype. Finally, since changes in the design can be made easily in a simulated system, it is possible to experiment with a wide set of variations in order to find the optimum solution.

Since digital MPPT methods provide better control than analog techniques and are essentially independent of environmental influences on performance, they are best suited for operation in the rough conditions of an outdoor vehicle. The challenging aspect of the design of a digital controller for MPPT applications is the inclusion of a discrete-time device into a continuous-time environment. This makes it impossible to obtain a closed-form transfer-function for conventional analysis of the system's stability and dynamic performance.

The MathWorks' software package MATLAB[®] includes the simulation tool SIMULINK[®]. It provides the possibility to simulate “mixed continuous and discrete systems” [TMW98]. This makes it well suited to implement, test, and evaluate

digital MPPT systems introduced in Chapter 3.

SIMULINK® allows for the division of a simulated system into a number of subsystems. These subsystems can be modeled and tested individually and then interconnected later. This makes it possible to build the physical subsystems such as the solar panel, the batteries, the dc-to-dc converter, and the MPPT as independent units and verify their proper functionality. Finally these subsystems can be combined to form a complete MPPT-controlled photovoltaic power system as shown in Figure 4.1. MPPT techniques and converter types can be combined and their operation can be simulated on solar panels and a battery pack of any desired size under an unlimited variety of operating conditions.

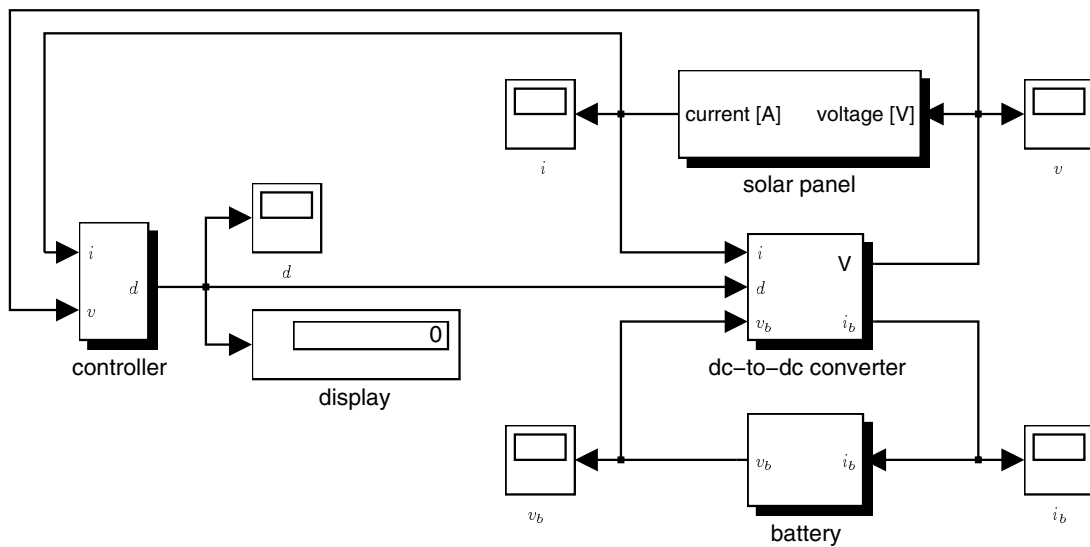


Figure 4.1: Block diagram of the MPPT-controlled solar power system.

Oscilloscope and discrete-value display blocks can be attached to any interconnecting line to monitor the corresponding signal's behavior. The monitored signal can also be written to a workspace variable for further evaluation and analysis

using MATLAB[®].

The next section will clarify how the various subsystem blocks for this study were modeled and on which mathematical equations they are based.

4.1 Modeling of the system components

The MPPT-controlled photovoltaic power system is simulated as a combination of subsystems as shown in Figure 4.1. Individual subsystem blocks represent the actual physical parts of the power supply system. Their models are based on the characteristic equations derived in Chapter 2.

4.1.1 The solar panel

The mathematical model for a photovoltaic cell array was derived in section 2.1.3 and is given by equation (2.9) as

$$I = I_{ph} - I_{s_1} \left[e^{\frac{q(V+IzR_s)}{zn_1kT}} - 1 \right] - I_{s_2} \left[e^{\frac{q(V+IzR_s)}{zn_2kT}} - 1 \right] - \frac{V + IzR_s}{zR_p}.$$

Further expressions (equations (2.4), (2.5), and (2.6)) were given to substitute for I_{ph} , I_{s_1} , and I_{s_2} respectively and are repeated here for convenience:

$$\begin{aligned} I_{ph}(T) &= I_{ph}|_{(T=298\text{K})} [1 + (T - 298\text{K}) \cdot (5 \cdot 10^{-4})], \\ I_{s_1} &= K_1 T^3 e^{-\frac{E_g}{kT}}, \\ I_{s_2} &= K_2 T^{\frac{5}{2}} e^{-\frac{E_g}{kT}}. \end{aligned}$$

To build an equivalent SIMULINK[®] simulation model of the solar panel, the above substitutions were used to further subdivide the panel into blocks representing the various elements of its equivalent circuit model (introduced in Fig-

ure 2.5). For example, the current through the parallel resistance (which is given as $I_{R_p} = \frac{V+IzR_s}{zR_p}$) is realized as presented in Figure 4.2.

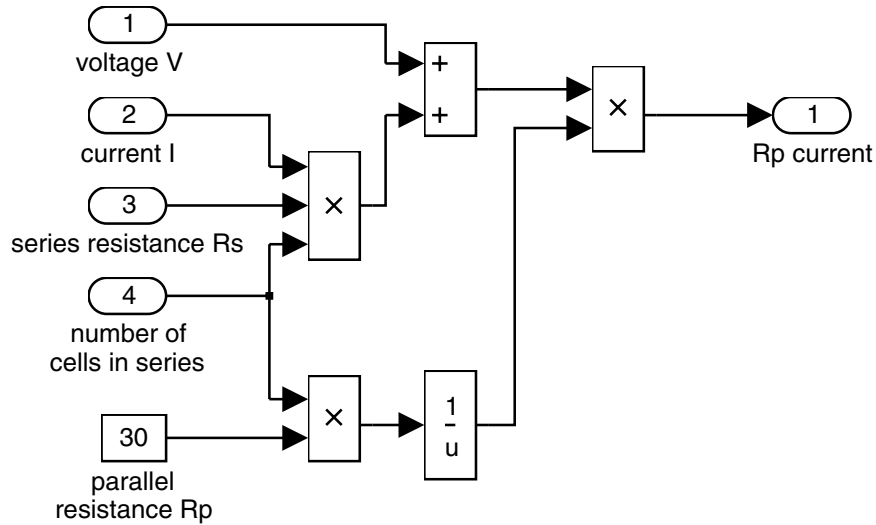


Figure 4.2: SIMULINK[®] implementation of the expression $I_{R_p} = \frac{V+IzR_s}{zR_p}$.

Separate blocks are created for the two diode currents I_{d_1} and I_{d_2} , and the generated photo-current I_{ph} . The interconnection of these individual subsystems yields the final simulation model of the solar panel. The resulting block diagram is shown in Figure 4.3.

The values for cell temperature T , insolation S , and number of photovoltaic cells in series z are accessible as external variables and can be changed anytime during the simulation process. This makes it possible to observe and evaluate the system's reaction to sudden changes in the operating conditions, such as variations in irradiance caused by passing sources of shade.

All further component dimensions are obtained from manufacturer's specifications [Bur97] for a photovoltaic cell type similar to that used in the solar racing

car SOLTRAIN. The actual values are noted in Appendix A.

4.1.2 The batteries

In section 2.2 an equivalent circuit model for a lead-acid battery was introduced (Figure 2.13). A mathematical description was given and transferred into a single-term form in the frequency domain (equation (2.17)) denoted as the battery impedance:

$$Z(s) = \frac{s^2 a_2 + s a_1 + a_0}{s^2 b_2 + s b_1 + b_0},$$

where the coefficients a_i and b_j were given as expressions (2.18).

For the simulations this equation was represented as a single transfer-function block, which accepts the coefficients of the given polynomials directly (see Figure 4.4). The battery's equivalent capacitance C_{bp} was determined using equation (2.14) and data from the manufacturer's specification of the SOLTRAIN battery pack¹. The remaining component values were modeled to realize an approximate overvoltage of 27 V at the maximum charging current of 9.5 A — based on experimental data acquired by Lu, Liu, and Wu [LLW95] and by Casacca and Salameh [CS92]. The exact values used for the simulations are given in Appendix A.

4.1.3 The dc-to-dc converter

Various mathematical models of the three converter types (buck, boost, and buck-boost) were derived in Chapter 2. For the simulations a model is neces-

¹The SOLTRAIN battery pack consists of a series connection of 9 independent 12 V GNB batteries with a specified capacity of 45 Ah each. This adds up to an theoretical operating voltage of 108 V. The actual operating range (V_{min}, V_{max}) of the batteries lies between 90 V and 125 V.

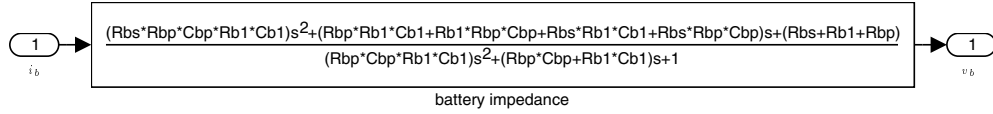


Figure 4.4: Battery impedance represented as a single SIMULINK[®] transfer-function block.

sary which describes the converter's steady-state behavior as well as its dynamic performance.

The buck converter

The basic equations for the buck converter were given in section 2.3.1 as expressions (2.20)–(2.22) for the time period DT_s and (2.23)–(2.25) for $D'T_s$. They can be used to obtain an averaged system description when employing equation (2.87):

$$\begin{aligned}\frac{dv}{dt} &= \frac{1}{C_1} [i - di_l], \\ \frac{dv_b}{dt} &= \frac{1}{C_2} [i_l - i_b], \\ \frac{di_l}{dt} &= \frac{1}{L} [dv - v_b].\end{aligned}\tag{4.1}$$

When the derivative $\frac{d}{dt}$ of a variable is equal to zero (i. e., in the steady-state case), these equations are equivalent to the steady-state dc model derived in section 2.3.1 as expressions (2.48)–(2.50). If $\frac{d}{dt} \neq 0$, equations (4.1) represent the desired system dynamics. They must be brought into a form which is suited to interconnect their representing system blocks with the rest of the simulated power system:

$$i_b = i_l - C_2 \frac{dv_b}{dt},\tag{4.2}$$

$$i_l = \frac{1}{d} \left(i - C_1 \frac{dv}{dt} \right),\tag{4.3}$$

$$v = \frac{1}{d} \left(v_b + L \frac{di_l}{dt} \right).\tag{4.4}$$

These expressions can then be implemented in SIMULINK[®] as shown in Figure 4.5 for equation (4.4).

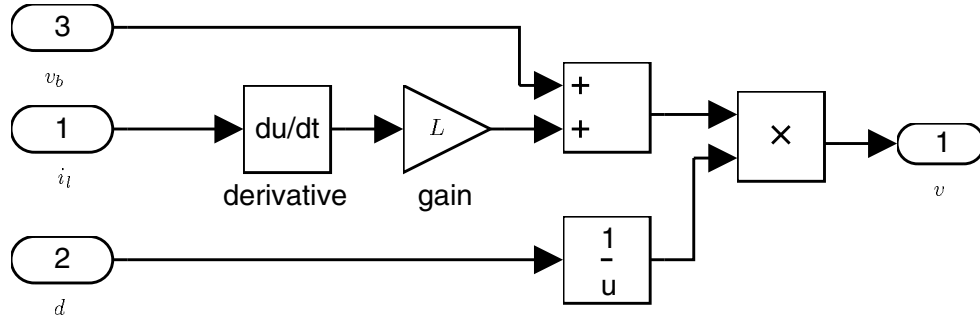


Figure 4.5: SIMULINK[®] implementation of equation (4.4).

Three subsystems, each representing one of the equations (4.2)–(4.4), are combined to form a buck converter simulation model as shown in Figure 4.6. The chosen form of equations (4.2)–(4.4) permits the use of the output voltage v of the converter as a direct input to the previously-discussed model of the solar panel. In the same way the converter output current i_b can be used as a direct input to the battery simulation block.

The boost converter

The basic expressions describing the boost converter were given in section 2.3.2 as equations (2.83) and (2.84). These can be used as discussed above to derive the

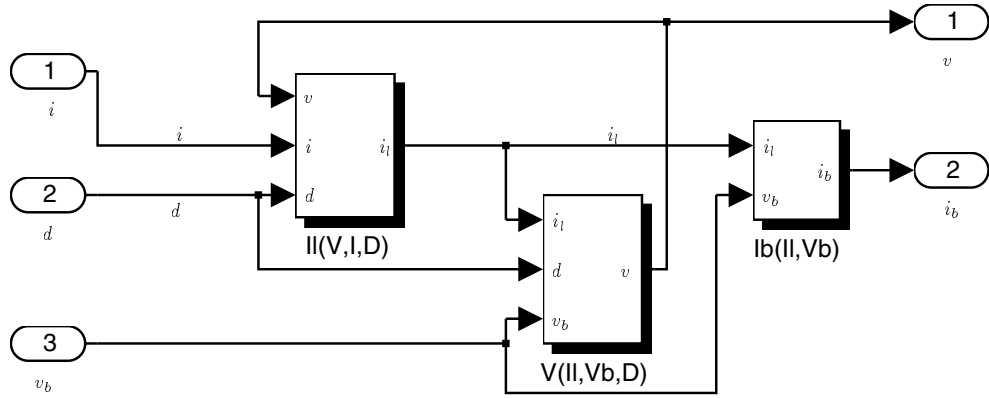


Figure 4.6: Block diagram for the simulation of a buck converter.

averaged model:

$$\begin{aligned}
 C_1 \frac{dv}{dt} &= d(i - i_l) + d'(i - i_l) = i - i_l, \\
 C_2 \frac{dv_b}{dt} &= d(-i_b) + d'(i_l - i_b) = (1 - d)i_l - i_b, \\
 L \frac{di_l}{dt} &= dv + d'(v - v_b) = v - (1 - d)v_b.
 \end{aligned} \tag{4.5}$$

The equations are then rearranged to allow the interconnection of the boost converter simulation block with the remaining system:

$$i_l = i - C_1 \frac{dv}{dt}, \tag{4.6}$$

$$i_b = (1 - d)i_l - C_2 \frac{dv_b}{dt}, \tag{4.7}$$

$$v = (1 - d)v_b + L \frac{di_l}{dt}. \tag{4.8}$$

These equations are implemented in SIMULINK[®] in the manner discussed in the previous section for the buck converter. The corresponding block diagram can be found as Figure A.2 in Appendix A.

The buck-boost converter

The basic buck-boost converter equations were derived as (2.109) and (2.110) in section 2.3.3. Their averaged system can be given as

$$\begin{aligned}C_1 \frac{dv}{dt} &= d(i - i_l) + d'i = i - di_l, \\C_2 \frac{dv_b}{dt} &= d(-i_b) + d'(-i_l - i_b) = -i_b - (1 - d)i_l, \\L \frac{di_l}{dt} &= dv + d'v_b = dv + (1 - d)v_b.\end{aligned}\tag{4.9}$$

These are then transformed into a form which allows the converter to be interconnected with the other system components:

$$i_l = \frac{1}{d} \left[i - C_1 \frac{dv}{dt} \right],\tag{4.10}$$

$$i_b = -(1 - d)i_l - C_2 \frac{dv_b}{dt},\tag{4.11}$$

$$v = \frac{1}{d} \left[\frac{di_l}{dt} - (1 - d)v_b \right].\tag{4.12}$$

The equivalent block diagram for the SIMULINK[®] simulation is shown as Figure A.3 in Appendix A.

4.1.4 The MPPT Controller

The various MPPT-control algorithms are implemented in a similar fashion as the other system components discussed in the previous sections. In addition to the function and operator blocks used in the other systems, a truth table block and several logical operators are employed to allow for conditional system states. The corresponding figures can be found in Appendix A.

All simulated MPPT systems directly control the PWM input of the dc-to-dc converter by adjusting its duty ratio d in increments of $\Delta d = 0.001$. This number

has been experimentally found using SIMULINK® to be suitable for quick, accurate, and reliable tracking of the MPP. Figure 4.7 shows the controller block with panel voltage v and current i as its input values and d as the output.

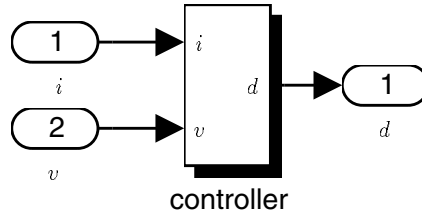


Figure 4.7: The MPPT controller generates the PWM control variable d directly.

4.2 The MPPT simulations

The only way to evaluate the performance of a digital feedback controller in an analog system before building an actual prototype is by simulation. As already mentioned earlier, conventional methods of closed-form transfer-function analysis fail because it is not possible to include the discrete states of an algorithm into a continuous-time transfer-function.

SIMULINK® provides methods not just to tackle the complexity resulting from the mixed discrete-continuous system, but also to simulate the changing operating conditions in the environment of a moving vehicle. As the vehicle moves along a certain route, the angle of incidence (AOI) of the solar irradiance on the photovoltaic panels changes constantly depending on the vehicle's position and its orientation towards the sun. Furthermore, shadows of structures, vegetation, and clouds will result in sudden changes in insolation, which in turn lead to a corre-

sponding change in cell temperature. All these factors influence the characteristics of the photovoltaic cells as discussed earlier in Chapter 2.

The simulations provide the valuable opportunity to evaluate the various MPPT techniques presented earlier and analyze their behavior under the exact same operating conditions. This comparative study will yield which MPPT method is best suited for use in a moving car.

4.2.1 Operation under stable environmental conditions

For this series of simulations the parameters temperature T and insolation S are kept constantly equal to standard test conditions (STC). The main focus will be on the power ripple caused by oscillations around the MPP and its dependency on both the sampling frequency of the various MPPT techniques and the employed dc-to-dc converter.

The P&O method

The P&O MPPT method, as introduced in section 3.4.1, is a very commonly used technique for operating a photovoltaic cell array at or close to its point of maximum efficiency (MPP).

Figure 4.8 shows the signals of the solar panel output power and operating voltage, the battery voltage, and the duty ratio d of a P&O-controlled power supply employing a buck converter.

The battery was given an initial output voltage v_b of 95 V to simulate the discharged 108 V battery block used in the solar car SOLTRAIN. The initial output of the MPPT was set to $d = .65$.

During the first approximately 25 seconds the battery voltage rises quickly to

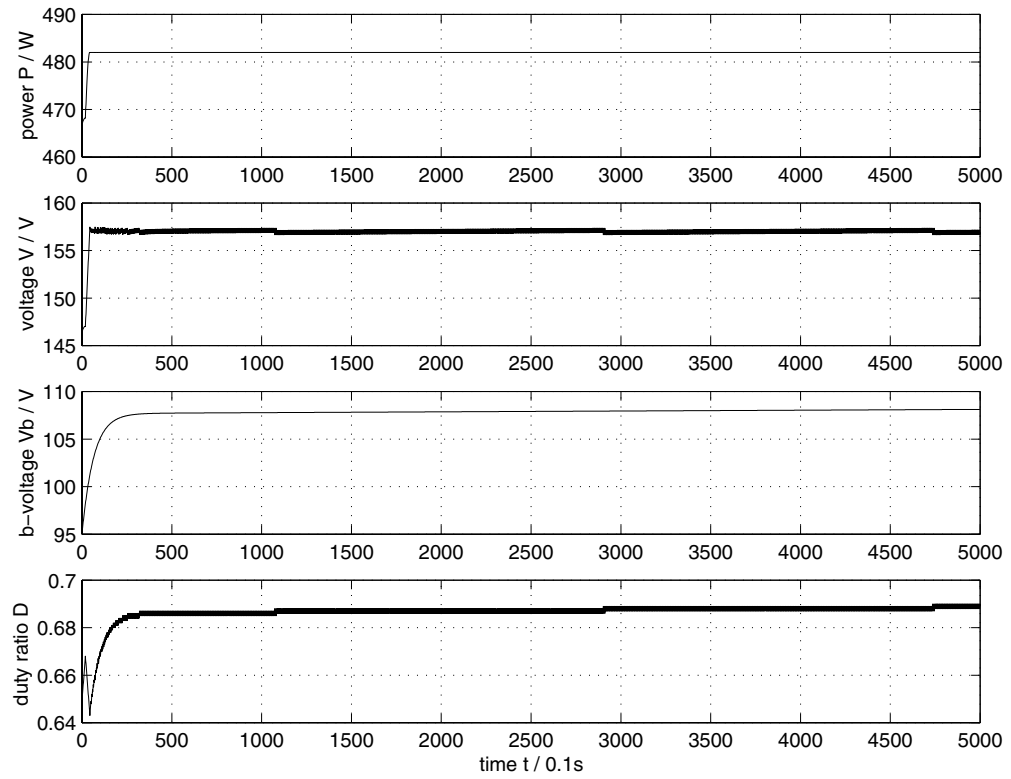


Figure 4.8: Simulation of the P&O MPPT method in combination with a buck converter under stable environmental conditions. Five standard solar panels with 7×8 photovoltaic cells each were connected in series.

a level of about 108 V, where it stabilizes. This rise is caused by the overvoltage or polarization effect mentioned in section 2.2. But even though the battery voltage is still on the rise, the MPPT manages to adjust the duty ratio d very quickly such that a stable power output is reached. After this point the output power does not change any further since the solar panel operates under constant conditions.

Close inspection of the presented curves in Figure 4.8 reveals that the battery voltage slowly rises throughout the whole simulation. This is caused by the charging process of the batteries, which causes the battery voltage to rise by about 30 % between the uncharged and the charged battery state [SCL92]. This slow voltage increase on the battery side of the system causes a corresponding change in the operating voltage at the solar panel. The MPPT, however, continues to readjust the duty ratio d and therefore prevents a deviation from the optimum operating point.

Figure 4.9 presents a more detailed look at the signals of the simulated system, revealing the continuous oscillation of the operating point around the point of maximum power (MPP). This is a result of the continuous perturbation of the operating voltage in order to find the MPP — a problem previously discussed in the introduction of the P&O MPPT method in section 3.4.1. A stepwise comparison of the control signal d in the bottom curve with the discrete power signal in the middle curve shows how the control signal changes its stepping direction every time a decrease in power is detected. This continuous oscillation is fundamental to the P&O method.

The top curve in Figure 4.9 shows the actual output power signal at the solar panel. It can be seen that the signal alternates between two minima, one of which is lower than the other. This is the result of the two different slopes in the P - V

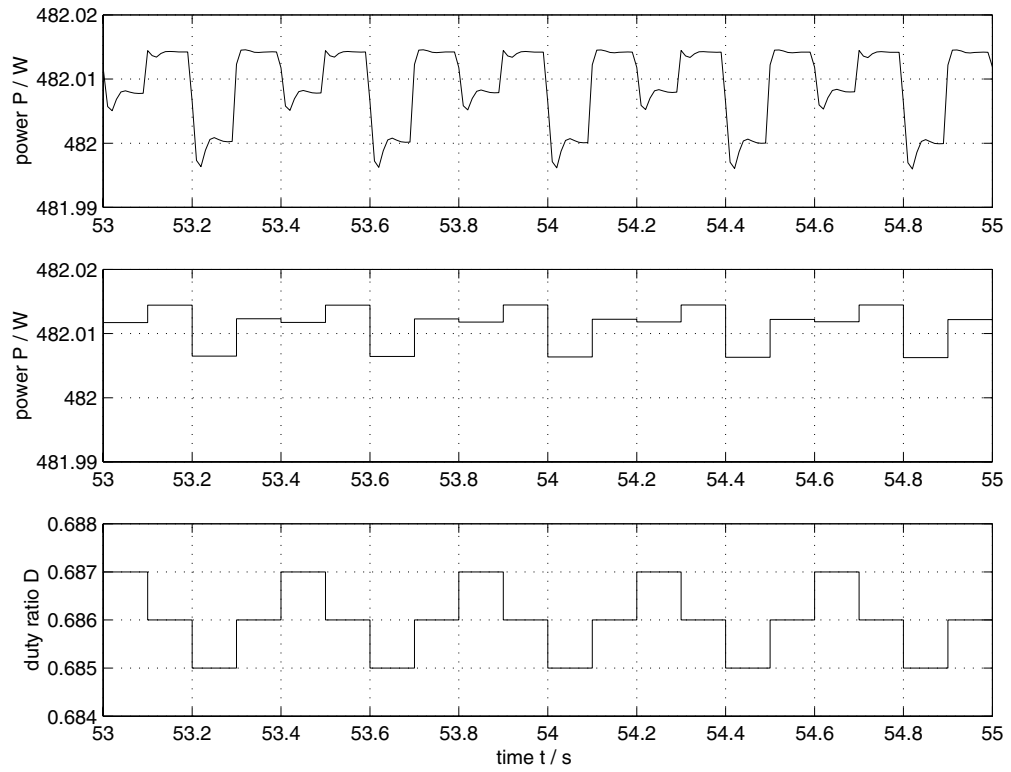


Figure 4.9: Detailed plot of the waveforms of the P&O MPPT simulation with a buck converter. The top curve represents the power signal at the panel, whereas the center curve shows the discrete ("sampled") power signal. The bottom curve is a plot of the MPPT output: the duty ratio d .

characteristics of the photovoltaic cells (Figure 2.10) and the alternating overshoot of the operating point into these two directions.

Furthermore, the power signal shows a slight ringing at every single perturbation step. This represents the system's step response. The ringing diminishes very quickly which is an indication of good damping characteristics and stability. Since the simulations rely on idealized equations — neglecting all the damping parasitic resistances in the dc-to-dc converter — the real system will have even better damping and a smaller overshoot.

The simulations discussed so far used a MPPT sampling frequency of 10 Hz. To allow the MPPT to react quickly to changes in operating conditions, this sampling rate can be increased. However, Figure 4.10 illustrates the reaction of the system if the sampling time of the discrete controller is higher than the response time of the controlled configuration of solar panel, battery, and dc-to-dc converter.

Comparison of the control and the power signal in Figure 4.10 shows the MPPT's reaction to a decrease in output power: as desired, the direction in which it perturbs the system's operating voltage is changed. But if it does this at a very high frequency, the power supply system does not have enough time to react to this change, so the power is still decreasing at the next sampling step. This triggers another change in the direction of the control variable. A permanent oscillation of d results until the power decrease slows down. After the MPPT manages to move the operating point towards the MPP again, the overshoot towards the other side of the power maximum causes the same problem. A high amplitude oscillation of the operating point around the MPP, associated with power losses, is the consequence. The limiting sampling frequency at which this phenomenon starts to occur with the buck converter has been found to be approximately 125 Hz.

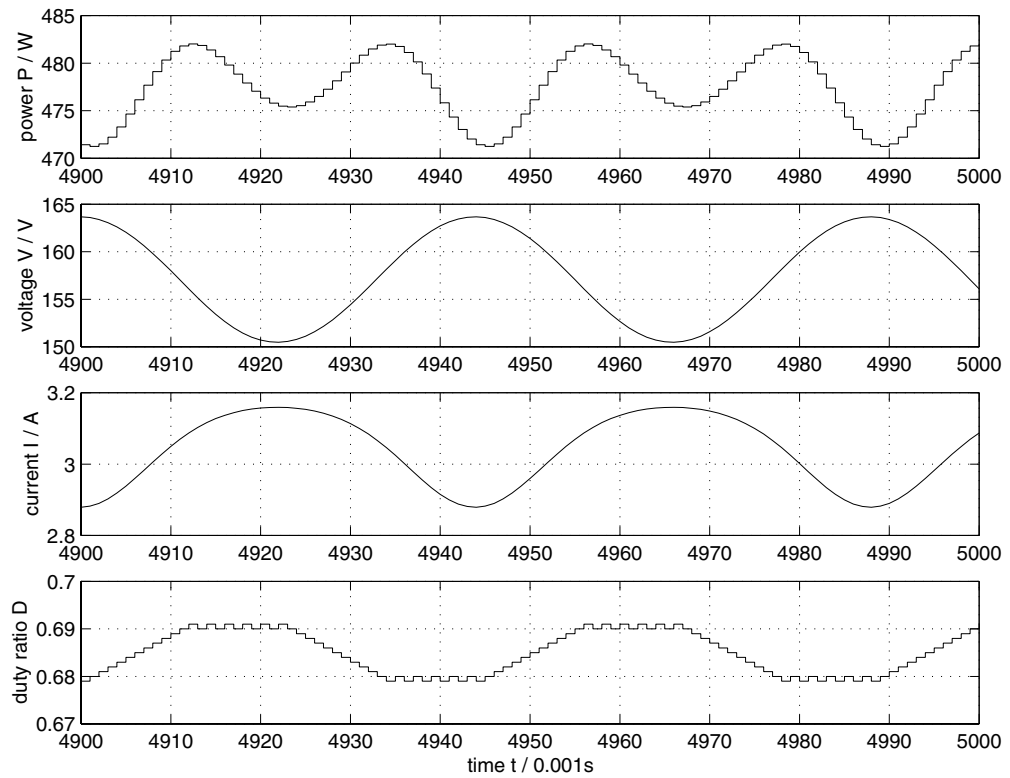


Figure 4.10: Oscillations of P&O MPPT with a buck converter at a high frequency sampling rate (1000 Hz).

Further simulations have been done for a solar power supply system with P&O MPPT employing a boost converter. At a sampling rate of 100 Hz it shows the P&O-characteristic low amplitude oscillations around the MPP under stable environmental conditions (Figure 4.11). The top curve shows that the dynamic response of the system to a step of the control input is not as well behaved as it was for the system employing the buck converter. However, the digital feedback control has a stabilizing effect on the system which prevents instability. Nevertheless the overshoots shown in Figure 4.11 result in an increase in system losses.

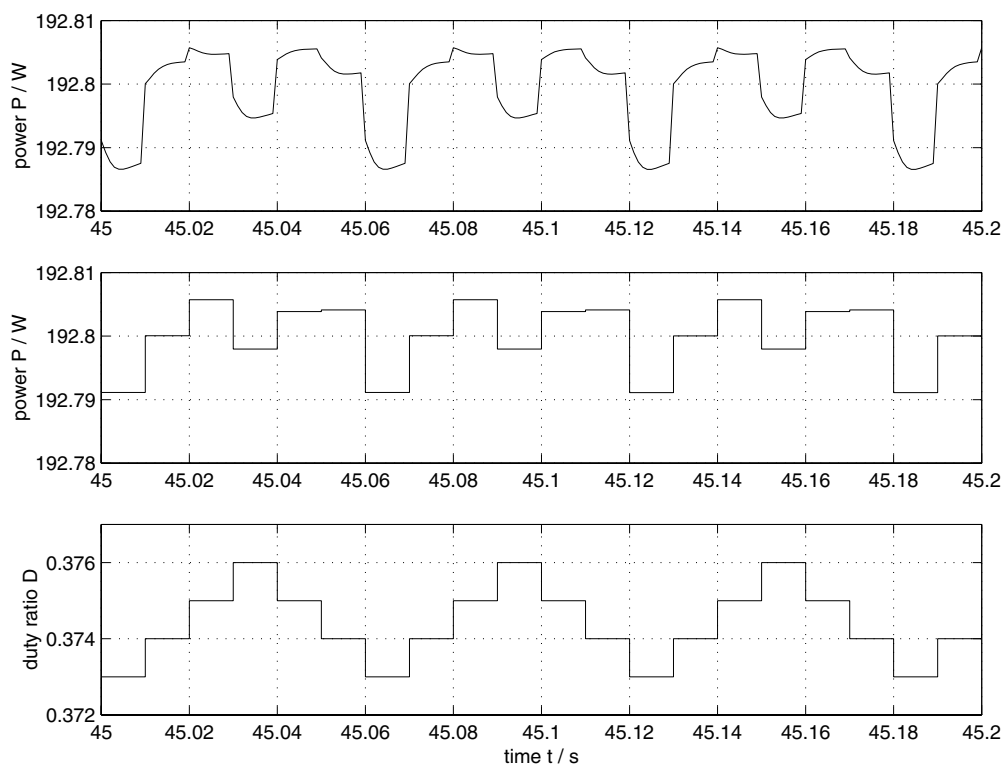


Figure 4.11: Detailed plot of the panel output power signal, its discrete equivalent, and the control variable d of a system with P&O MPPT and a boost converter. The sampling frequency is equal to 100 Hz.

An increase of the MPPT's sampling frequency to 1 kHz has same effect as in

the configuration with the buck converter: the system is too slow to react to the short term corrections induced by the controller. Figure 4.12 shows how this causes significant oscillations around the MPP. The limiting frequency for this effect in a boost converter configuration has been determined to be approximately 160 Hz.

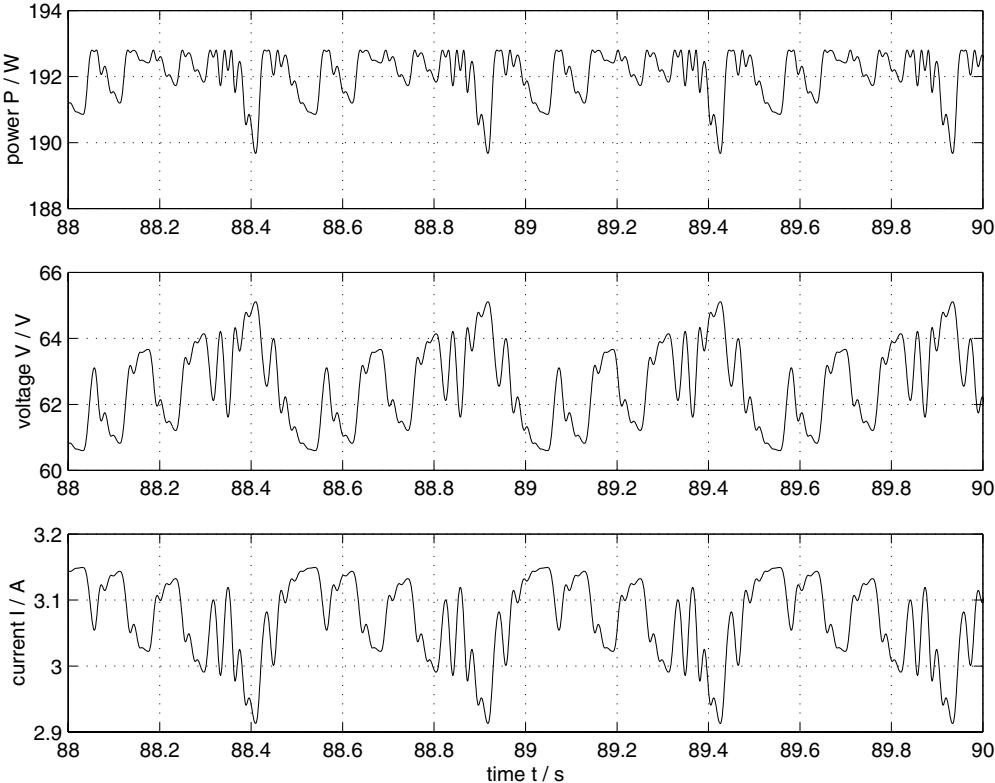


Figure 4.12: Signals for power P , voltage V and current I at a solar panel in a system with P&O MPPT on a boost converter at 1000 Hz.

Additionally, Figure 4.12 reveals a certain pattern in the described oscillations completely different from the oscillations seen in the earlier simulations with the buck converter. This is an indicator for a diminished robustness of the boost converter system. It is the battery voltage — slowly increasing throughout the charging process — that causes a continuous distortion of the system which needs

to be compensated by the MPPT. Since the controller starts oscillating around the current operating point as long as a rapid decrease in output power occurs (see Figure 4.13), this distortion can not be completely neutralized at these high sampling frequencies.

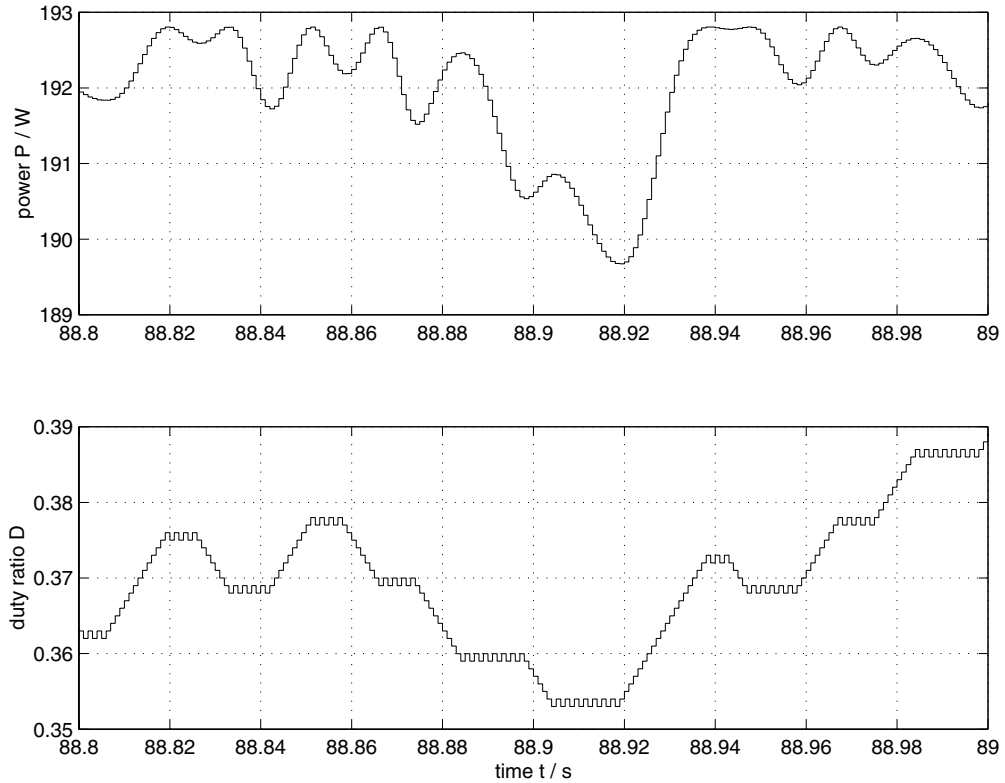


Figure 4.13: Details of the discrete power signal and the control variable d of the system with P&O MPPT on a boost converter at 1000 Hz.

Finally, the buck-boost converter has the great advantage of having a continuous operating range between step-down and step-up operation. It is therefore possible to choose its output voltage to be lower, equal, or even higher than its input voltage. The output voltage is negative, which means the battery and any other load on its bus must be connected accordingly. Figure 4.14 shows the signals

of such a configuration connected to four solar panels of 7×8 photovoltaic cells in series.

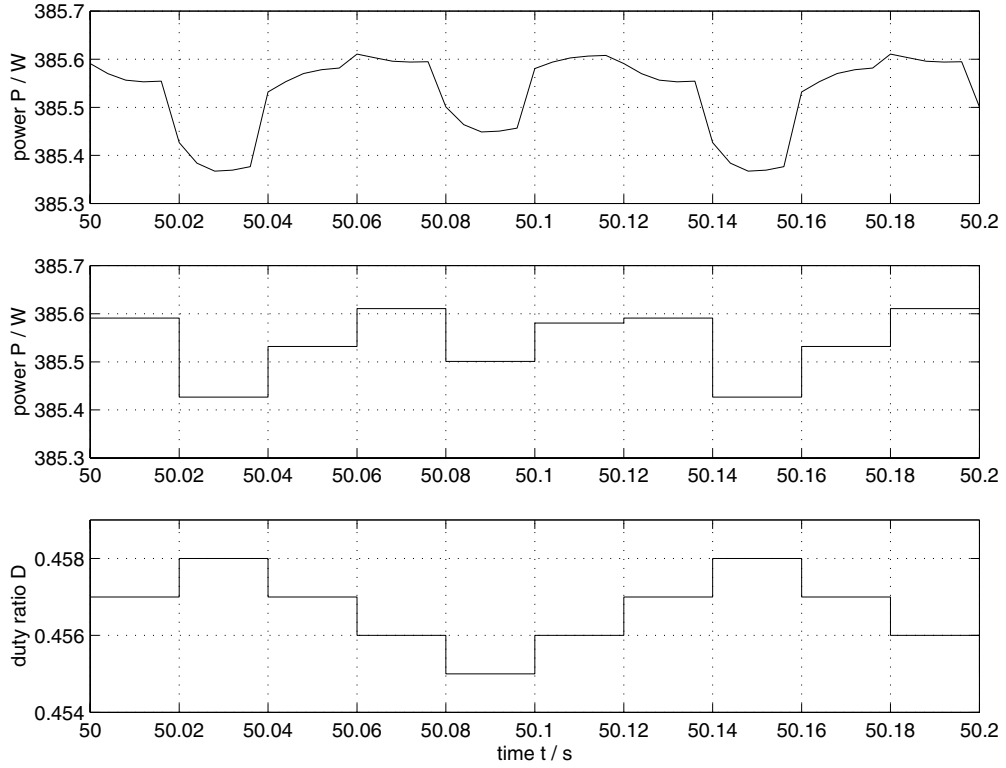


Figure 4.14: Detailed plot of the power signal, its discrete equivalent, and the control variable d of a system with P&O MPPT and a buck-boost converter under constant environmental conditions. The sampling frequency is equal to 50 Hz.

The output power signal (top curve of Figure 4.14) shows almost the same step response and ripple amplitude as the buck converter system: it is not very well behaved but stabilized by the digital feedback control. The typical P&O oscillations around the MPP occur here as well and do not differ from the ones observed with the other converters.

The plot in Figure 4.15 shows the power and control signals at an increased sampling frequency of 200 Hz. It reveals the same effect as has been observed for

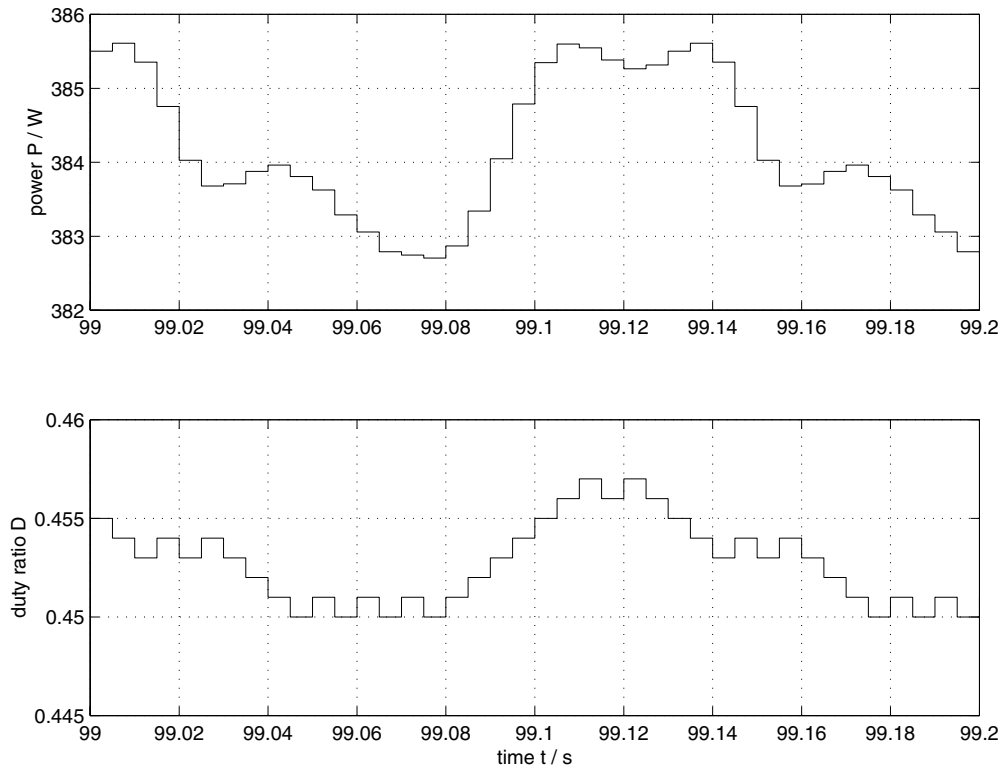


Figure 4.15: Discrete power signal and control variable d of the P&O algorithm at a sampling frequency of 200 Hz in combination with a buck-boost converter.

the systems employing the buck converter or the boost converter at high sampling frequencies: the amplitude of the oscillations in the output power is increased due to a permanent oscillation of the MPPT output during a falling power signal. It should be noted that the threshold frequency for this effect for a buck-boost converter system lies around 100 Hz.

The improved P&O algorithm

In section 3.4.1 an improved version of the regular P&O MPPT method was presented. Its aim is to prevent a deviation from the MPP during rapidly increasing insolation levels. Figure 4.16 shows a closeup of the discrete power signal and the control signal d of this improved algorithm with a buck converter and STC environmental conditions.

The signal graph in Figure 4.16 reveals how this improved algorithm distinguishes itself from the conventional P&O method: after two consecutive increases in output power the controller reverses the direction of the perturbation to make sure the power increase is actually caused by its own action and not by some other factor like an increase in insolation. This control condition occurs every six cycles at an operation at 100 Hz under constant environmental conditions.

Figure 4.17 shows how the improved algorithm performs at a sampling frequency of 1 kHz.

At this higher sampling frequency, the regular P&O method oscillates significantly with an amplitude of about 10 W (Figure 4.10). This is equivalent to an approximate 2% loss of the maximum possible output power. As Figure 4.17 reveals, this oscillation and the related losses are significantly reduced by this improved P&O algorithm. Both algorithms react to the falling power signal with

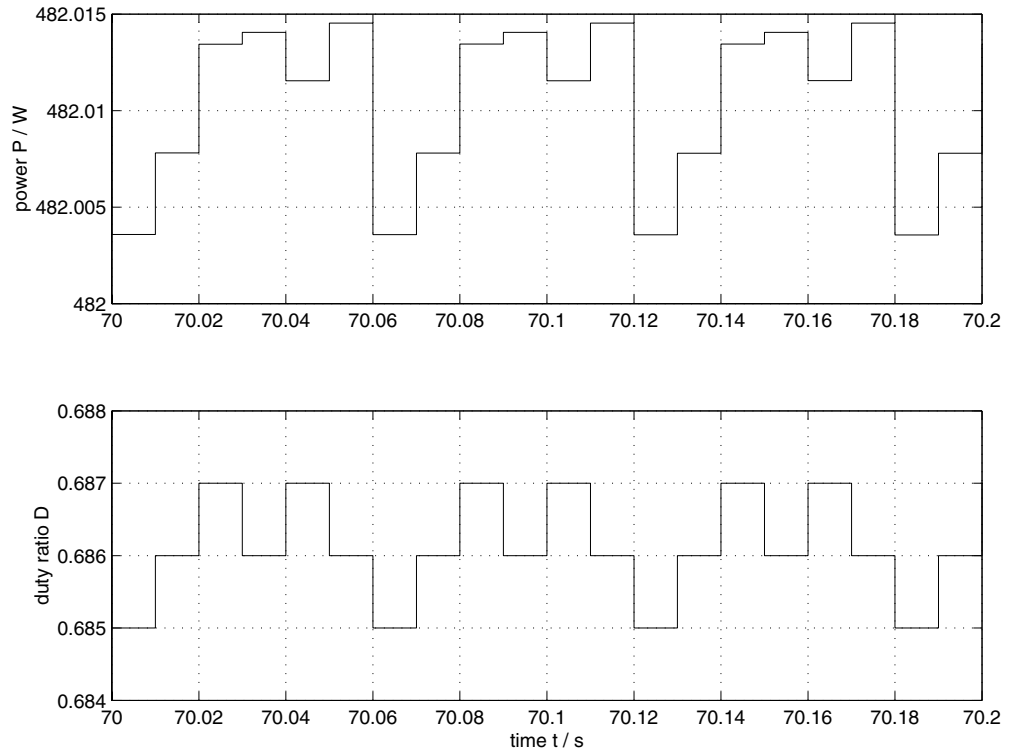


Figure 4.16: Plot of the steady-state oscillations of the improved P&O MPPT mechanism with a buck converter at a sampling frequency of 100 Hz.

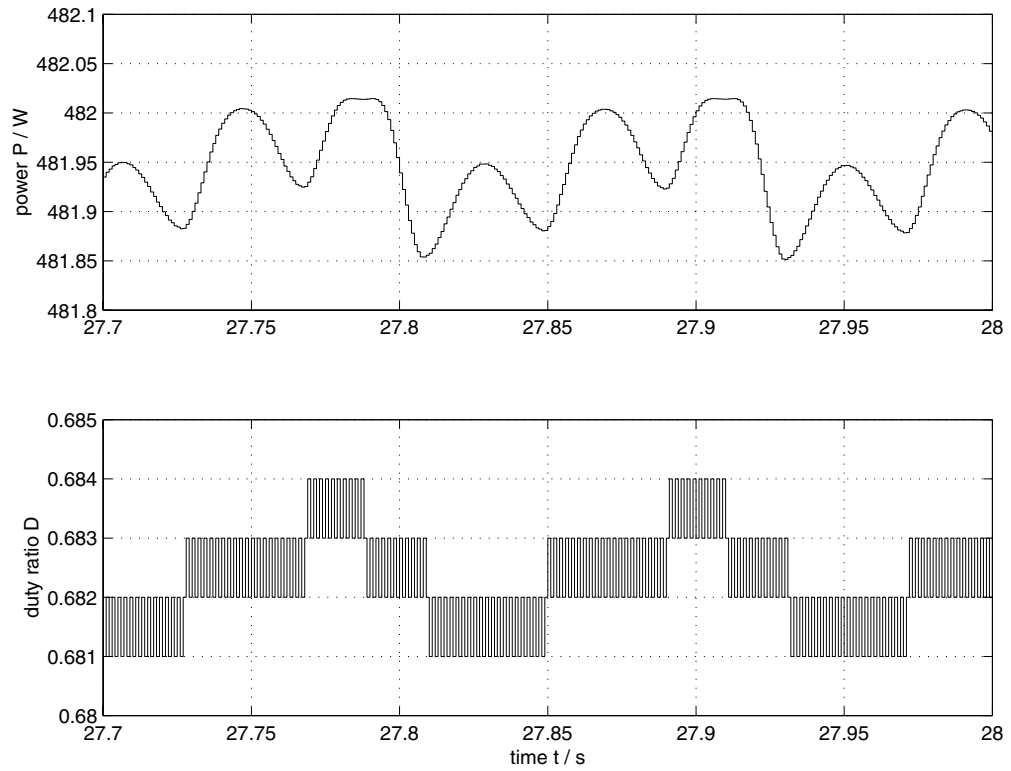


Figure 4.17: Output power ripple with an improved P&O algorithm at a buck converter operating at 1000 Hz.

oscillations of the control variable around the current operating point. The advantage of the improved method is that the control variable also oscillates around its current operating point when the power signal is rising. As a result, the controller does not drift off in one direction as it did with the conventional method (Figure 4.10). This results in a much better damping characteristic of the system and yields a reduction of the steady-state power losses to approximately 0.02 %. However, operation at this high sampling frequency should be omitted since the ripple losses are still ten times higher than for operation at 100 Hz.

Independently of the employed converter type, the improved P&O MPPT method decreases the steady-state output power ripple slightly for sampling frequencies below the previously determined thresholds. For a higher sampling ratio the ripple and the associated losses are significantly reduced. But since ripple losses increase exponentially after crossing this threshold frequency, it is still not desirable to operate the MPPT at such high frequencies.

The corresponding signal curves showing the power and control signal for the boost and the buck-boost converter controlled by the improved P&O method can be found in Appendix B.

Simulation of the IncCond method

In section 3.4.2 the incremental conductance (IncCond) MPPT method was introduced. With the IncCond algorithm (Figure 3.5) the control variable is changed dependent on the sign of the derivative $\frac{dP}{dV}$. Further evaluated factors are the incremental changes dI and dV .

Figure 4.18 shows the discrete output power signal and the control variable d of an IncCond controlled MPPT system at a sampling frequency of 100 Hz employing

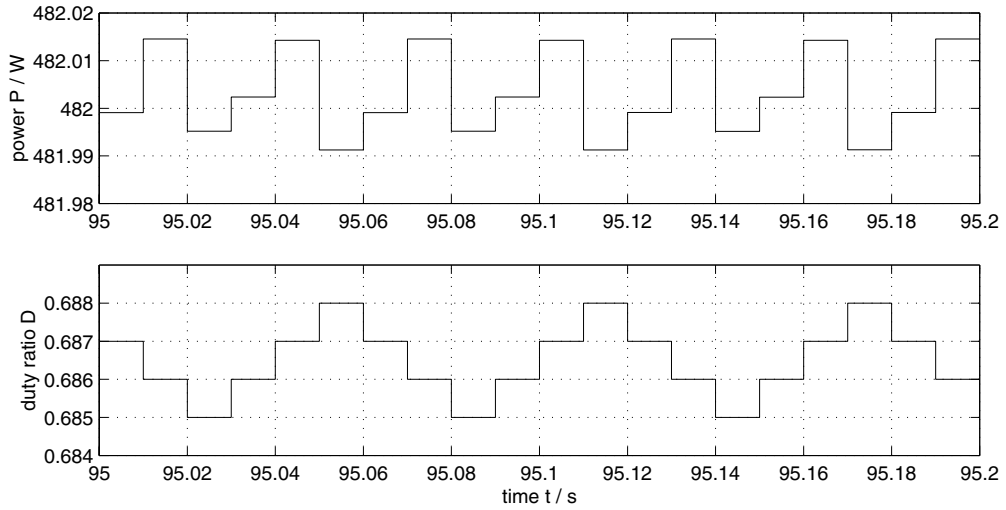


Figure 4.18: Power and control signal of a simulation of a IncCond MPPT algorithm in combination with a buck converter at a sampling frequency of 100 Hz.

a buck converter. The obvious oscillation of the power signal shows the fact that the MPP condition $\frac{dI}{dV} = -\frac{I}{V}$ (equation (3.5)) never occurs. A satisfaction of this condition would cause the algorithm to bypass the step of perturbing the control variable as soon as the maximum power point was reached. The approximation of the values dI and dV and the high resolution of the sampling input to the MPPT prevents satisfaction of (3.5) and of the conditions $dV = 0$ and $dI = 0$. Consideration of the IncCond flow chart diagram on page 74 shows that under these circumstances the IncCond method does not distinguish itself significantly from the simple P&O technique: the control variable is perturbed for every cycle of the tracking algorithm until the MPP is passed. Then the perturbation is reversed to start the same process in the opposite direction. This leads eventually to a continuous oscillation around the MPP.

Figure 4.19 shows the higher frequency response oscillations phenomenon with the IncCond algorithm. This is an expected behavior, since this depends on the

response time of the system which varies with the employed dc-to-dc converter and not with the employed MPPT.

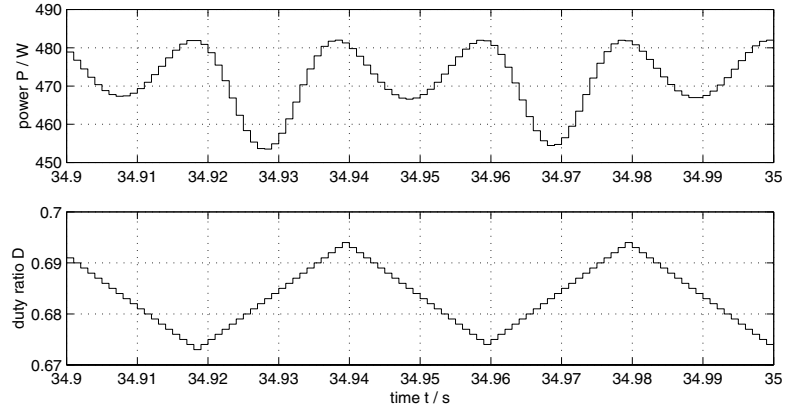


Figure 4.19: Power and control signal of a simulation of the IncCond MPPT algorithm in combination with a buck converter at an increased sampling frequency of 1 kHz.

Simulations of the IncCond MPPT in combination with a boost and a buck-boost converter closely resemble the ones performed with the previous configurations with these two converter types and can be found in Appendix B.

The information obtained with the simulations discussed so far is summarized in Table 4.1. It is shown that the increased ripple at higher sampling frequencies of the MPPT causes a significantly higher power loss. Additionally it can be seen that the modified P&O algorithm results in a considerable improvement over the conventional P&O technique. The IncCond algorithm is limited in its performance by the fact that its maximum power condition (equation (3.5)) is never fulfilled.

At this point, one would conclude to favor the buck converter configuration with its well behaved system response and associated low power losses (as long as the sampling frequency stays below the threshold of 125 Hz). However, since each

		Power ripple losses in %	
		MPPT sampling frequency	
MPPT	converter	100 Hz/50 Hz ^a	1 kHz/200 Hz ^a
P&O	buck	0.0031	2.12
	boost	0.0078	1.47
	buck-boost ^a	0.05	0.653
P&O improved	buck	0.0021	0.031
	boost	0.0046	0.041
	buck-boost ^a	0.023	0.052
IncCond	buck	0.0052	5.934
	boost	0.002	1.634
	buck-boost ^a	0.044	0.6

^aSince the threshold sampling frequency for the MPPT which causes increased power oscillations lies lower for a system with a buck-boost converter, the buck-boost version has been simulated at lower sampling rates.

Table 4.1: Comparison of the ripple losses for the different MPPT techniques under steady-state conditions (STC).

converter covers a different conversion range², all three converter types must still be studied in all further considerations.

The improved IncCond method

The simulations of the IncCond method revealed that the maximum power condition (3.5) never occurs. An oscillation around the MPP — similar to the one observed with the simple P&O technique — is the result. This causes the accompanying power losses to be in the same range as they are with the P&O algorithm (see Table 4.1).

To overcome this obstacle which prevents the IncCond algorithm from using its intended features, the maximum power condition can be modified. As previously discussed in section 3.4.2 (equation (3.10)), a small marginal error ϵ is added such that

$$\left| \frac{dI}{dV} + \frac{I}{V} \right| \leq \epsilon.$$

Further simulations had the best results in ripple reduction with an $\epsilon = 0.0002$ and the change of the condition $dI = 0$ to $|dI| \leq 0.02$. With this improved IncCond algorithm the ripple and the associated power losses were reduced by approximately 70%. This makes the power ripple performance of the IncCond algorithm superior to the simple P&O technique, as intended [HMHO95]. A comparison of this improved IncCond method with the improved P&O algorithm only revealed minor differences in their ripple behavior and the associated power losses,

²The conversion range is determined by the converter's conversion ratio, which is defined as the fraction $\frac{V_b}{V}$. The nominal battery voltage V_b is equal to 108 V, while the solar array voltage V is proportional to the number of solar panels connected in series. The buck converter was simulated as operating at five panels each having 7×8 photovoltaic cells in series ($V_{mp} \geq V_b$); the boost converter on two equal panels ($V_{mp} \leq V_b$), and the buck-boost converter on four panels ($V_{mp} \approx V_b$).

with the IncCond being slightly superior.

4.2.2 Performance under changing insolation levels

The four digitally controlled MPPT techniques (P&O, improved P&O, IncCond, and improved IncCond) were first simulated employing a buck converter in an environment of changing insolation levels. Five standard solar panels of 7×8 solar cells were connected in series and through the dc-to-dc converter connected to the simulated 108 V SOLTRAIN battery pack.

Slow increase in insolation

A slow increase in insolation from 500 W/m^2 to 600 W/m^2 over a time period of 10 seconds was simulated, whereas the temperature was kept constant at $25 \text{ }^\circ\text{C}$. Observation of the output power curves of the various configurations led to the graph shown in Figure 4.20.

It can be seen that the continuous perturbation of the control variable d due to changing operating conditions (e. g., changing insolation) leads to an oscillation in the output power signal. All four MPPT techniques show this behavior. Furthermore, it can be noticed that the output power of the improved P&O technique rises slower and with a smaller oscillation than the power of the other MPPT methods. This is caused by the intended reaction of the improved P&O to an increase in insolation: the control variable is kept oscillating around a constant value until the power increase ends. This prevents a deviation of the operating point from the MPP as discussed in Figure 3.4. In fact, the high amplitude oscillations of the other MPPT techniques during the period of increasing insolation are nothing but a repeated deviation of the operating point in both directions of the MPP. Fortu-

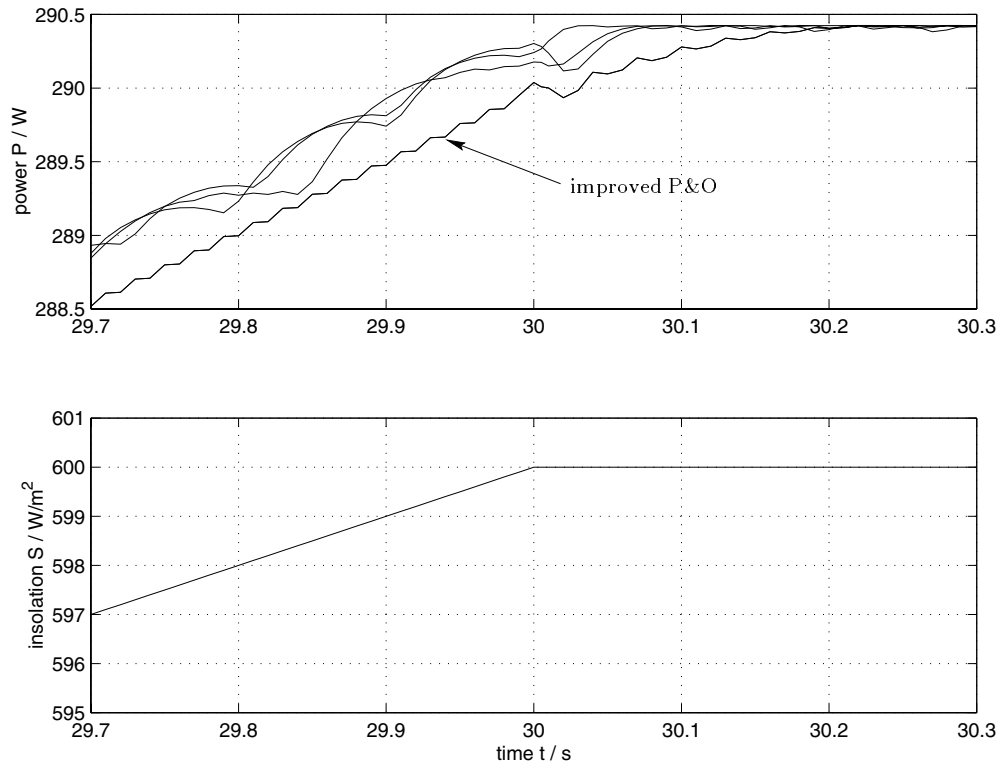


Figure 4.20: Power output signals of the various MPPT configurations under an increase in insolation from 500 W/m^2 to 600 W/m^2 . The improved P&O method shows the smallest oscillations during the rise but as well causes a reduced power output.

nately, the insolation increase is slow and the MPPTs are fast enough to always find their way back to the MPP. In this case, the idling state of the improved P&O method results in a slightly reduced power output.

Rapid increase in insolation

Next, a rapid increase in solar irradiance from 500 W/m^2 to 1000 W/m^2 within a time period of 5 seconds was simulated. The cell temperature was kept at a constant value of 25°C . Under these operating conditions the advanced algorithm of the improved P&O MPPT method becomes more significant. Figure 4.21 shows how the power output of the improved P&O MPPT increases linearly, whereas the other MPPT techniques experience a vast deviation from the MPP.

Inspection and comparison of the the panel voltage and the control variable d shown in the same figure reveal the problem discussed in Figure 3.4: the rapidly increasing power generated by the step increase in insolation causes the MPPT to continuously perturb the control variable in one constant direction. All MPPTs except the improved P&O are unable to detect this problem and as a result increase their duty ratio up to their physical limit of $d = 1$. Only after the insolation increase ends do these methods recover from their error.

Figure 4.21 further shows how the improved P&O algorithm keeps the control variable constant for the time of the increase, waiting for the power signal to stabilize again. At the end of the increase only a minor correction is required to move the operating point to the new MPP. A look at Figure 2.8, which shows the P - V -characteristics of a solar panel for various insolation levels, reveals how the values of V_{mp} vary only slightly over the whole presented range of insolation. This allows the improved P&O algorithm to delay the adjustment of its control variable

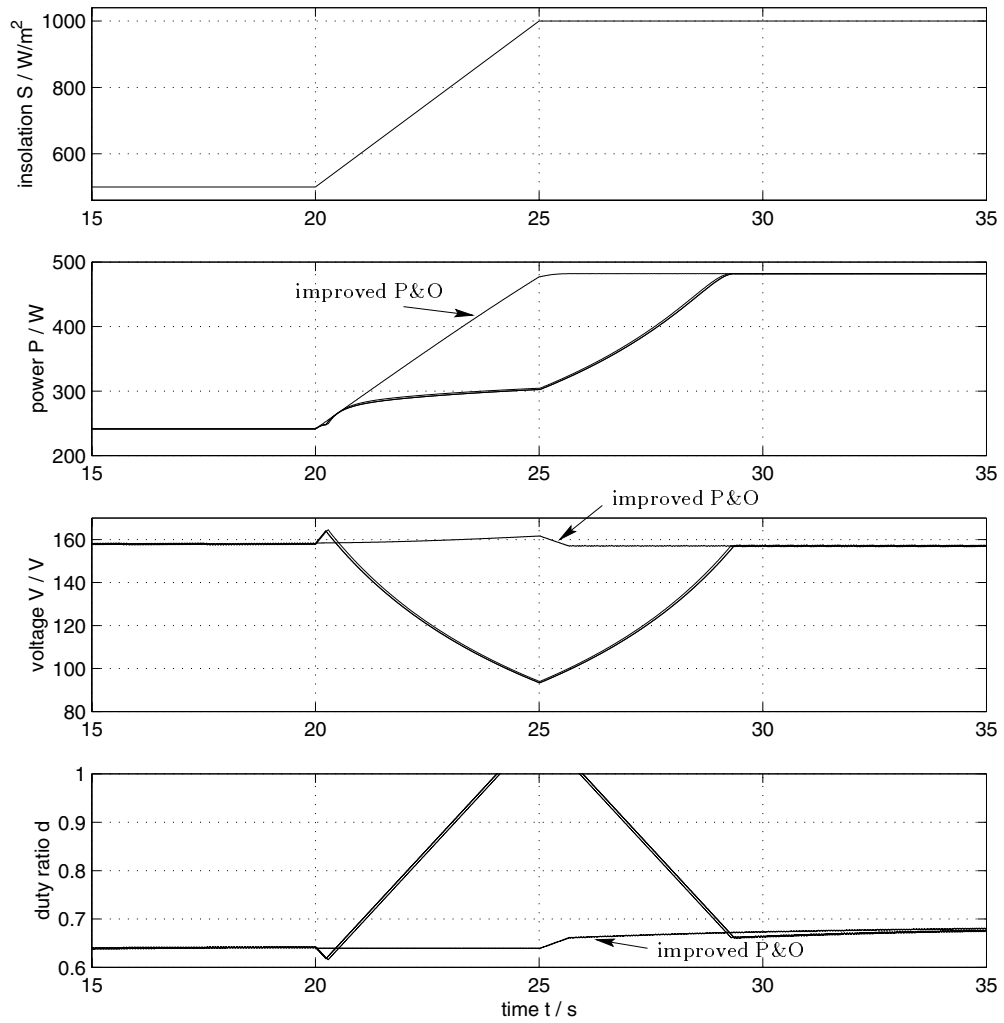


Figure 4.21: Comparison of the various MPPT's signals for output power, panel voltage, and the control variable d under rapidly increasing insolation levels.

without suffering significant power losses.

This ability to detect a rapid increase in insolation and avoid an associated deviation from the MPP presents a significant advantage of the improved P&O algorithm over all the other MPPT techniques. The average power output of the system controlled by this advanced algorithm was found to be approximately 5% higher than the output from the systems controlled by the other MPPTs under these conditions.

Rapid decrease in insolation

A large drop in insolation from 1000 W/m^2 to 500 W/m^2 within a time period of 5 seconds was simulated employing the four digitally controlled MPPT systems. The temperature was kept constant at 25°C . This simulation led to the power curves and duty ratio signals presented in Figure 4.22.

The plots show how all the MPPTs kept their control variable oscillating at a constant point until the drop in insolation ended. This happens because in either perturbing direction of the control variable the output power is decreasing (as a result of the falling insolation levels). Since all the tested MPPT techniques react in the same way to this kind of situation, their resulting power output is almost identical.

At the point where the decrease in insolation ends, all four MPPT controllers detect the slight deviation from the MPP and readjust their control variable accordingly. This adjustment period is where the various MPPTs react and behave differently: the IncCond algorithm is slightly quicker than the improved IncCond or the P&O algorithm and significantly faster than the improved P&O method. The reason for this is that the IncCond method evaluates the slope $\frac{dP}{dV}$ of the

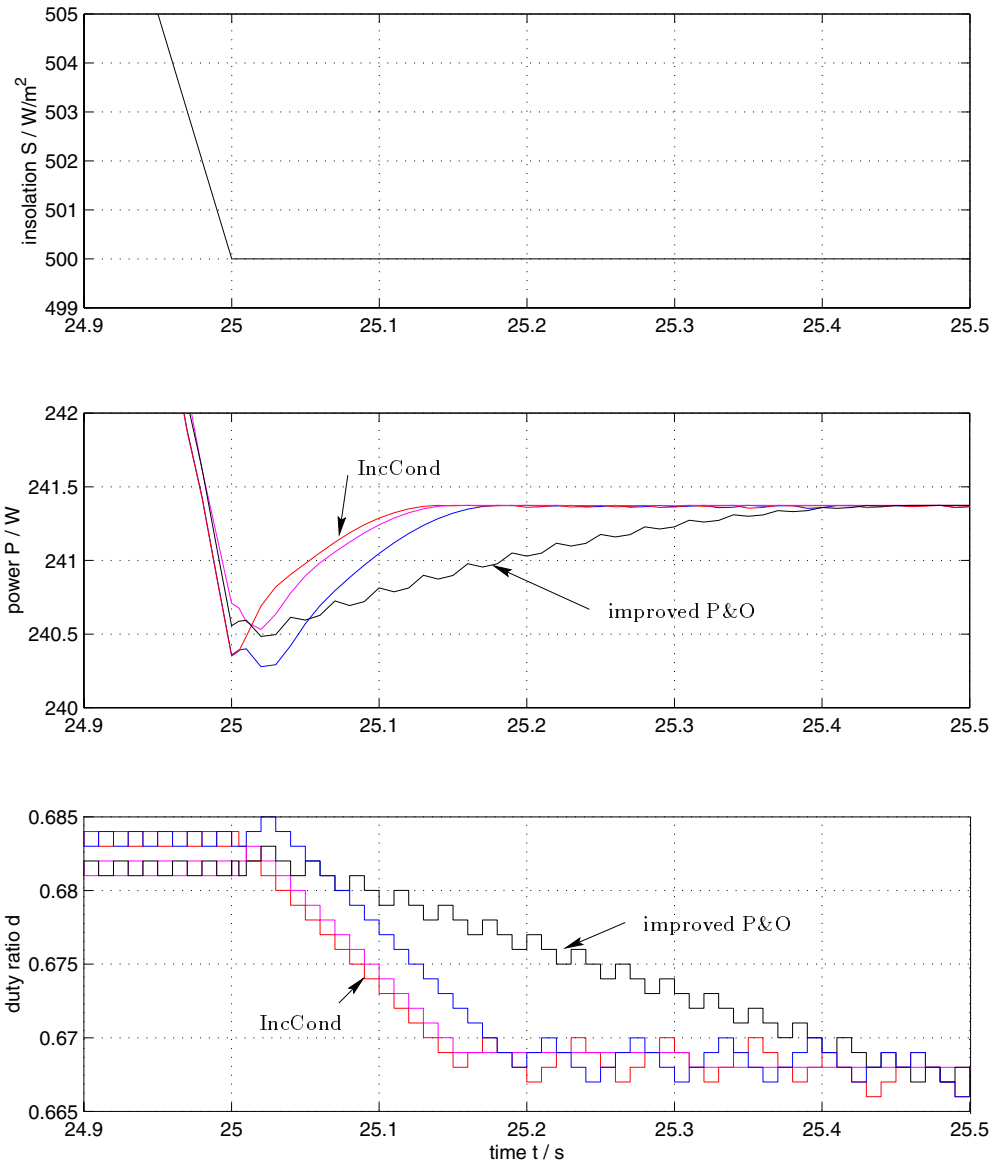


Figure 4.22: Power and control signal of the various MPPTs under quickly decreasing insolation levels.

P - V -characteristic to decide on the direction of perturbation for the control variable. This leads to the advantage that the IncCond control moves the operating point in the correct direction with its first adjustment step, whereas the P&O method has to find the right direction by ‘perturbing and observing’ and in this case initially attempts the wrong direction.

The difference in the performance of the conventional IncCond and the improved IncCond technique can be explained by the addition of the small marginal error ϵ to reduce the output power ripple. This modification makes the improved IncCond algorithm less sensitive to changes in the operating conditions.

The reason for the relatively slow adjustment of the operating point by the improved P&O controller is found in its extra added control condition (see section 3.4.1): if the power increases twice within two consecutive steps, the MPPT will change the perturbation direction of the control variable to prevent deviation from the MPP as illustrated in Figure 3.4. While this leads to the previously discussed advantages of this improved algorithm over all other MPPT techniques under quickly *increasing* insolation levels, it also causes a somewhat slower response as these levels are rapidly *decreasing*.

Slow decrease in insolation

A slowly decreasing insolation environment was also simulated. The monitored behavior was equivalent to that observed under rapidly decreasing irradiance levels. The resulting signals did not show any significant variation compared to the plots obtained in the previous section. The only difference was a reduction in amplitude due to the lowered insolation levels. The corresponding plots can be found as Figure B.9 in Appendix B.

Performance in combination with a boost or a buck-boost converter

All the previous simulations of varying insolation levels were performed employing a buck dc-to-dc converter. Since the buck is a step-down converter, its operation requires a higher number of serially connected solar panels and hence has a correspondingly higher power input than the other converters.³

The lower power output in combination with a boost or a buck-boost converter causes the tested MPPT techniques to react differently to changes in the operating conditions. The resulting signal curves for an increase in insolation from 500 W/m^2 to 1000 W/m^2 within 5 seconds are presented in Figure 4.23.

It can be seen how the improved P&O algorithm — like the simulations with the buck converter — keeps its control variable d oscillating around a certain point for the time of the insolation increase. This prevents the deviation from the MPP which is experienced with the other MPPTs. Unlike in the buck converter configuration, the other MPPT techniques manage to return the operating point to the MPP only to experience a deviation in the opposite direction caused by the increased effectiveness of the perturbation step size ($\Delta d = 0.001$) in relation to the diminished actual power output. This relatively increased Δd allows the MPPT to react faster to changes in environmental conditions and results in a detection of the deviation before the increase in insolation ends. The drawback of the larger step size is that it also leads to higher ripple losses under stable operating conditions. Thus a suitable value for Δd must be experimentally determined for every desired configuration.

The performance of the configurations employing the boost or the buck-boost converter was found to be equivalent to that of the various MPPT techniques

³see footnote 2 on page 113 for configuration details.

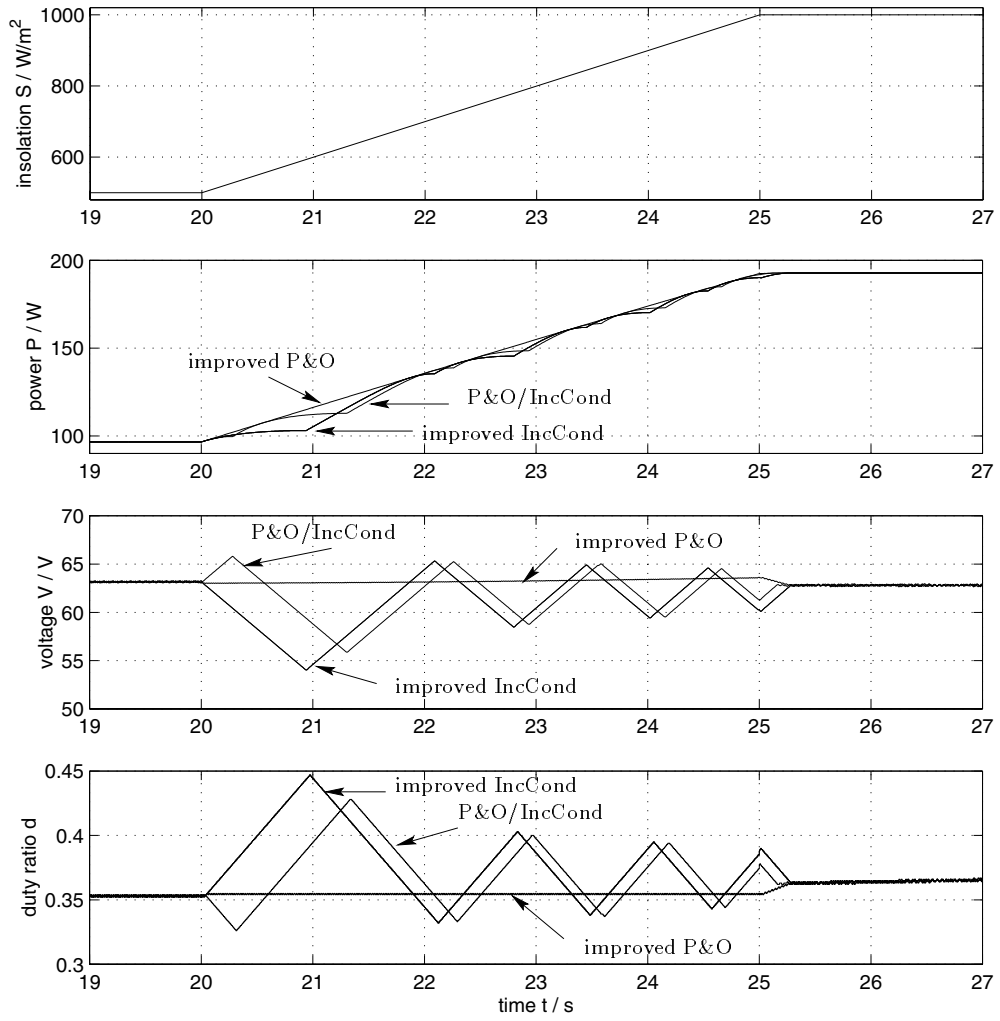


Figure 4.23: Signals of the four simulated MPPTs employing a boost converter during rapidly increasing insolation.

already discussed in this section. All of the plotted signals resemble those obtained with the buck converter system and only differ in their actual scale.

4.2.3 Performance under changing temperature levels

Besides insolation, a second important factor influencing the characteristics of a photovoltaic cell array is the cell temperature T (see Figures 2.7 and 2.9). The thermal mass of the solar panels causes the gradient of this variable to be much smaller than that of the insolation. The temperature primarily depends on the availability of solar radiant energy. In periods of high-level insolation the cell temperature will increase slowly until a thermal balance is reached. During shady or overcast periods the cells will gradually cool off. A sudden increase in temperature will usually never occur, whereas a rapid decrease in temperature may happen as a result of a sudden rainstorm or similar influences.

As can be seen from the solar panel's P - V -characteristics in Figure 2.9 the changes in temperature do not influence the output power as drastically as the changes in insolation, but the location of the MPP and the corresponding value of the panel voltage V_{mp} varies considerably with T .

Comparison of Figures 2.8 and 2.9 reveals that the variations of V_{mp} caused by changes in temperature are much greater than those caused by changes in insolation. Fortunately changes in temperature occur only gradually in most cases and therefore do not present a challenge to the controller which adjusts the panel's output voltage by changing the dc-to-dc converter's duty-ratio d .

The performance of the various MPPT mechanisms under variations in cell temperature will be evaluated in the present section.

Slowly increasing temperature

Consistent solar radiation on the solar panel's surface will result in an increase in cell temperature T and therefore result in a gradual reduction in output power accompanied by a reduced value for the optimum operating voltage V_{mp} . These changes in operating conditions must be detected by the MPPT and the appropriate adjustments made.

Figure 4.24 shows the plots of the output and control signals of the various MPPT techniques during a period of slowly increasing cell temperature. The temperature rises within 15 seconds from 40 °C to 45 °C at an insolation of 1000 W/m².

As can be seen in the presented graph (Figure 4.24), the rising temperature causes a decrease in output power which triggers the necessary changes in d by the MPPT to adjust the system in the direction of V_{mp} . All tested MPPT techniques perform equally well except the improved IncCond algorithm. The addition of the small marginal error ϵ to the conventional IncCond method improves this technique's steady-state ripple behavior, but makes it less sensitive to changes in environmental conditions. This drawback was already detected in the simulations evaluating the performance under changing insolation levels. It now leads to a clearly visible deviation from the optimum operating point and a reduction in the average power output under changing temperature levels. Consideration of the plot of the duty-ratio d in Figure 4.24 shows how the improved IncCond algorithm still keeps skipping perturbation steps even as the power signal significantly drops below the level marked by the other output power curves.

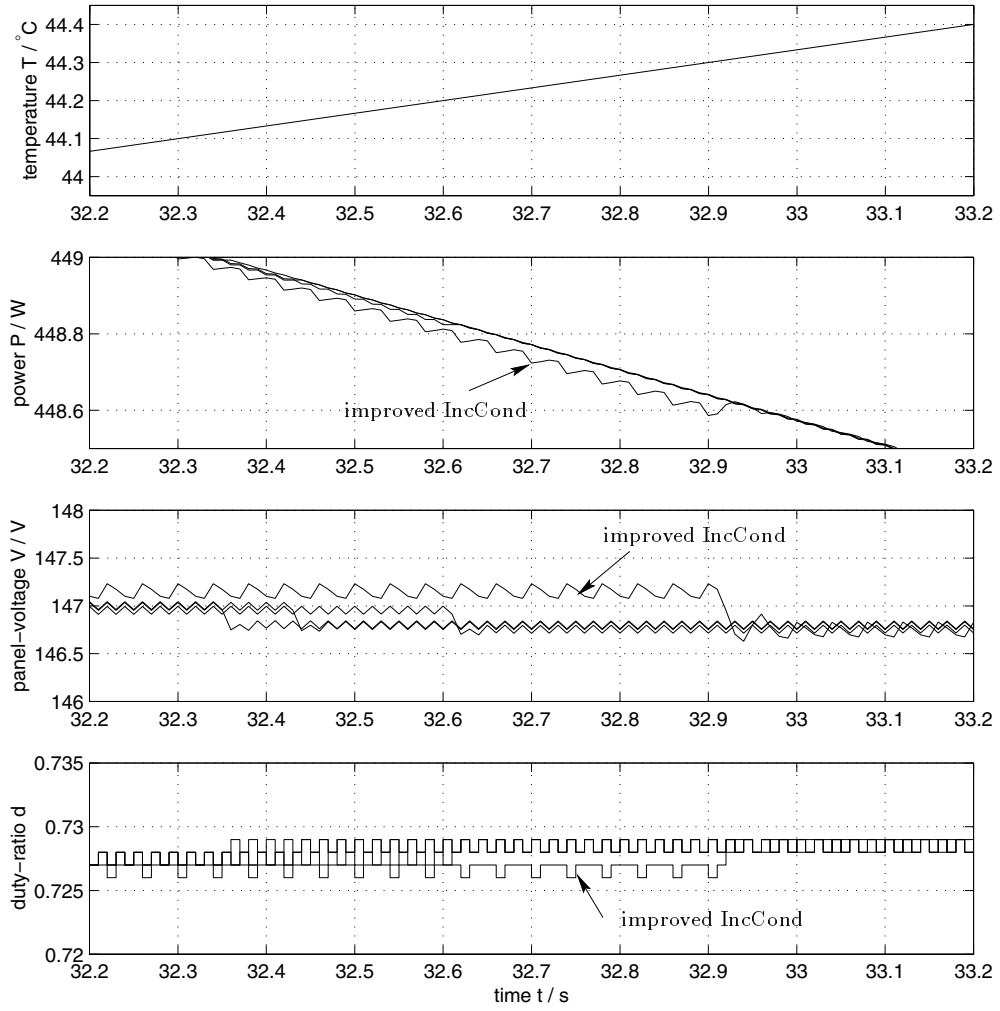


Figure 4.24: Output power, panel voltage, and the duty-ratio d for the various MPPT algorithms under slowly increasing cell temperature.

Slowly decreasing temperature

A decrease in cell temperature will occur as the insolation level drops or when the air surrounding the solar panels cools down. If the insolation is kept constant during the simulation, a lower cell temperature will increase the efficiency and therefore the power output of the photovoltaic cells as can be seen in Figure 2.9.

Figure 4.25 shows how under the circumstances of slowly decreasing cell temperature the panel output power slowly increases. For this simulation the cell temperature was set to a linear decrease from a level of 45 °C to 40 °C within a period of 15 seconds under an insolation of 500 W/m².

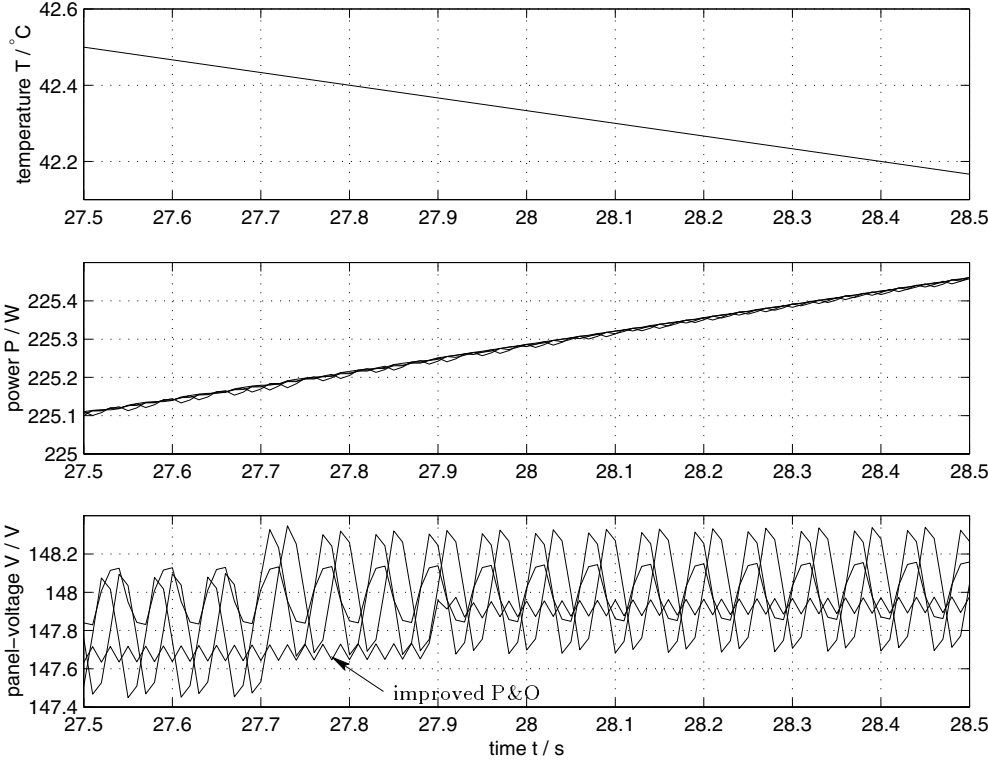


Figure 4.25: Signals for output power and panel voltage of the various digital MPPT methods under slowly decreasing cell temperature.

It can be seen that all MPPT methods track the linear increase in power quite accurately even though the various panel voltages V show significant differences in their ripple behavior. The improved P&O algorithm shows its typical reaction to the increasing power level: as discussed earlier, the panel voltage is kept oscillating around a constant point to cut off deviations from the optimum operating point. This results in a reduced output ripple during the power increase but also, as a result of the *slowly* increasing power levels, in a slightly lower average power output than detected with the other MPPT methods.

Quickly decreasing temperature

A sudden rainstorm or similar occurrences will result in a faster reduction in cell temperature than usually expected. Even though the power output of the solar array will be most likely minimized due to low insolation levels, the reaction of the MPPT to such an occurrence must still be tested and evaluated.

Figure 4.26 shows the signal behavior of the various MPPT mechanisms during a decrease in cell temperature from 50°C to 40°C within 10 seconds. The plot does not reveal any new properties in comparison with the plot obtained under slowly decreasing cell temperature (Figure 4.25). The previously discussed differences between the various MPPT techniques are amplified such that the damping behavior of the improved P&O algorithm becomes clearly visible. The high ripple in the voltage signal of the improved IncCond algorithm is a result of the added error margin ϵ which causes a delayed detection of changes in the environmental conditions. Close inspection of the control signal d for the improved IncCond method reveals that the controller still keeps skipping several perturbation steps, even though the power deviates from the MPP.

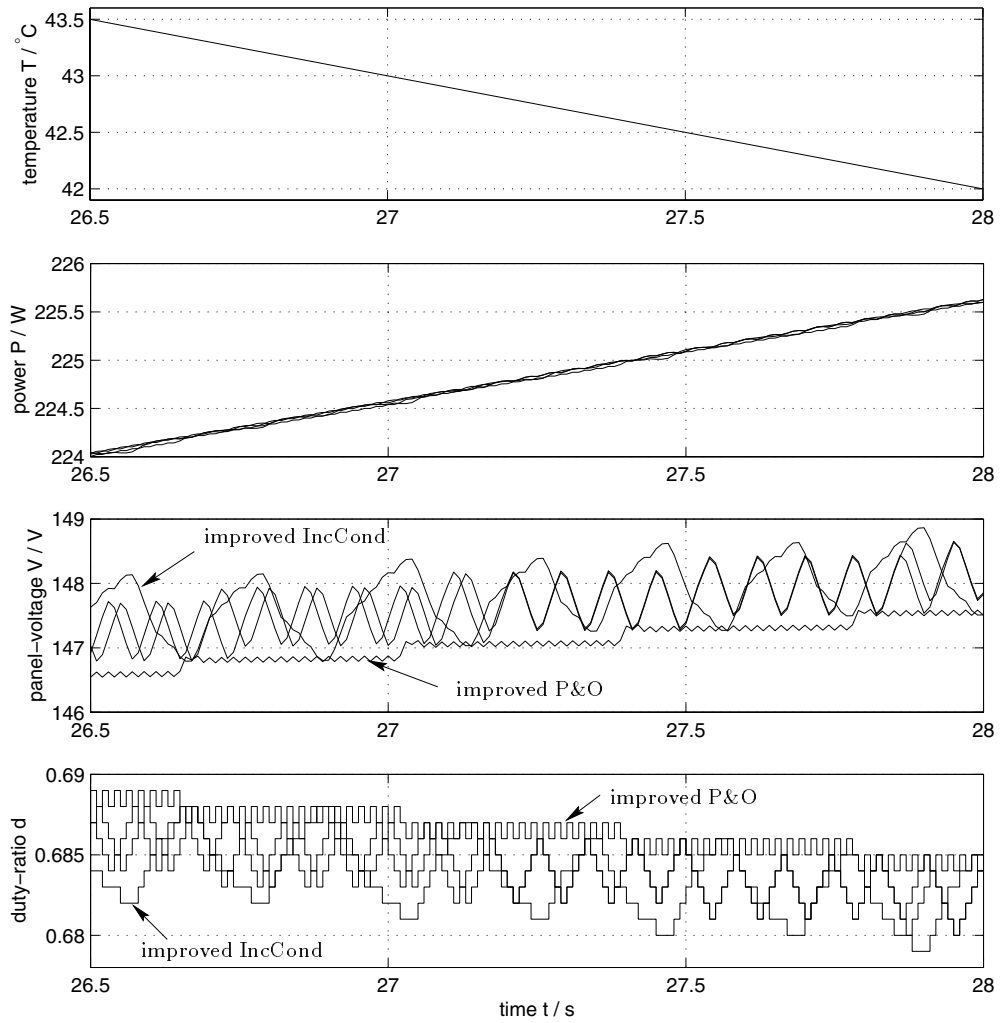


Figure 4.26: Signals of output power, panel voltage, and the duty ratio d of the various MPPT algorithms under quickly decreasing cell temperature.

A comparison of the average power output of the different MPPT techniques under these conditions shows the lowest values for the system controlled by the improved P&O algorithm. Even the high ripple amplitude associated with the improved IncCond algorithm yields better results than the improved P&O method in this case.

The simulations discussed in this section were all performed employing a buck dc-to-dc converter on a five panel solar array. A comparison of the MPPT performance employing other converters such as the boost or the buck-boost did not reveal any new properties in the power supply system's behavior.

4.2.4 Performance under simulated random variations of temperature and insolation

The preceding sections covered the simulation, analysis, and discussion of the performance of the various MPPT techniques under certain isolated environmental conditions. This led to a detailed understanding of the system's response to the individual tracking mechanism and its reaction to such events as quickly increasing insolation or a rise in the cell temperature.

In the real world operation of a solar power supply system, these conditions never occur in isolation. As already mentioned in the previous section, the cell temperature strongly depends on the insolation level, even though the changes in temperature are much smoother and slower than the changes in insolation.

To simulate such a 'real world' operating condition, various filter types were applied to randomly generated Gaussian white noise to produce an insolation and temperature profile as shown in the two bottom curves of Figure 4.27. Both pro-

files cover a time span of 300 seconds which is equal to a simulation of a 5 minute operating period. The insolation profile covers irradiance levels between 300 W/m^2 and 1000 W/m^2 while the temperature varies between 35°C and 48°C . This generated set of values was then used as variable parameters S and T in equations (2.4), (2.5), (2.6), and (2.9).

The conventional P&O MPPT

Figure 4.27 shows the various parameters such as output power, panel voltage, duty-ratio, and the battery voltage of a P&O controlled solar power supply system under randomly varying temperature and insolation levels.

A typical behavior of the conventional P&O method can be noted in the plots of the duty-ratio and the panel voltage: at every instance of increasing power levels the curves reveal large spikes which are an indication of the earlier discussed deviation from the MPP at increasing insolation levels.

The graphs in Figure 4.27 further show that the battery voltage is not at a constant voltage level throughout the whole time of operation as assumed by Sullivan and Powers [SP93]. In fact, it varies closely with the changes in temperature. This can be explained with the help of Figures 2.8 and 2.9: changes in cell temperature cause wide variations of the optimum operating voltage V_{mp} , whereas changes in insolation strongly influence the value of the maximum power output which is closely associated with the optimum operating current I_{mp} . At the same time the battery represents a system with a relatively high time constant τ (see section 4.1.2 and Appendix A). This is the reason why the short time changes (spikes) in the panel voltage are neglected whereas the changes caused by the temperature variations appear.

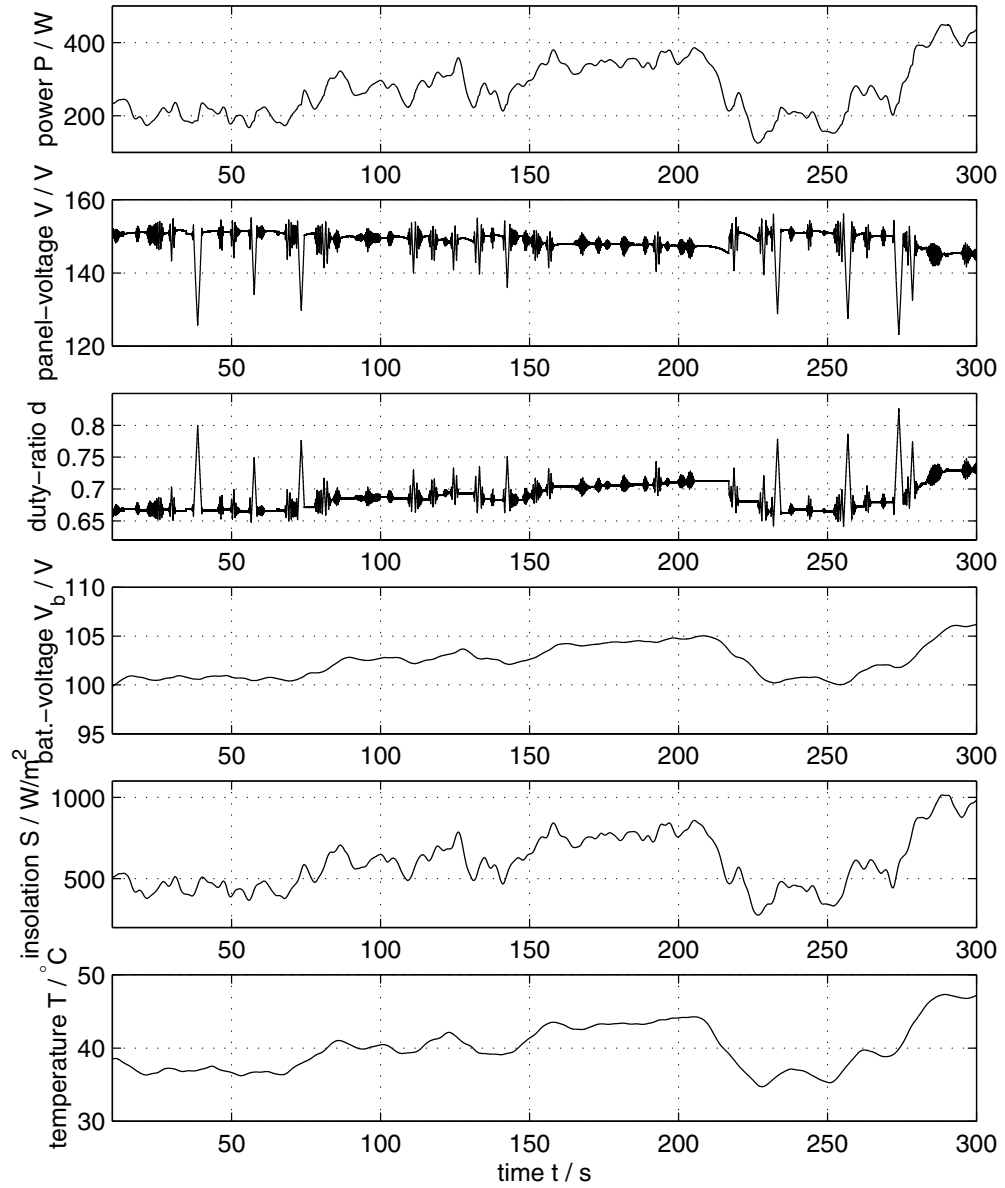


Figure 4.27: Signal curves of a solar power supply system controlled by a conventional P&O MPPT under randomly varying environmental conditions.

The improved P&O MPPT

The mentioned deviation from the MPP under increasing insolation levels in combination with the conventional P&O MPPT algorithm can be overcome by the addition of a “control condition” as discussed in section 3.4.1. This condition is fulfilled if the output power increases with two consecutive perturbation steps of the control variable in the same direction. This triggers the MPPT controller to oscillate its output at the current operating point until the rapid power increase subsides.

Figure 4.28 shows the plots of various signals of the solar power system controlled by this improved P&O MPPT. The significantly reduced spikes in the panel voltage and the duty-ratio signals are an indication that the added control condition prevents the problematic deviation under increasing insolation levels.

The small spikes still visible in the panel voltage signal are a result of the idling status of the improved P&O MPPT during an increase in insolation: the rising output power causes a slow increase in battery voltage which moves the panel voltage to a higher level. Additionally, the higher insolation causes an increase in cell temperature which results in a reduction of the optimum operating voltage V_{mp} as discussed in the previous section. The MPPT can not react to these variations until the increase in insolation is over, resulting in an associated power loss.

The final evaluation of the various MPPT techniques at the end of this chapter will reveal the weight of the advantages and disadvantages of the improved P&O in comparison with the other digital MPPT approaches in general and with the conventional P&O algorithm in particular.

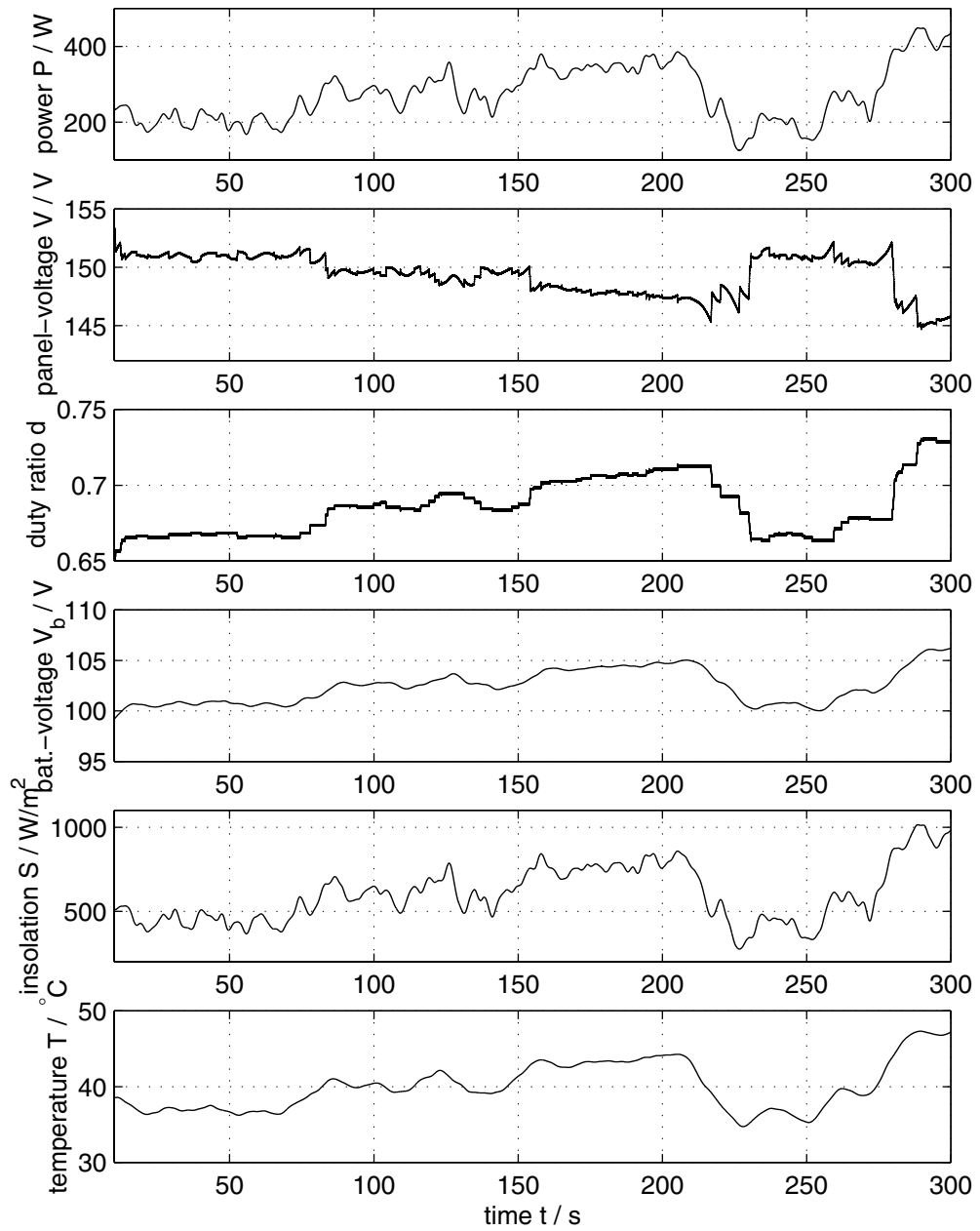


Figure 4.28: Signal curves of a solar power supply system controlled by the improved P&O MPPT under randomly varying environmental conditions.

The IncCond MPPT

Another approach to MPPT was introduced in section 3.4.2 as the IncCond MPPT method. It is based on the evaluation of the value of the derivative $\frac{dP}{dV}$ and therefore is able to determine the relative location of the MPP. This helps to avoid an eventual perturbation step in the opposite direction of the MPP and therefore purports to be a faster and more accurate tracking mechanism than the P&O method.

Figure 4.29 represents the signals of the IncCond MPPT-controlled solar power supply system under randomly varying environmental operating conditions.

A comparison of the graphs with those obtained with the simulation of the simple P&O method does not reveal any differences. The reason for this similarity was already discovered in section 4.2.1: the approximation of the derivative $\frac{dP}{dV} = \frac{V}{I} + \frac{dV}{dI}$ by the incremental changes $dI \approx I(k) - I(k-1)$ and $dV \approx V(k) - V(k-1)$ and the high resolution of their measurement causes the maximum power condition $\frac{dP}{dV} = 0$ to rarely occur. Furthermore an eventual single perturbation step of the simple P&O mechanism in the wrong direction is not so momentous that it would result in a totally different output power curve. As a result the IncCond method is basically limited to its simple tracking mechanism which is not very different from the simple P&O method — thus the similarity in their plots.

The improved IncCond MPPT

As already mentioned earlier, the IncCond method can be improved by adding a small marginal error ϵ to its maximum power condition $\frac{dP}{dV} = 0$. This resulted under stable operating conditions in a significant reduction of the output power ripple and the associated power losses.

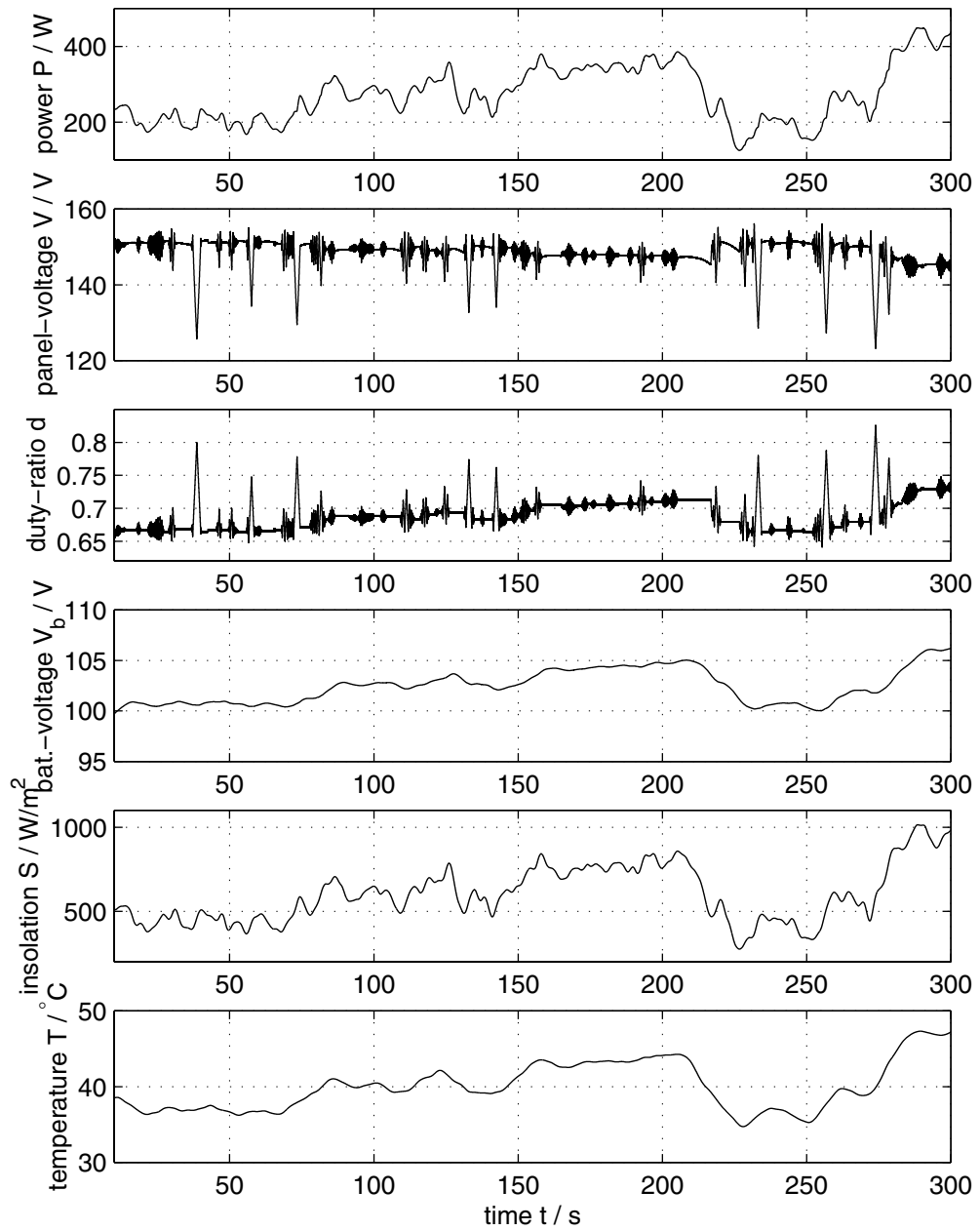


Figure 4.29: Signal curves of a solar power supply system controlled by the IncCond MPPT under randomly varying environmental conditions.

Figure 4.30 shows the plots of the signals of a solar power supply system controlled by this improved IncCond algorithm under randomly varying environmental conditions.

A comparison of the graphs in Figure 4.30 with the plots of the conventional IncCond method in Figure 4.29 reveals increased spikes in the panel voltage and in the duty-ratio d . This is an indicator of a stronger deviation from the MPP under increasing insolation than that detected for the simple IncCond technique. This poor behavior is caused by the addition of the small marginal error to the maximum power condition $\frac{dP}{dV} = 0$ which makes it less sensitive to changes in the environmental operating conditions.

A detailed comparison of the improved IncCond method with the other tested MPPT techniques can be found in the next section where its overall performance will be evaluated.

Comparison of the various MPPT techniques under varying environmental conditions

Figure 4.31 shows a section of the superimposed plots of the power signals of the tested tracking techniques under these simulated ‘real world’ operating conditions.

The plots reveal what would have been expected from the results of the experiments under quickly changing insolation levels: the improved P&O algorithm shows a superior performance in tracking capability as rapid changes occur. Furthermore it can be noted that the conventional P&O and IncCond techniques produce almost identical output power curves, even though they use two different tracking approaches. The idea of using the derivative $\frac{dP}{dV}$ to obtain information about the relative location of the MPP fails due to the use of the small incremental

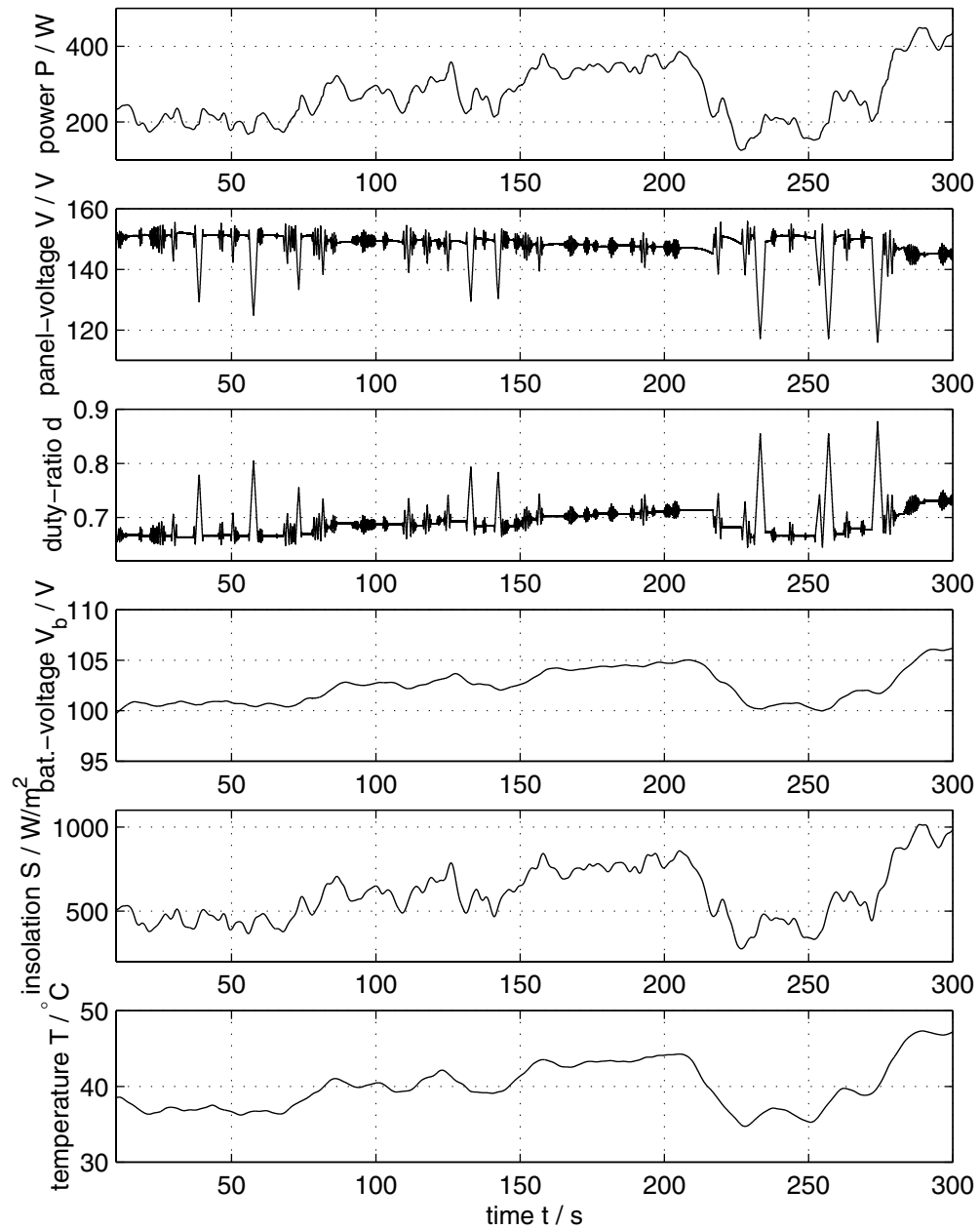


Figure 4.30: Signal curves of a solar power supply system controlled by the improved IncCond MPPT algorithm under randomly varying environmental conditions.

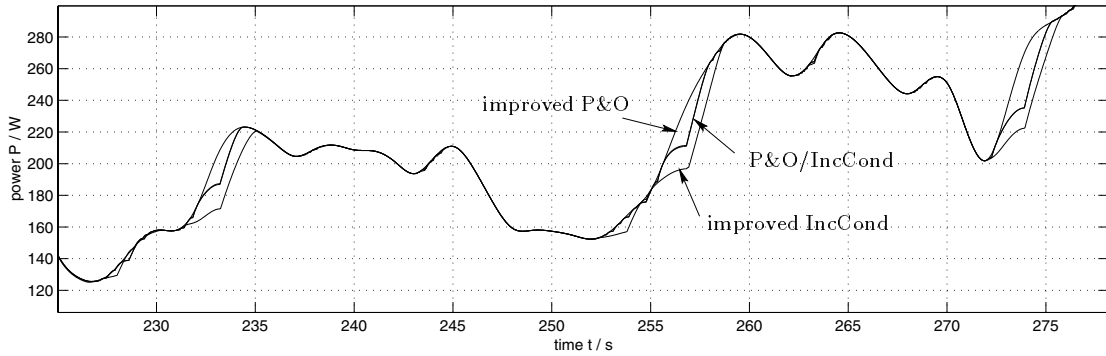


Figure 4.31: Comparison of the power signals of the various MPPT methods under randomly varying temperature and insolation levels.

changes $I(k) - I(k - 1)$ and $V(k) - V(k - 1)$ as an approximation of the necessary values dI and dV . This causes the IncCond algorithm to encounter the same problem as the conventional P&O technique: it *always* interprets an increase in panel power as a result of its own action and therefore leads to a deviation from the MPP during a power increase caused by changes in the operating environment (see also section 3.4.1). The improved IncCond method shows an additional increase in this effect. This higher deviation is clearly visible in Figure 4.31 and is caused by the addition of the small error margin ϵ which was added to allow better ripple suppression under stable environmental operating conditions.

A comparison of the average output powers achieved with the various MPPT techniques showed that the improved P&O method yields an approximately 0.36 % higher power output than the other tested methods under these randomly changing environmental conditions.

The discussed simulations in this section were all performed employing a buck step-down dc-to-dc converter on a photovoltaic cell array with five standard panels connected in series. Other configurations were also tested employing a boost and

buck-boost converter but did not reveal any new properties of the various MPPT approaches.

An example signal plot of a solar power system with randomly changing operating conditions employing a boost converter controlled by the P&O MPPT can be found as Figure B.10 in Appendix B.

Chapter 5

Conclusions

In the previous chapters various approaches to maximum power point tracking were successfully simulated and evaluated using The MathWorks' simulation tool SIMULINK[®]. Valuable information on the performance of the individual MPPT techniques was gathered to allow the specification of a method which will significantly increase the efficiency of the solar racing car SOLTRAIN. A detailed analysis of the individual components of the photovoltaic power system was undertaken to evaluate their performance in the complete system under operating conditions characteristic for a moving vehicle.

The simulations were concentrated on the analysis and evaluation of microprocessor controlled MPPT methods which provide superior controllability and have the ability to handle very complex tracking conditions.

Analog MPPT systems, as introduced in section 3.4.3, were not further investigated since they only permit the realization of very basic MPPT techniques. Any improvement and addition of extra modes and operating conditions would be very difficult to accomplish and even impossible without the support of logic devices.

Systems using power feedback and direct microprocessor control of the dc-to-dc converter's PWM input d , were found to be best suited for a solar car environment.

They are independent of the load configuration and thus will perform reliably in combination with the SOLTRAIN's PWM motor controller.

Very encouraging results were obtained with the improved P&O method proposed by Burger [Bur97]. Operation under slowly increasing power levels, caused by moderately rising insolation levels or by decreasing cell temperature, revealed a slight lag behind the other simulated techniques and an associated power loss. This was more than overcome by this technique's extraordinary performance under rapidly increasing insolation levels. The deviation from the MPP, as observed with other simulated MPPT methods, did not occur. This made the improved P&O algorithm superior to all evaluated models and led to a significantly higher average power output under randomly and rapidly changing environmental conditions as they occur in a moving vehicle.

A comparison of the improved P&O algorithm with the results of the improved IncCond method revealed a slight disadvantage of Burger's technique under stable operating conditions: the continuous oscillations around the MPP, typical to the P&O method, led to a slightly reduced efficiency. Thus Burger's P&O technique might not be the best choice for a stationary solar power supply system, but it yields the best results in the operating environment of a solar vehicle.

The problem of continuous oscillation under stable conditions could most likely be reduced by adding another branch to the flow chart representing the P&O algorithm in Figure 3.3. This branch would represent the condition wherein the array output power $P(k)$ has not changed since the last measurement ($\Delta P(k) = 0$). The process flow would then skip the perturbation of the operating voltage for this cycle so $V_{ref}(k+1) = V_{ref}(k)$.

This would combine the advantages of the improved P&O algorithm under

quickly changing conditions with the superior ripple performance of the IncCond technique under stable conditions. As with the IncCond method it would most likely be necessary to add a small marginal error ϵ to the maximum power condition such that $\Delta P(k) \leq \epsilon$. This would allow smoothing of the output power ripple even though the very slow changes in battery voltage never actually allow for a totally constant operating point.

The influence of the addition of this maximum power condition on the improved P&O method's performance under quickly varying operating conditions would have to be determined in a further course of study. It is expected to enhance this technique's performance under stable conditions but might also slightly slow its ability to react to rapid changes in environmental conditions as was experienced with the improvement of the IncCond method.

Even though the buck converter configuration showed the best behaved system response of all three evaluated types (see Figure 4.9), simulations of the digitally controlled MPPT system showed that all three converters perform adequately.

Since all existing panels of the solar car SOLTRAIN differ in their operating point as well as in their mounted angle on the vehicle, they will all need their separate MPPT system. A combination of panels with different mounting angles would yield a difference in the angle of sunlight incidence and therefore lead to multiple local maxima in the panel's P - V curve [SP93]. A combination of several panels into a larger panel array would therefore require serious consideration and further investigation of the tradeoff between a higher number of MPPT systems versus the possibility of power losses due to operation at a point of reduced efficiency. Table 3.1 shows that the various voltages of the different panels may be well above or below the nominal 108 V operating point of the battery pack, de-

pending on the environmental conditions. This suggests for these particular panels the employment of a buck-boost converter which permits such an operating range.

The implementation of the proposed improved P&O MPPT method in combination with a well designed buck-boost converter would increase the SOLTRAIN's efficiency significantly. As mentioned in section 3.1, the car is currently operating with the simple panel load matching method at an efficiency of approximately 30 % [HS98]. With the proposed MPPT method this efficiency can be raised to above 95 % [SDL91, Raj90]. This more than threefold increase will substantially improve the range and the dynamics of the vehicle.

Bibliography

- [BGK⁺97] A.W. Bett, S.W. Glunz, J. Knobloch, R.Schindler, and W. Wettling. Simplification of process technology for high-efficiency solar cells. In Robert D. McConnell, editor, *Future Generation Photovoltaic Technologies: First NREL Conference*, number 404 in AIP Conference Proceedings, pages 355–365, Denver, CO, March 1997. AIP, American Institute of Physics, Woodbury, New York.
- [Bod77] Hans Bode. *Lead-acid Batteries*. The Electrochemical Society Series. John Wiley & Sons, Inc., New York, 1977.
- [Bur97] Bruno Burger. *Transformatorloses Schaltungskonzept für ein dreiphasiges Inselnetz mit Photovoltaikgenerator und Batteriespeicher*. Ph.D. dissertation, University of Karlsruhe, Karlsruhe, Germany, 1997.
- [Cle96] Barry Dean Clegg. Photovoltaic principles and design of a maximum power point tracker. Master’s thesis, Kansas State University, Manhattan, Kansas, 1996.
- [CR90] Alan Cocconi and Wally E. Rippel. *Lectures from GM sunracer case history*, lecture 3-1: The Sunracer Power System. Number M-101. Society of Automotive Engineers, Inc., 400 Commonwealth Drive, Warrendale, PA 15096-0001, 1990.

- [CS92] Margaret A. Casacca and Ziyad M. Salameh. Determination of lead-acid battery capacity via mathematical modeling techniques. *IEEE Transactions on Energy Conversion*, 7(3):442–446, September 1992.
- [Eri97] Robert W. Erickson. *Fundamentals of Power Electronics*. Chapman & Hall, 115 Fifth Avenue, New York, NY 10003, 1997.
- [EWSS97] Johan H. R. Enslin, Mario S. Wolf, Daniël B. Snyman, and Werner Swiegers. Integrated photovoltaic maximum power point tracking converter. *IEEE transactions on industrial electronics: a publication of the IEEE Industrial Electronics Society*, 44(6):769–773, December 1997.
- [FB83] Alan L. Fahrenbruch and Richard H. Bube. *Fundamentals of Solar Cells: Photovoltaic Solar Energy Conversion*. Academic Press, Inc, New York, NY, 1983.
- [Fey97] Turgut Feyiz. Maximum power condition for photovoltaic cells. Master’s thesis, Kansas State University, Manhattan, Kansas, 1997.
- [GPR90] Lee Goldhammer, Joe Powe, and Gene Ralph. *Lectures from GM sunracer case history*, lecture 3-3: GM Sunracer Solar Panel. Number M-101. Society of Automotive Engineers, Inc., 400 Commonwealth Drive, Warrendale, PA 15096-0001, 1990.
- [GRIR97] R. Gottschalg, M. Rommel, D. G. Infield, and H. Ryssel. Comparison of different methods for the parameter determination of the solar cell’s double exponential equation. In *14th European Photo-voltaic Science and Engineering Conference (PVSEC)*, Barcelona, Spain, 1997.

- [HLS98] Chihchiang Hua, Jongrong Lin, and Chihming Shen. Implementation of a DSP-controlled photovoltaic system with peak power tracking. *IEEE transactions on industrial electronics: a publication of the IEEE Industrial Electronics Society*, 45(1):99–107, February 1998.
- [HMHO95] K.H. Hussein, I. Muta, T. Hoshino, and M. Osakada. Maximum photovoltaic power tracking: an algorithm for rapidly changing atmospheric conditions. In *IEE Proceedings. Generation, Transmission and Distribution*, volume 142(1), pages 59–64. IEE, Stevenage, Herts., U.K., January 1995.
- [HS98] Chihchiang Hua and Chihming Shen. Comparative study of peak power tracking techniques for solar storage system. In *IEEE Applied Power Electronics Conference and Exposition*, volume 2 of *APEC Proceedings of the 1998 13th Annual Applied Power Electronics Conference and Exposition, APEC'98*, pages 679–685, Anaheim, CA, USA, February 1998. IEEE, IEEE, Piscataway, NJ, USA.
- [IEC95] Crystalline silicon photovoltaic (PV) array - On-site measurement of I-V characteristics. IEC Standard 61829 (1995-03), International Electrotechnical Commission (IEC), 1211 Geneva 20, Switzerland, 1995.
- [KE96] David L. King and Peter E. Eckert. Characterizing (rating) the performance of large photovoltaic arrays for all operating conditions. In *Proceedings of the 25th IEEE Photovoltaic Specialists Conference*, Conference Record of the IEEE Photovoltaic Specialists Conference, pages 1385–1388, Washington, DC, USA, May 13–17 1996. IEEE, IEEE, Piscataway, NJ, USA.

- [KOS80] Aaron Kirpich, G. O'Brien, and N. Shepard. *Solar Energy Technology Handbook, Part B, Applications, System Design, and Economics*, volume 6 of *Energy, Power, and Environment, A Series of reference Books and Textbooks*, chapter 37, electric power generation: photovoltaics, pages 313–351. Marcell Dekker, Inc., New York, NY, 1980.
- [LLW95] C.-F. Lu, C.-C. Liu, and C.-J. Wu. Dynamic modelling of battery energy storage system and application to power system stability. In *IEE Proceedings Generation, Transmission and Distribution*, volume 142(4), pages 429–435. IEE, Stevenage, Herts., U.K., July 1995.
- [Möl93] H.J. Möller. *Semiconductors for Solar Cells*. Artech House, Inc, Norwood, MA, 1993.
- [Nev78] Richard C. Neville. *Solar Energy Conversion: The Solar Cell*, volume 1 of *Studies in Electrical and Electronic Engineering*. Elsevier Scientific Publishing Company, New York, N.Y., 1978.
- [Raj90] Anita Rajan. A maximum power point tracker optimized for solar powered cars. In *Future Transportation Technology Conference and Exposition, San Diego, California, August 13–16, 1990*, number 901529 in SAE Technical Paper Series. SAE, Warrendale, PA, USA, 1990.
- [SCL92] Ziyad M. Salameh, Margaret A. Casacca, and William A. Lynch. A mathematical model for lead-acid batteries. *IEEE Transactions on Energy Conversion*, 7(1):93–98, March 1992.
- [SDL91] Ziyad M. Salameh, Fouad Dagher, and William A. Lynch. Step-down

- maximum power point tracker for photovoltaic systems. *Solar Energy*, 46(5):279–282, 1991.
- [SH84] John F. Schaefer and L. Hise. *An inexpensive photovoltaic array maximum-power-point tracking dc-to-dc converter*. Number NMSEI/TN-84-1. New Mexico Solar Energy Institute, Las Cruces, New Mexico 88003, May 1984.
- [SMD88] Ziyad M. Salameh, A. K. Mulpur, and F Dagher. Two stage electrical array reconfiguration controller for PV powered water pump. In *Proceedings of the 1988 Annual Meeting, American Solar Energy Society*, pages 399–404, June 1988.
- [SP93] Charles R. Sullivan and Matthew J. Powers. High-efficiency maximum power point tracker for photovoltaic arrays in a solar-powered race vehicle. In *Proceedings of the 1993 IEEE 24th Annual Power Electronics Specialists Conference, PESC Record - IEEE Annual Power Electronics Specialists Conference*, pages 574–580, Seattle, WA, USA, June 1993. IEEE, IEEE Piscataway, NJ, USA.
- [ST90] Ziyad M. Salameh and Daniel Taylor. Step-up maximum power point tracker for photovoltaic arrays. *Solar Energy*, 44(1):57–61, 1990.
- [Stö94] Prof. Dr. Horst Stöcker, editor. *Taschenbuch der Physik*. Verlag Harry Deutsch, Frankfurt am Main, Germany, second edition, 1994.
- [TMW98] The Mathworks, Inc., Natick, MA 01760-1500. SIMULINK[®]: *Dynamic System Simulation for MATLAB[®]*, version 2.2 edition, January 1998.

- [YD92] H. Yongji and L. Deheng. A new method for optimal output of a solar cell array. In *IEEE International Symposium on Industrial Electronics*, volume 1, pages 456–459. IEEE, 1992.

Appendix A

A.1 Component specifications for Simulink simulations

```
%%%%%%%%%%%%%%%%%%%%%%%%%%%%%%%%%%%%%%%%%%%%%%%%%%%%%%%%%%%%%%%%%%%%%%%%
%%% LCR.m
%%%
%%% DEFINITION OF VALUES USED FOR ALL MPPT SYSTEM SIMULATIONS
%%%
%%% HK98/99
%%%%%%%%%%%%%%%%%%%%%%%%%%%%%%%%%%%%%%%%%%%%%%%%%%%%%%%%%%%%%%%%%%%%%%%%

%%%%%%%%%%%%%%%%%%%%%%%%%%%%%%%%%%%%%%%%%%%%%%%%%%%%%%%%%%%%%%%%%%%%%%%% VALUES FOR CONVERTER COMPONENTS %%%%%%%%%
L = 10*350e-6; % = 3.5mH (Burger uses 10mH)
C1 = 10*560e-6; % = 5.6mF (Burger uses 1mF)
C2 = C1;
% R = 0.05; % parasitic resistance of inductor
%%%%%%%%%%%%%%%%%%%%%%%%%%%%%%%%%%%%%%%%%%%%%%%%%%%%%%%%%%%%%%%%%%%%%%%% END CONVERTER COMPONENTS %%%%%%%%%

%%%%%%%%%%%%%%%%%%%%%%%%%%%%%%%%%%%%%%%%%%%%%%%%%%%%%%%%%%%%%%%%%%%%%%%% SOLAR PANEL %%%%%%%%%
G = 0.1; % conductance for linearized model
%%%%%%%%%%%%%%%%%%%%%%%%%%%%%%%%%%%%%%%%%%%%%%%%%%%%%%%%%%%%%%%%%%%%%%%% END SOLAR PANEL %%%%%%%%%

%%%%%%%%%%%%%%%%%%%%%%%%%%%%%%%%%%%%%%%%%%%%%%%%%%%%%%%%%%%%%%%%%%%%%%%% BATTERY VALUES DEFINITION %%%%%%%%%
%
% (according to graphs in Salameh, Casacca, Lynch)
%
% adjusted the values, so there is an overvoltage of 9*3Volts
```

```

% (9 blocks, a 3 Volts) with a charging current of 9.5A
% (max. current for car soltrain).
% (ca 3 Volts overvoltage at Salameh's 12Volt blocks).
% Got the values for Rbs from Lu,Liu,Wu.
%
% Now there is a total rise in Voltage for a 12 hour charging
% period (3.25A) of about 30 Volts (fits to an operating range
% between 95 and 125 Volts).
%
% Since the value for Cbp is fixed by battery capacity and the
% value of Rbp influences the voltage slope during charging
% condition only very little, I have to assume that charging time
% using 9.5A is about 14500 sec. (ca 4h).
%
Rbp = 10e3; % this is Lu's value
Cbp = 2/(125^2-90^2)*45*9*12*3600;
% = 4.6501 kF - calculated after Lu's formula
Rbs = .0013; % same as Lu's value
Rb1 = 2.84; % = 9*3V/9.5A
Cb1 = 2.5; % gives a time constant tau for the overvoltage of
% about 10 sec.
% (Salameh talks about minutes !!!, Lu has 0.001 sec.)
%
%
%%%%%%%%%%%%%%%%%%%%%%%%%%%%%%%%%%%%%%%%%%%%%%%%%%%%%%%%%%%%%%%%%%%%%%%%% END BATTERY VALUES DEFINITION %%%%%%%%%%%%%%%

% peak-peak voltage of triangle at pulse-width modulator
VM = 3;%V

%%%%%%%%%%%%%%%%%%%%%%%%%%%%%%%%%%%%%%%%%%%%%%%%%%%%%%%%%%%%%%%%%%%%%%%%% END OF FILE %%%%%%%%%%%%%%%

```

The solar panel

$$I = I_{ph} - I_{s1} \left[e^{\frac{q(V+IzR_s)}{zn_1kT}} - 1 \right] - I_{s2} \left[e^{\frac{q(V+IzR_s)}{zn_2kT}} - 1 \right] - \frac{V + IzR_s}{zR_p}.$$

The following values were used in the above equation and in expressions (2.4), (2.5), and (2.6):

- $I_{ph}|_{T=298\text{K}} = 3.25\text{ A}$ [Bur97]
- $R_p = 30\ \Omega$ [Bur97]
- $R_s = 15 \cdot 10^{-3}\ \Omega$ [Bur97]
- $E_g = 1.1\text{ eV}$ (for crystalline silicon) [Stö94]
- $n_1 = 1, \quad n_2 = 2$ [GRIR97]
- $k = 1.380 \cdot 10^{-23}\text{ J/K}$ (Boltzmann constant) [Stö94]
- $q = 1.602 \cdot 10^{-19}\text{ C}$ (elementary charge constant) [Stö94]

A.2 Block diagrams of the simulated models

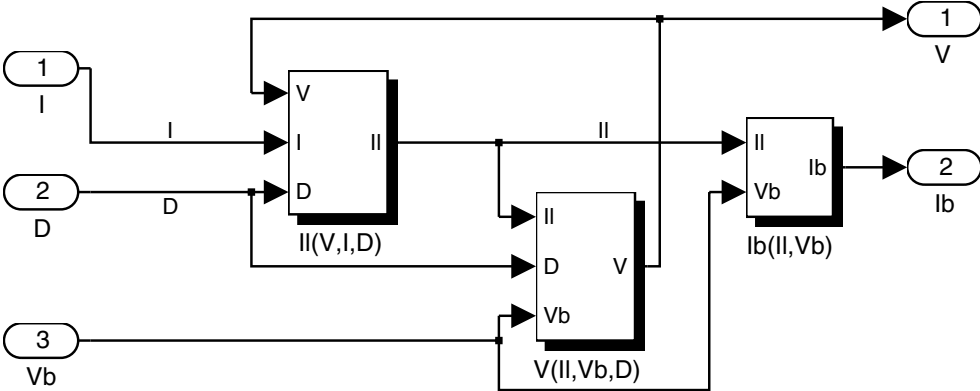


Figure A.1: Block diagram of the buck converter.

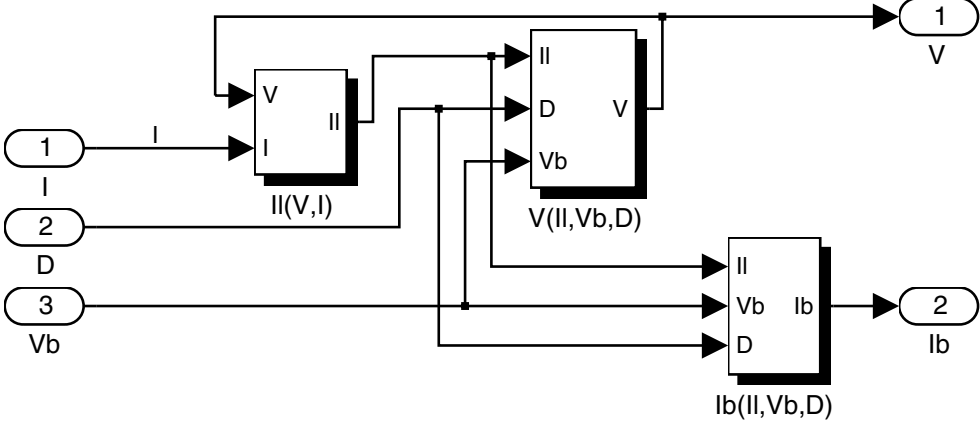


Figure A.2: Block diagram of the boost converter.

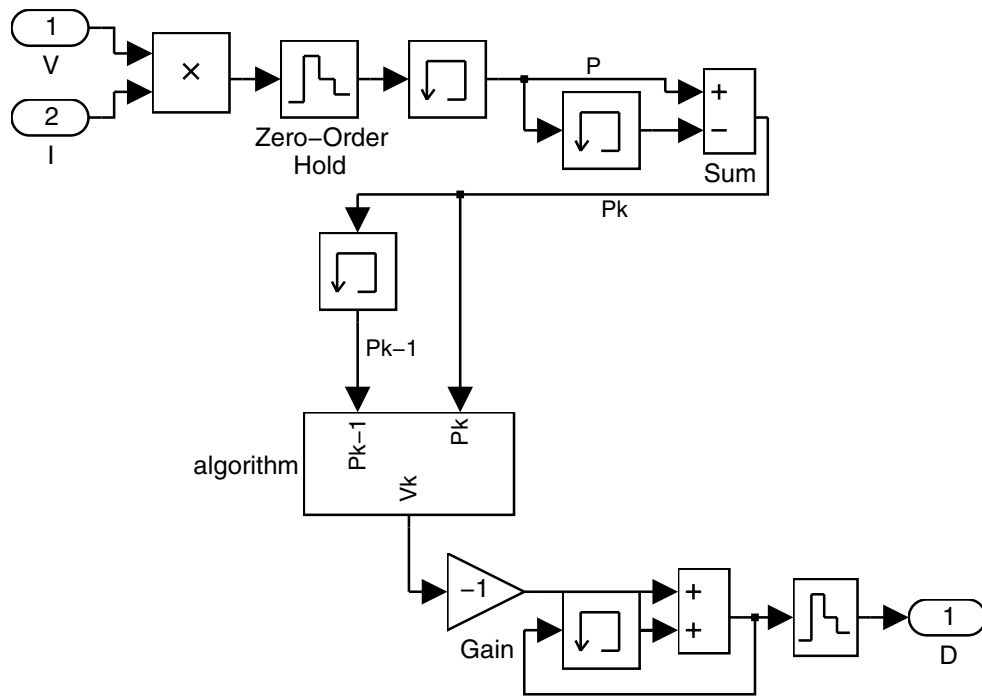


Figure A.5: Block diagram of the improved P&O algorithm.

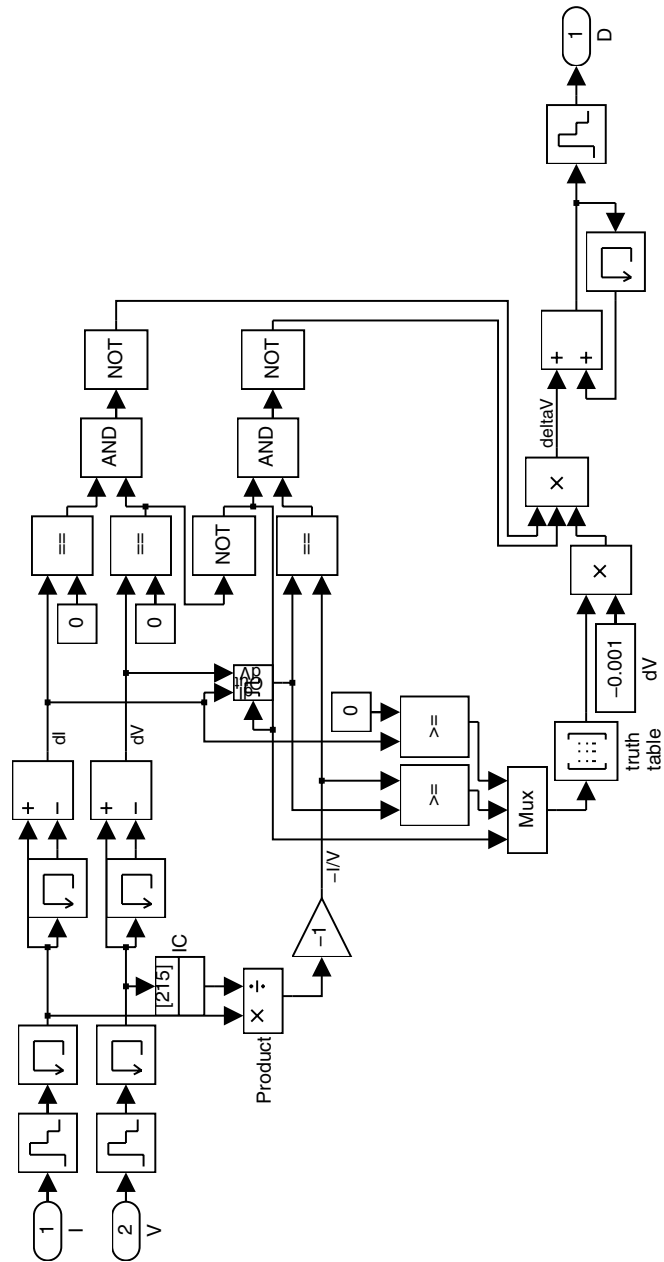


Figure A.6: Block diagram of the IncCond algorithm.

Appendix B

B.1 Signal curves of various system configurations under standard test conditions (STC)

Simulation of the improved P&O MPPT

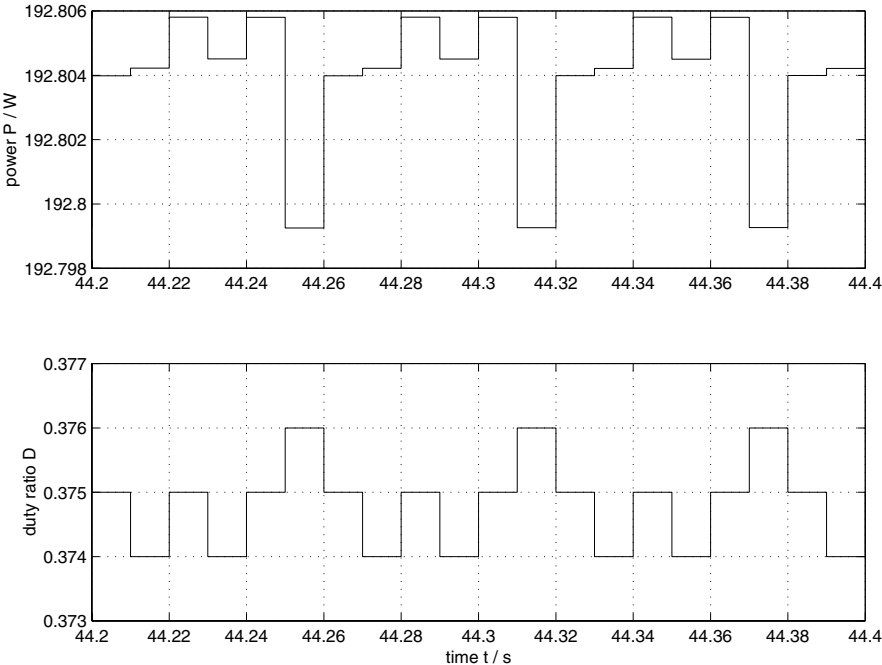


Figure B.1: Power and control signal for the improved P&O method operating with a boost converter at a sampling frequency of 100 Hz.

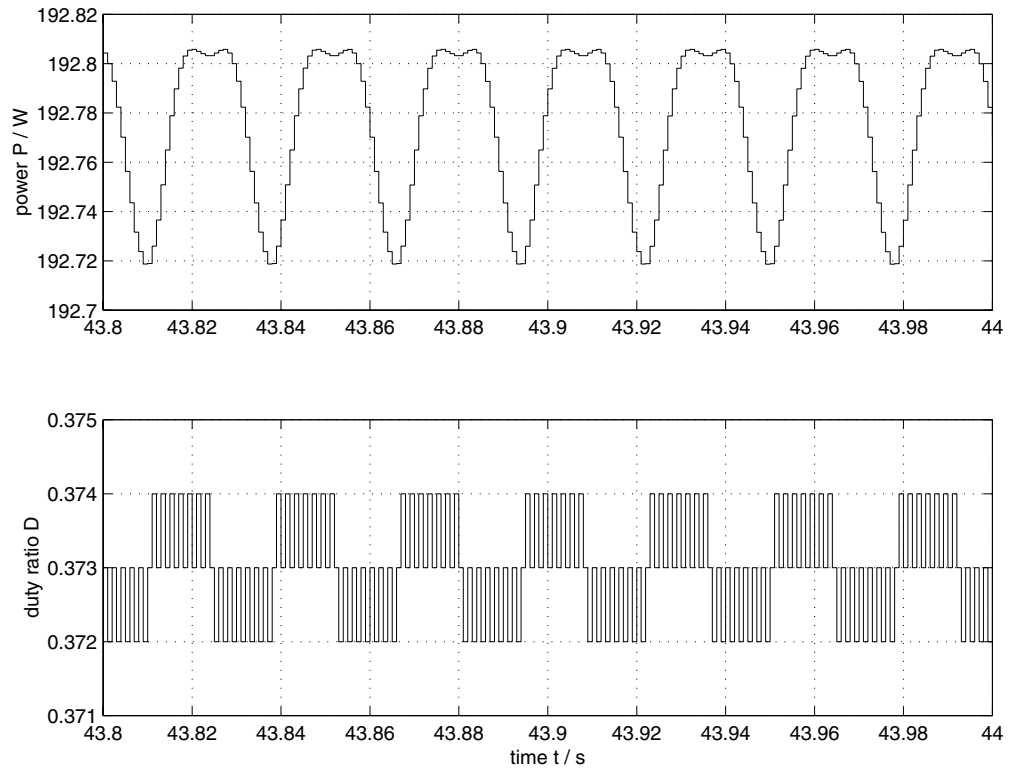


Figure B.2: Power and control signal for the improved P&O method operating with a boost converter at an increased sampling frequency of 1 kHz.

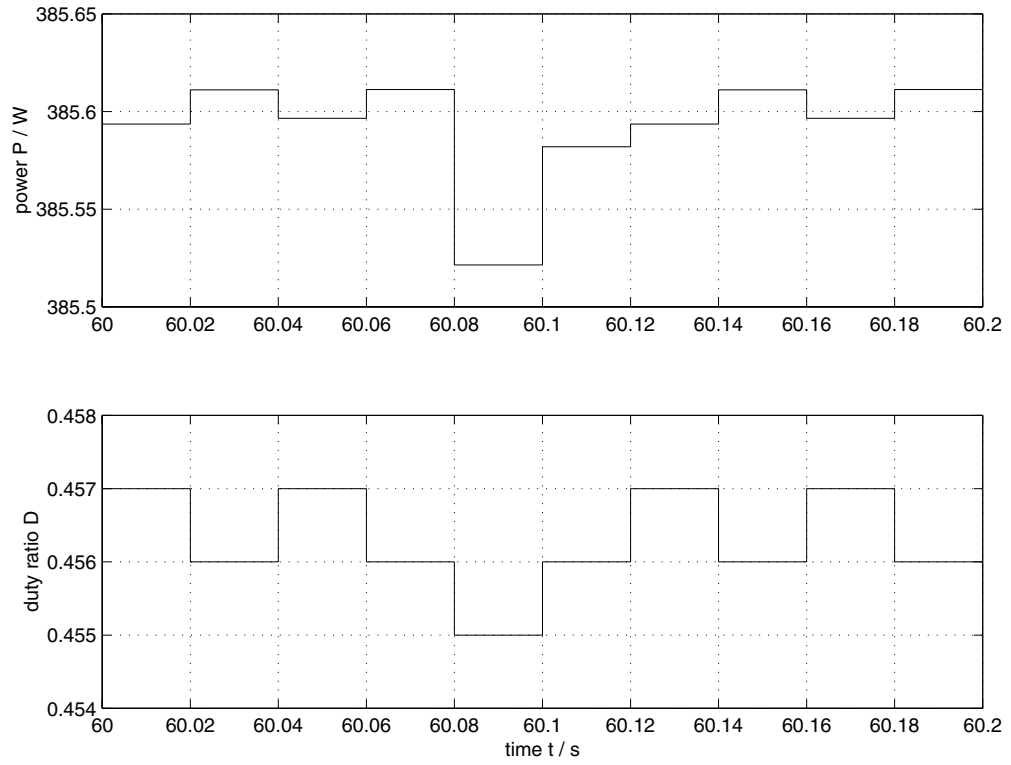


Figure B.3: Power and control signal for the improved P&O method operating with a buck-boost converter at a sampling frequency of 50 Hz.

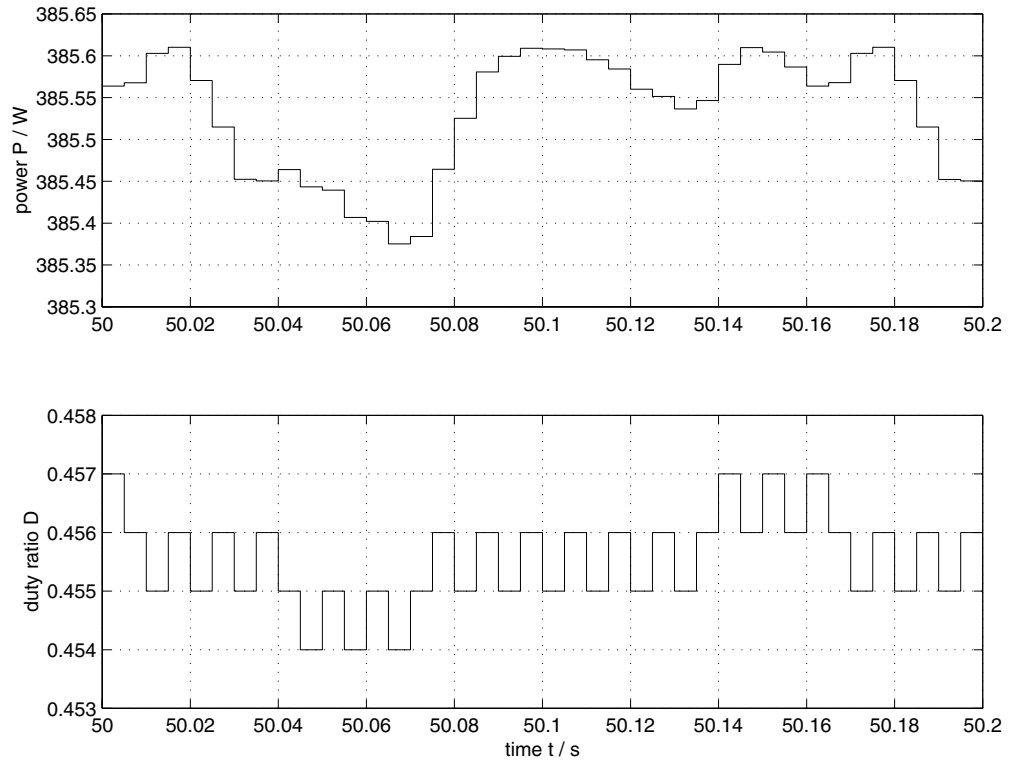


Figure B.4: Power and control signal for the improved P&O method operating with a buck-boost converter at an increased sampling frequency of 200 kHz.

Simulation of the IncCond MPPT

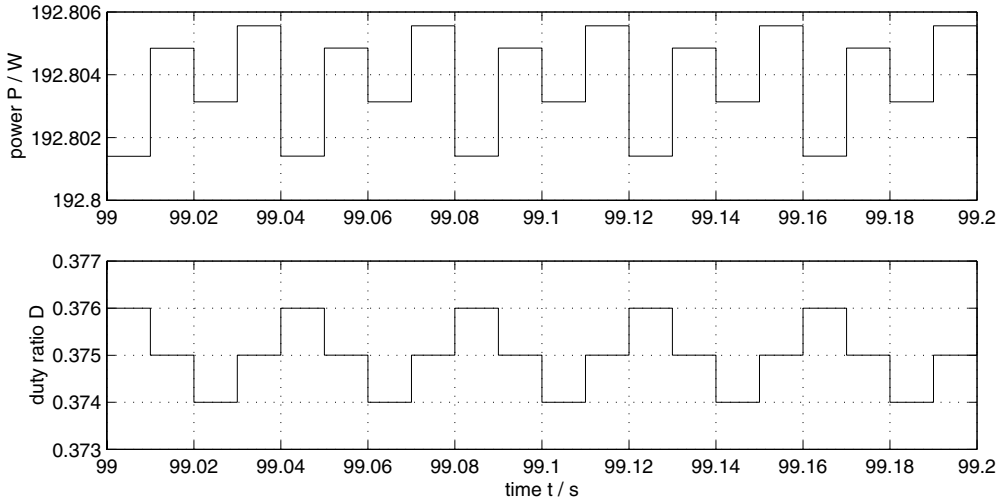


Figure B.5: Power and control signal for the IncCond MPPT operating with a boost converter at a sampling frequency of 100 Hz.

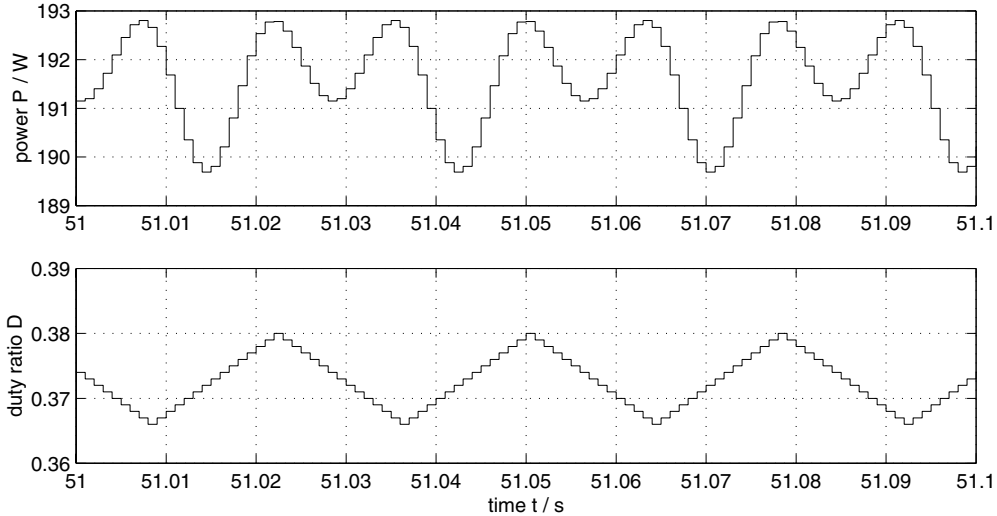


Figure B.6: Power and control signal for the IncCond MPPT operating with a boost converter at an increased sampling frequency of 1 kHz.

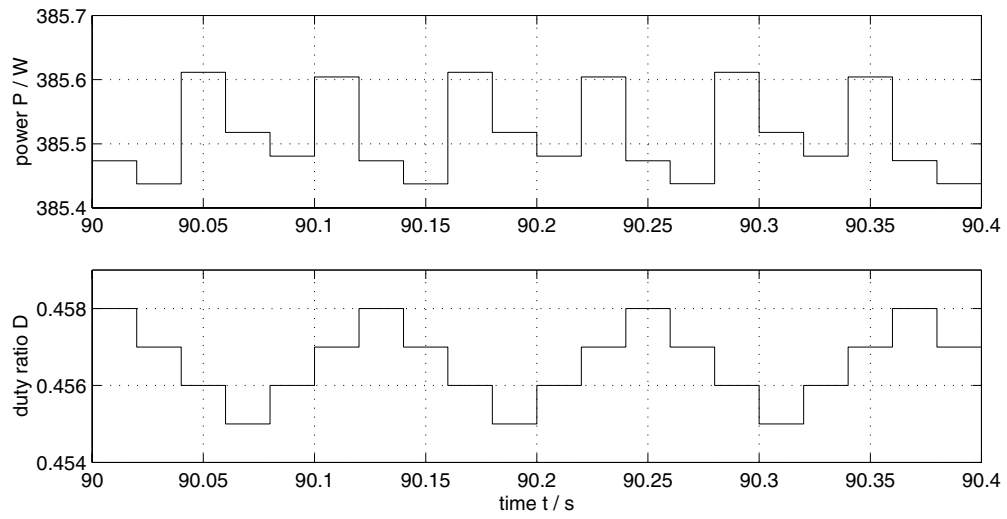


Figure B.7: Power and control signal for the IncCond MPPT operating with a buck-boost converter at a sampling frequency of 50 Hz.

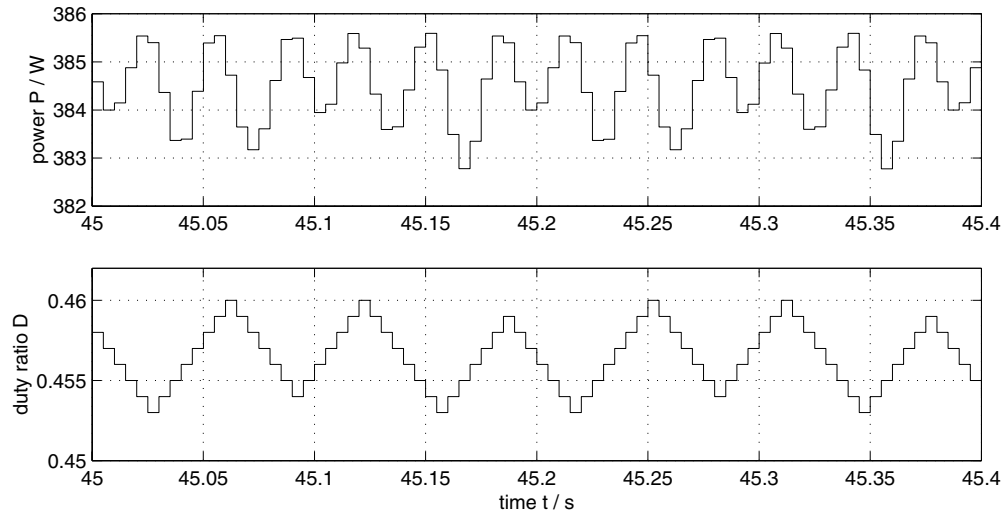


Figure B.8: Power and control signal for the IncCond MPPT operating with a buck-boost converter at an increased sampling frequency of 200 Hz.

B.2 Signal curves under varying operating conditions

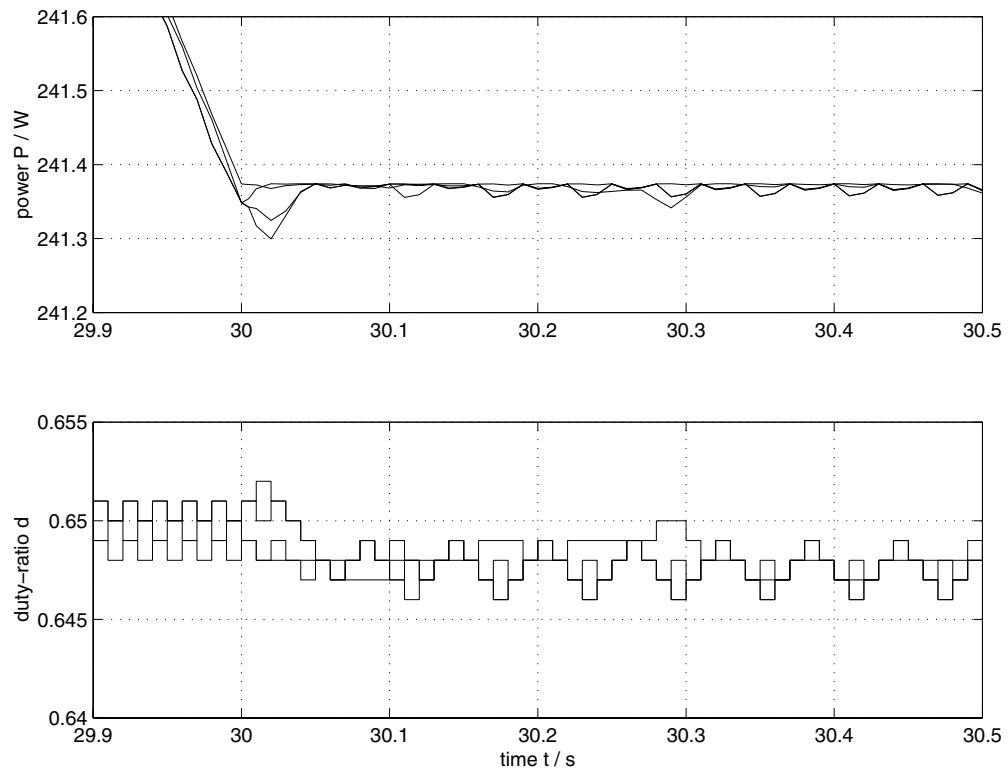


Figure B.9: Output power and control variable d of the various simulated MPPT techniques under slowly falling insolation levels.

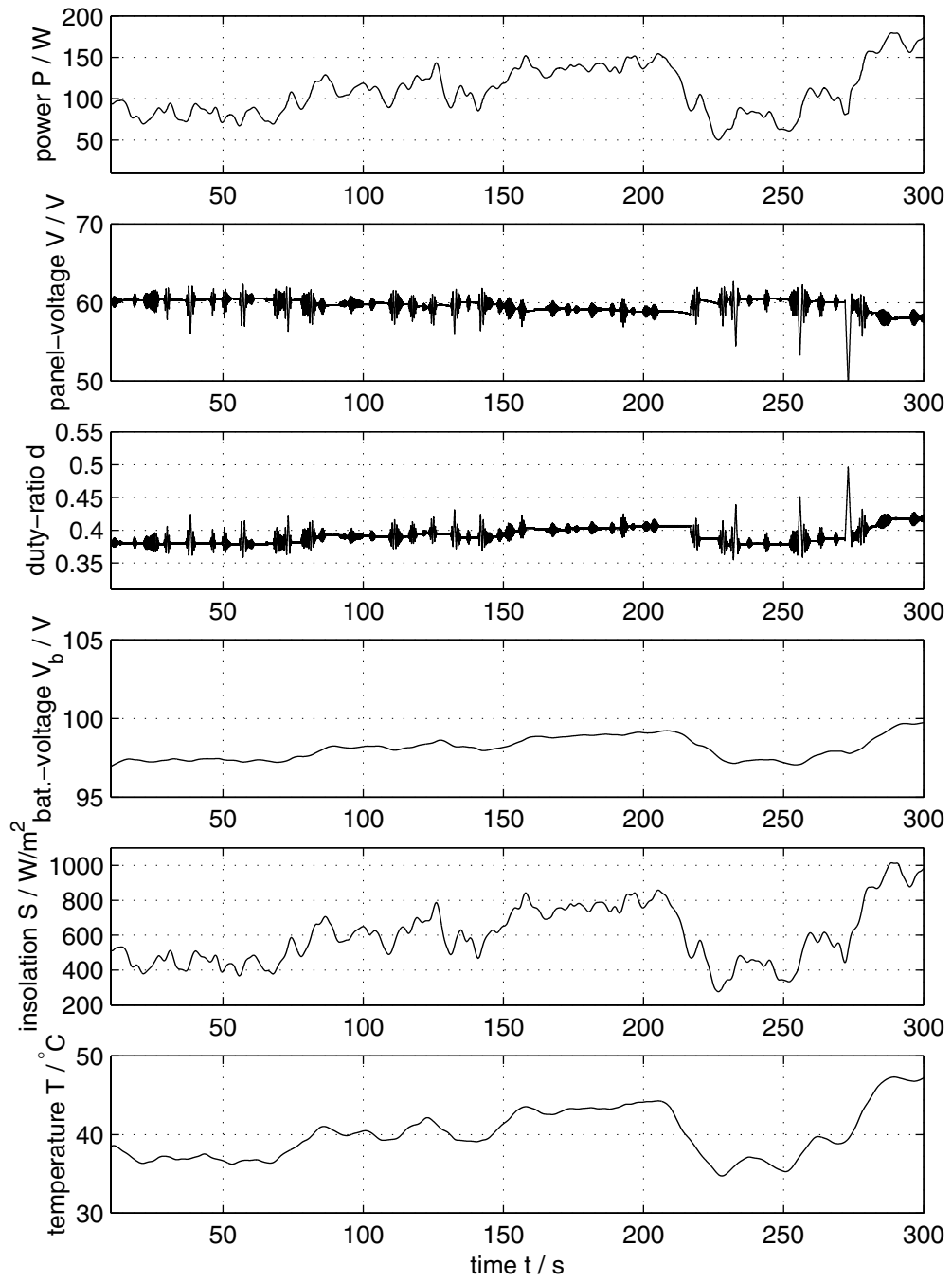


Figure B.10: Signal curves of a solar power supply system employing a boost converter controlled by the P&O MPPT algorithm under randomly varying environmental conditions.